SCHOOL OF SCIENCE
Department of Industrial Chemistry “Toso Montanari”

Second cycle degree in

Low Carbon Technologies and Sustainable Chemistry

Classe LM-71 - Scienze e Tecnologie della Chimica Industriale

Selective hydrogenation of CO_2 to ethanol and higher alcohols using Li-supported Rh nanoparticles

Experimental degree thesis

CANDIDATE
Michela Di Costanzo

SUPERVISOR
Chiar.mo Prof. Nikolaos Dimitratos

CO-SUPERVISOR
Dr. Atul Bansode
Dr. Stefano Scurti
Dr. Michele Offidani

Academic Year 2022-2023

Abstract

One of the greatest and most complicated challenges of the 21*st* century for preventing even more disastrous effects on the habitability of our planet, is to minimize the increasing CO_2 emissions representing the main cause of climate change. This challenge has raised a global interest towards process optimization, renewables, as well as CO_2 capture for storage or for using it as valuable resource to convert it to valuable chemicals and fuels. Therefore, the focus of this thesis is the CO_2 hydrogenation to higher alcohols. Particular attention is given to finding new catalysts and alternative catalyst synthesis methods that allow a good control over the structure of the catalyst involved in the CO_2 hydrogenation reaction. Following both literature studies and previous results obtained by the research group, rhodium (Rh) nanoparticles (NPs) supported on mesosilica has been chosen as metal catalyst. It was prepared with the sol immobilization method, which, compared to conventional techniques, such as wet impregnation and deposition–precipitation, allows a good control of metal particle size before embedding them in the support, thus reducing the influence of the support on metal dispersion. The mesoporous support guaranteed both thermal and mechanical stability to the catalyst, as well as a great dispersion of Rh NPs due to its high surface area. The tests were performed by varying the reaction conditions, the metal loading and by adding Li and Fe as promoters to verify any difference in the catalytic activity for the CO_2 hydrogenation reaction. Due the high redox potential of Fe, the supported RhFeLi alloy NPs was not prepared with the same procedure used for the unpromoted catalyst. An innovative hybrid method was developed, combining sol immobilization with impregnation. The best catalytic results showed 14.3% CO_2 conversion for 1wt%Rh/meso-SiO_2@Li10% and 5.8% of methanol selectivity for 1wt%RhFe/meso-SiO_2@Li10% (both at 250°C, 80 bar, 20 mL/min of CO_2/H_2 with 1/3 ratio). As shown from the BET model, the low activity might be due either to a partial clogging of pores or the collapse of pore structure (or both). Despite the low selectivity towards ethanol production, XPS spectra confirmed the presence of the desired species, and TEM and BET analysis a mesoporous structure with uniform dispersion of Rh NPs throughout all the surface. The efficacy of the synthesis strategy adopted was thus validated.

1 Introduction

1.1 Catalysis: definitions and general concepts

Catalysis plays a vital role in many industries, such as energy and fuels, fine chemicals, pharmaceuticals, and commodity chemicals. Currently, about 90% of chemical manufacturing processes and more than 20% of all industrial products involve catalytic steps [1].

The term "catalyst", derive from the Greek words κατα (kata) = down and λυδειν (lysein) = to split or break, was coined by Berzelius in 1835, who defined it as a substance which by its mere presence evokes chemical actions which would not take place in its absence[1]. It took about sixty years until a new definition of catalysis was given in 1894 by W. Ostwald. Based on the knowledge of chemical equilibrium, Ostwald defined a catalyst as a substance that increases the rate of a chemical reaction, without being consumed or produced. The catalyst changes only the rate of the reaction, and does not change the thermodynamics[2].

The activation energy E_a is that energy barrier the reactant molecules must possess to enable the reaction to take place and that this barrier can only be surmounted by a small fraction of reactant molecules for which the total collision energy exceeds the activation energy. As shown in the diagram in Figure 1, where the potential energy is plotted against the reaction coordinate, a catalyst is as any substance added to a chemical reaction that lowers its activation energy barrier by:

- Orienting the reacting particles in such a way that a greater faction of the particles to have enough energy to react,
- Reacting with the reactants to form an intermediate that requires lower activation energy to form the product, in this way providing an alternative pathway.

In this way, the catalyst increases the reaction rate and allows the reaction to proceed under milder conditions (*e.g.*, low temperature or pressure) towards equilibrium. Nevertheless, it is obvious that a catalyst which increases the reaction rate of the

forward reaction of a reversible reaction must also increase the rate of the reverse process by the same amount.

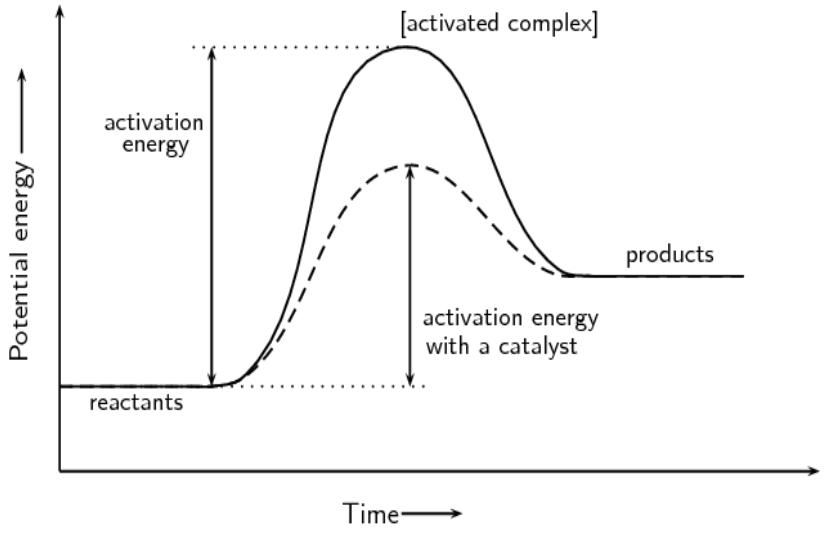

Figure 1. Potential energy profile for a catalysed and uncatalyzed exothermic reaction[1].

1.2 Catalytic systems

Mainly, it is possible to distinguish between three types of catalysts: homogeneous catalysts, heterogeneous catalysts, and biocatalysts.

1.2.1 – Biocatalysis

Biocatalysts are defined as natural substances, like enzymes or cells, used to catalyse chemical reactions[3]. Enzymes have pivotal role in the catalysis of hundreds of biological processes that occur within all living organisms (such as digestion of food or the build-up of proteins and DNA). Without enzymes, many of these reactions would not take place at a perceptible rate[2]. The reactant in an enzyme-catalysed reaction is called a substrate. Enzymes also have valuable industrial (such as fermenting of wine, leavening of bread, curdling of cheese, and brewing of beer)[4] and medical applications (such as killing disease-causing microorganisms, promoting wound healing, and diagnosing certain diseases)[5].

1.2.2 Homogeneous catalysis

In homogeneous catalysis, the catalyst and the reactants are both in the same phase[6], which is mostly liquid phase, but also gas phase (sometimes even in the solid phase). There are an extended variety of homogeneous catalysts, ranging from Brønsted and Lewis acids (which are widely used in organic synthesis), to transition metals, organic molecules and organometallic or coordination complexes[6].

The advantages of these catalysts include an excellent selectivity and a high and uniform dispersion of the catalyst throughout the reaction mixture, allowing the maximum number of collisions between reactants and catalyst and so and easy accessibility to all catalytically active sites[3]. However, they suffer from some disadvantages, such as corrosion, toxicity, poor thermal stability, difficult separation of the catalysis from solution after the interaction, high catalyst recovery costs, and the creation of solid waste[2]. Despite these problems, are still used in the food, fine chemical, pharmaceutical, and agrochemical industries. Moreover, a number of commercially viable processes, mainly using transition metal compounds, have been developed in recent years, such as high-density polyethylene and polypropylene. The first industrial catalysed reaction, performed in 1750, was the oxidation of SO_2 to SO_3 using NO in the gaseous phase as a homogeneous catalyst (the so-called lead chamber process)[4]:

$$\text{Step 1: } 2NO_{(g)} + O_{2(g)} \rightarrow 2NO_{2(g)} \quad (1)$$

$$\text{Step 2: } 2NO_{2(g)} + 2SO_{2(g)} \rightarrow 2NO_{(g)} + 2SO_{3(g)} \quad (2)$$

$$\text{Overall reaction: } 2SO_{2(g)} + O_{2(g)} \rightarrow 2SO_{3(g)} \quad (3)$$

It is used for the manufacture of sulfuric acid (H_2SO_4)[5]:

$$SO_3 + H_2O \rightarrow H_2SO_4 \quad (4)$$

1.2.3 Heterogeneous catalysis

Heterogeneous catalysis involves systems in which the reaction takes place in different phases[6]: the catalyst is usually in a solid form, and the reaction occurs either in the liquid or in the gaseous phase[7]. This means that the rate-limiting step occurs at the solid surface, which is why heterogeneous catalysis is also referred to as surface catalysis[8].

Moreover, it implies many advantages compared to the homogeneous catalysts, such as their easy separation from the products and easy recovery[3]. Some example of processes that use heterogeneous catalysts are Fe with small amounts of Al_2O_3 and K_2O used in the Haber-Bosch process for the synthesis of ammonia from N_2 and H_2, but also the Fischer–Tropsch (FT) process to produce a variety of hydrocarbons[8].

Heterogeneous catalysts may be used as fine particles, powders, granules. They may be used in bulk form (unsupported catalysts) or be deposited on the solid support (supported catalysts)[9]. The first occupy the large section of industrial catalysis (e.g., Raney nickel in the hydrogenation of glucose to sorbitol[10]), while the second are mainly used in hydrogenation, hydrogenolysis, dehydrogenation, reforming reactions, and cracking of petroleum hydrocarbons. Some common heterogeneous catalysts are metals, metal oxides, metal salts, or organic molecules. Noble metals, such as Pt, Pd, Rh, Ni, Co, and Ir, are superior heterogeneous catalysts[11]. They have been extensively used in the chemical and petrochemical industry for the production of energy and fuels, and commodity chemicals, but also medicine production, and environmental technology[11]. However, due to the high costs and low abundance of such noble metals in nature, they cannot fulfil the increasing demand[12]. This is only one of the reasons why, even if unsupported catalysts occupy the large section of industrial catalysis, considerable scientific and economic interest is given to the supported catalysts and, in particular, to high-performing supported metal nanoparticles (M-NPs)[13]. In fact, the first purpose of using a carrier is to achieve a high dispersion of the metal as small metal particles (see *1.3.3 "The size effect in nanomaterials"*), so that smaller amounts of the often expensive active metal component can be used, which may also prove to be more economically favourable[10]. The second purpose is, of course, to provide a

structural framework to stabilize the metal both thermally and mechanically and to avoid it from sintering as well as to make it more robust, respectively[14]. The use of a support also increases the available metal surface area which can be directly related to the catalytic activity[15]. Choosing the appropriate support is a topic of main importance[16]. In most cases, it may be imposed by the type of reaction to be promoted. Typical support materials include carbon-based materials (such as carbon black[17], carbon nanotube[18,19], carbon nanofiber[20], and graphene[21]), inorganic-based materials (such as zeolites or metal oxides like Al_2O_3, SiO_2, and TiO_2), and organic-based materials (such as polymers, *e.g.* polystyrene, copolymers, *e.g.* styrene-divinylbenzene)[9].

In some cases, the support only plays a physical role (such as silica) and is considered inert towards the catalytic process. In this case, the adsorption usually occur via low energy van der Waals interactions. However, depending on the material used, in most cases supports may also interact with the active metal (bifunctional catalyst, such as silica-aluminas, zeolites or chlorinated aluminas). In this case, the overall process is actually a combination of two functions: the one of the metal and the one of the catalytically active support[22]. One such example could be that Au catalyst supported on TiO_2 (i.e., a catalyst used in the methanol oxidation reaction), in which the TiO_2 acts not only as catalyst support, but also as a methoxy species reservoir for the reaction[23]. In general, when this occurs, metal–support interactions (MSI), provided by the interfacial sites actually acting as the bridge to connect the metal species and support[24], are in operation. The extent or strength of these interactions, can have significant effects on the catalytic performance[25]. The MSI has been widely exploited as a strategy to enhance stability, strengthen selectivity, and promote activity for various supported catalyst[24], influencing the electronic environment of the active sites (by introducing new active sites to the system, usually acidic or basic or both), changing the number of active sites, and influencing the morphology of the metal crystallites.

If an intrinsic size effect on catalytic properties is to be evidenced, much care should be taken to choose as much as possible an inert support and/or to avoid using conditions that could possibly induce any MSI. These precautions are often not sufficient, and also the conventional catalyst preparation methods are likely to not

allow having a good control over the size, shape, oxidation state and dispersion[13] of the metal particles, thus influencing both activity and stability of the catalysts[26]. One mechanism to achieve this control, is to utilise another nanotechnology, that of nanoporous materials (See *1.1.4.1 "Nanoporous materials"*), as well as enhanced and efficient preparation methods (such as the sol-immobilization).

1.2.3.1 Heterogeneous catalysis processes on a solid surface

Catalytic surface reactions mainly occur via three reaction mechanisms, i.e. Langmuir–Hinshelwood, Eley–Rideal or Mars Van Krevelen mechanism (Figure 2)[27]. The Langmuir–Hinshelwood mechanism proposes that both reactants first adsorb onto the surface and then, react to form the final product. Most catalytic reactions follow this mechanism. It consists of the following sequence of steps: (1) adsorption from the gas phase, (2) dissociation of molecules at the surface, (3) reactions between adsorbed molecules, and (4) desorption to the gas phase.

According to the Eley-Rideal mechanism, only one of the reactants adsorbs onto the surface; then, the other reactant interacts with the adsorbed species directly from the gas–phase or liquid phase. The sequence is the following: (1) adsorption from the gas phase, (2) dissociation of molecules at the surface, (3) reactions between gas and adsorbed molecules, and (4) desorption to the gas phase.

In the final mechanism (Mars–van Krevelen mechanism), the surface itself is an active part in the reaction: one reactant forms a chemical bond with the catalytic surface forming a thin surface layer of metal–reactant (1a). The other reactant now directly reacts from the gas–phase with the atoms from the chemically bonded reactant on the surface (1b)[28].

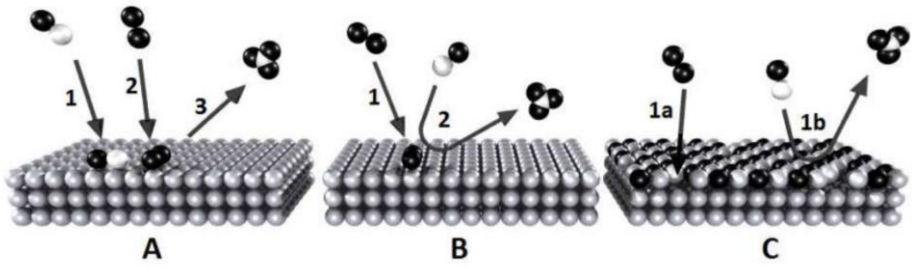

Figure 2. Langmuir–Hinshelwood mechanism (A), Eley–Rideal mechanisms (B) and Mars–Van Krevelen mechanism (C)[27].

1.3 Nanomaterials

In the following sections, some general concepts about nanomaterials are reported in order to underline their importance in scientific research as well as the influence the downsizing of metal sizes has on the performance of supported metal catalysts for a broad range of chemical transformations[24] needed for a future sustainable society After that, the fusion between nanoparticle and nanoporous materials technology is discussed[29].

1.3.1 History of nanomaterials

The term nanometer was first used in 1914 by Richard Adolf Zsigmondy[30].
In 1959, the American physicist and Nobel Prize laureate Richard Feynman was the first to introduce the concept of nanotechnology during the lecture ‘‘There’s Plenty of Room at the Bottom’’ presented in the American Physical Society’s annual meeting at Caltech. In his speech, he explained that our ability to work at the atomic and molecular levels it is not limited by the laws of nature, but it is rather a lack of appropriate equipment and techniques[31]. He imagined that huge amounts of information could be encoded onto increasingly small spaces, and that machinery could be made considerably smaller and more compact[32]. Due to this, he is often considered to be the father of modern nanotechnology.

In 1974, the Japanese scientist Norio Taniguchi might be the first person who used the term “nanotechnology” as: “the processing of separation, consolidation, and deformation of materials by one atom or one molecule[33,34].

On the wave of Feynman’s influence, the term was then popularized by the American engineer Eric Drexler, suggesting an engineering vision of the phenomenon[35] and directly inspiring numerous crucial scientific developments in the field of nanotechnology, among which the invention of the scanning tunneling effect

microscope (STM) in 1982, the atomic force microscope (AFM) in 1986, and the first images of single atoms using the STM (the Eigler-Schweizer experiment[36]).
The motivation to develop hard discs with high storage density stimulated the measurement of electrostatic and magnetic forces. This led to the development of Kelvin-probe-, electrostatic-, and magnetic-force microscopy[37].

1.3.2 Nanomaterials categorization

Nanomaterials can be classified according to the type of nanomaterials[38,39]:

- Carbon-based nanomaterials;
- Inorganic-based nanomaterials, mainly made of metal or metal oxide particles less than 100 nm;
- Organic-based nanomaterials excluding carbon-based nanomaterials (for example, dendrimers, micelles, liposomes, and polymers);
- Composite-based nanomaterials, which are multiphase complex nanostructures with one phase at least confined to the nanoscale range. The nanocomposites can be any mixture of carbon-based, metal-based, or organic-based nanomaterials and bulk materials of every kind and form (metal, ceramic, or polymer, etc).[40]

Furthermore, nanomaterials can be classified with respect to the number of dimensions which are not confined to the nanoscale range (> 100 nm) (Figure 3):

- Zero dimensional (0-D): length, breadth and heights are confined at single point and all three dimensions are in the nanoscale range (s *e.*, nanoparticles);
- One dimensional (1-D): only two dimensions in the nanoscale range, the other one (either length, breadth or height) not (*e.g.*, nanowires, nanorods, nanotubes);
- Two dimensional (2-D): only one dimension in the nanoscale range, the other two not (*e.g.*, nanocoatings, thin-film-multilayers).

Whereas, when all dimensions not confined to the nanoscale range, so they are all above 100 nm, it is the case of the three dimensional (3-D) materials, such as bulk material (e.g., sand, cement, salts, pigments, etc)[40].

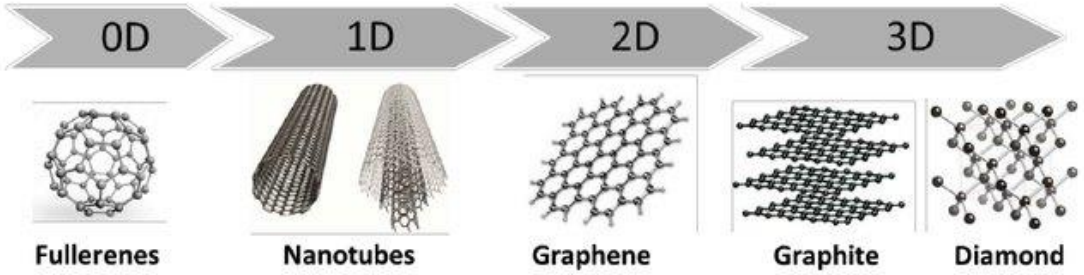

Figure 3. Crystal structure of carbon nanomaterials with different dimensions.[41]

1.3.3 The size effect in nanomaterials

Conventionally, most of the chemical-physical properties of the bulk-sized material is determined by their chemical composition and crystal structure and not by the surface atoms because they account for only a fraction of total atoms, so are considered plying a negligible role. Compared to their bulk counterparts[42], nanomaterials show very different and unique chemical, physical, optical, and electronic properties[43]. This is due to their size in the nano-scale, for which a greater proportion of atoms are present on the surface (Figure 4), which makes them no longer negligible.[44]

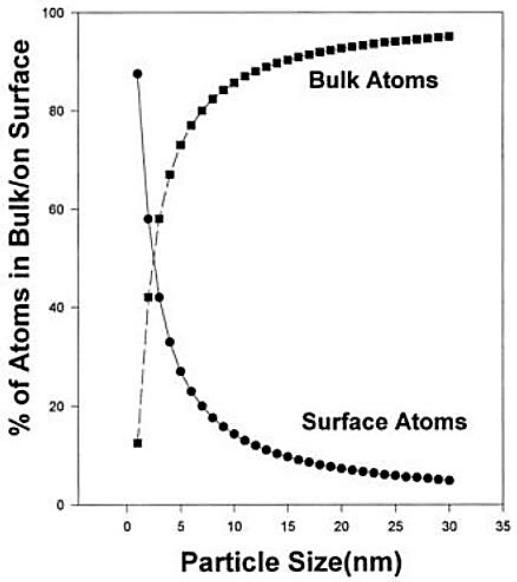

Figure 4. The percentage of atoms in bulk and on surface as a function of particle size[45].

A greater number of atoms present on the surface implies changes in the chemical and physical properties[46]. It entails increased surface area (surface-to-volume ratio) and quantum confinement effect[47]. Due to the huge surface area, all NMs possess a huge surface energy, which makes them thermodynamically unstable or metastable. Compared to the bulk materials, NMs' surface atoms have incomplete bonds due to their low coordination number[48], meaning they are more chemically reactive[49,50]. The relationship between the NMs dimension and their distinctive properties can be expressed by the following equation[51] (eq.1):

$$\frac{E_t}{V} = e_i + \left(\frac{A}{V}\right) e_s \quad \text{(eq.1)}$$

, where E_t = total energy content of a solid [J],
e_i = internal energy per unit of volume [J/cm^3],
e_s = surface energy per unit of surface [J/cm^2],
V is the volume of the solid,
and A is its surface area.

The A/V ratio takes the name of dispersion F[51] and it represents the fraction of atoms on the surface with respect to the total number of atoms present in the sample. As the dispersion increases, in particular when it has a value between 106 -107 cm^{-1}, the surface energy acquires a significant relevance, justifying the different chemical-physical properties of the NMs compared to their bulk counterparts.
In addition to their chemical properties, NMs' small size and high surface energy affects some physical properties as well. For example, it:

- Makes NMs excellent supports for catalytic applications, since their high surface area allows a good dispersion of the active catalyst, and so enhances its performance substantially[52];
- Increases thermal and electrical conductivity; a material with high surface energy is energetically unstable and, in order to reach a state of greater equilibrium, tends to have phase transition at lower melting temperatures than macroscopic materials;

- Improves mechanical properties, including hardness (five times harder than their bulk counterparts, for which hardness does not depend on the particle size), fracture toughness and strength[53,54];
- Exhibit superparamagnetism, according to which sufficiently small nanoparticles can be magnetized in the presence of an external magnetic field, passing from being non-magnetic to magnetic[55];
- Increased permeability through biological barriers (membranes, blood-brain carrier), improved biocompatibility, and an excellent capacity to deal with pathogen-related diseases[56];
- Changes the optical and electronic properties, which may arise from the so called quantum confinement effect. According to this effect, as the size of the particles becomes comparable to the exciton Bohr radius (which is the separation between electron and hole in an electron-hole pair), the continuous band structure expected for an infinite solid crystal (bulk material)[57] becomes discrete and quantized (there is a splitting of the energy levels). As a result the optical band gap (also called Kubo gap) between two successive quantic energy levels becomes larger. The spacing is expressed by:

$$\delta = \frac{4E_f}{3n} \quad \text{(eq.2)}$$

, where E_f = energy corresponding to the Fermi level for massive matter , and n = total number of valence electrons of the nanocrystal.

The smaller the nanoparticles, the larger will be the Kubo gap. The more the energy level space increases, the more the system becomes confined.

These properties can be arbitrarily tuned via precisely controlling their size[58] shape (morphology), synthesis conditions, composition, and though an appropriate functionalization.

1.3.4 Applications

The increasing interest of scientific research towards nanotechnology has allowed it to establish itself as a field of science with versatile and widespread applications in different fields: from computer chips to medical uses, space exploration, and so on. It is also well-known for its considerable potential in materials manufacturing and behaviour improvement; in particular, in producing the so-called nanomaterials (NMs), *i.e.* engineered nano-sized and nanostructured materials.[59] Currently, a single and rigorous definition of the term "nano" is still under debate in the scientific community. In the absence of a generally internationally accepted definition[60], it is usually referred to single atoms or molecules or, more in general, to materials with size or with one of their dimensions in the range of 1 to 100 nm [31,42].

Nanomaterials seem to have been unknowingly used for various applications since ancient times: about 4000-4050 years ago they were used as ceramic mixtures reinforcement[61] or in an ancient hair-dyeing formula[38,62]. Nowadays, they have emerged as an exciting class of next-generation materials that are in high demand in materials chemistry for a wide range of practical applications, such as paints, surface coatings, electronics, cosmetics, environmental remediation, sports equipment, sensors, and energy storage devices[63].

1.3.4.1 Nanoporous materials

For decades, the technological and scientific potential of porous materials has fuelled the growing interest of materials chemists in the development of nanoporous materials[64]. The technological and scientific importance of porous solids arises from their ability to interact with ions, atoms, and molecules at their outer surface, while their interior is also accessible. A porous material is normally a solid composed of an interconnected network of pores (voids). Many natural substances such as rocks, clays, biological tissues (e.g. bones) and synthetic materials including ceramics, metal oxides, carbonaceous materials and membranes can be considered as porous media[29].

According to the pore size, porous materials can be generally divided into four main categories[65]:

- Macroporous materials, when they have pore sizes > 50 nm.
- Mesoporous materials, when they have pores between 2 and 50 nm.
- Microporous materials, when they have pore sizes < 2 nm.
- Nanoporous materials, when they have a pore diameter of less than 100 nm[66]

The generation of pores in the material can introduce outstanding features into the material that are absent in non-porous materials, including easily functionalized surfaces or high surface-to-volume ratios[67]. One of the most interesting expanding areas of research is the fusion between nanoparticle and nanoporous materials technology[29]. In particular, the use of nanoporous materials as supports for metal nanoparticles. The defined pore sizes and solid structure has the potential to immobilize and stabilize NPs, thus inhibiting NP aggregation, as well as allowing size/shape selective catalysis, which means controlling of size, shape and activity of the resulting NPs[29]. Furthermore, by selecting and manipulating the textural properties of the porous support (sometimes in unison with a reduction step), it should be possible to generate specific adsorption sites. The control of nanoscale activity and selectivity, potentially provides extremely efficient catalytic materials for specific applications in various fields, including environmental remediation, medicine, catalysis (production of commodity chemicals and energy) and sensors[29,68]. This is why, recently, research is focusing more on developing synthesis processes able to produce materials with precisely controlled pores for high-performance applications.

1.3.4.2 An example of porous material: mesoporous silica

Inorganic nanoporous materials include porous silicas, clays, porous metal oxides, and zeolites. Compared to other nanostructured materials, over the decades, porous silicas have emerged as a new generation of inorganic materials with potential applications as supports for catalysis, separation, selective adsorption, novel functional materials, and use as hosts to confine guest molecules. The widespread interest is due to the ordered and well-defined porous structure with large and uniform pore sizes of about

2.0–10.0 nm, narrow pore size distribution, their extremely high surface area (>700 m^2g^{-1}), their biocompatibility, biodegradation, biodistribution, and excretion properties, and their two functional surfaces (the cylindrical pore surfaces and the exterior surfaces). In this way, they surpass the small organic molecules as templating compounds and the pore-size constraint (<2.0 nm) of microporous zeolites[69].

The structure, composition, and pore size of these materials can be tailored during synthesis by variation of the reactant stoichiometry, the nature of the surfactant molecule, the auxiliary chemicals, the reaction conditions, or by post-synthesis functionalization techniques.

Mesoporous silicas' surface is heavily covered with many silanol groups that act as reactive sites[70], facilitate functionalization for the desired applications. Different types of silanol groups (single (a), hydrogen-bonded (b) and geminal (c)) are present on the surface of a mesoporous silica (Figure 5) and behave as weak Brønsted acidic sites[71]. It can be used in fuel cells, chemical engineering, ceramics, and biomedicine as excellent materials for use in drug delivery systems. It has been found that surface modification via introducing appropriate polymers or functional groups, such as CN, SH, NH_2, and Cl, can control drug release rate[72].

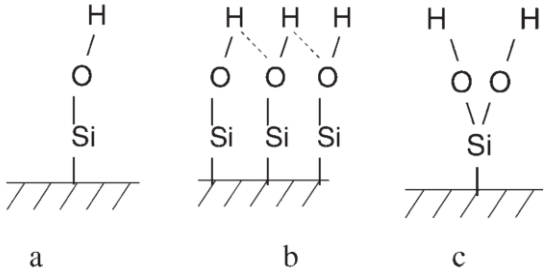

Figure 5. Schematic representation of single (a), hydrogen-bonded (b) and geminal (c) silanol groups present on the surface of mesoporous silica[73].

Mesoporous silica synthesis happens in the presence of surfactants as templates for the polycondensation of silica species, originating from different sources of silica: sodium silicate, alkoxides like tetraethylortosilicate (TEOS) and tetramethyl orthosilicate (TMOS). The characteristics of the porous structure (type of mesostructure, diameter and volume of the pores, wall thickness) and the morphology[74] can be controlled by changing the synthesis conditions, meaning reaction time[71], temperature[75], ionic

strength, pH, composition of the reaction mixture, source of silica, type of surfactant (MCM-41, MCM48 and MCM-50*). *MCM: Mobile Crystalline Material

Although it is possible to use the mesoporous silica in basic catalysis, most of the applications found in literature involve acidic catalysis[76], which is carried out by incorporation of strong acidic sites in the silica framework, such as aluminium (Al), into the lattice during or after the synthesis[73]. The tetrahedral substitution of Al in the mesoporous structure generates strong Brønsted acid sites, while the presence of tri-coordinated Al species in the framework can generate weak Lewis acid sites as it is illustrated in Figure 6. The incorporation of Al increases the catalytic activity of mesoporous silica, as well as its stability since it increases the pore wall thickness.

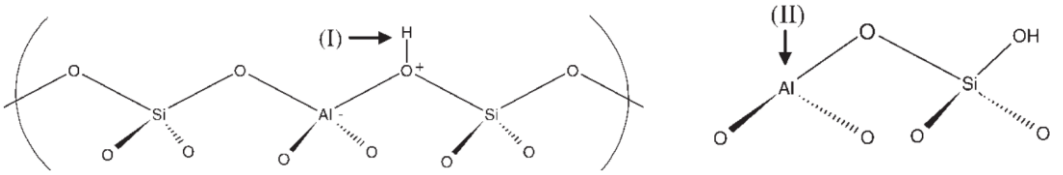

Figure 6. Representation of Brønsted and Lewis sites in mesoporous silica generated by structural tetra- (I) and tri-coordinated (II) aluminium, respectively.[73]

In the last decade, an important application corresponds to the use of mesoporous silica as template for the synthesis of carbon nanotubes[77],with the pores acting as a mold for the carbon nanotubes, and for this they need to be purified by acidic treatment. Furthermore, it has also been used as catalytic support for metallic clusters by impregnation [78], or by direct incorporation of a metal precursor into the silica structure by sol-gel process. The use of mesosilica as support is due to its high surface area allows a good dispersion of the active metal, generating metallic clusters of small size.

1.3.5 Synthesis of nanomaterials

During recent decades, the field of nanotechnology has been evolving every day, creating more and more powerful and optimized characterization and synthesis tools for producing nanomaterials with better-controlled dimensions[15]. The synthesis of nanomaterials can follow two different approaches: top-down or bottom-up.

1.3.5.1 Top-down approaches

The top-down approach refers to all the processes that involve the direct generation of the nanomaterial starting from the breaking down of the bulk system, using advanced miniaturization techniques such as lithography (involves the patterning of a surface through exposure to light, ions or electrons, and the deposition of material on to that surface to produce the desired material[79]) or mechanical methods (such as mechanical milling, laser ablation, etching, sputtering, and electro-explosion[80]). Most of the instruments use high-energy systems such as lasers or plasmas, which are economically expensive. On an industrial level, mechanical and thermal treatments are the most used ones, but despite the ease of processing, the materials obtained show inferior properties compared to those obtained with bottom-up techniques.[81]

1.3.5.2 Bottom-up approaches

The bottom-up approach (Figure 7) refers to all the physical and chemical processes that involve the building-up of the nanomaterial starting from single nanobuilding blocks (atom-by-atom or molecule-by-molecule) that self-assembly spontaneously through non-covalent interactions (typically hydrogen bonding, electrostatic attraction, and van der Walls interactions). Frequently, molecular self assembly exploits the principle of molecular recognition (chemical complementarity and structural compatibility)[82].

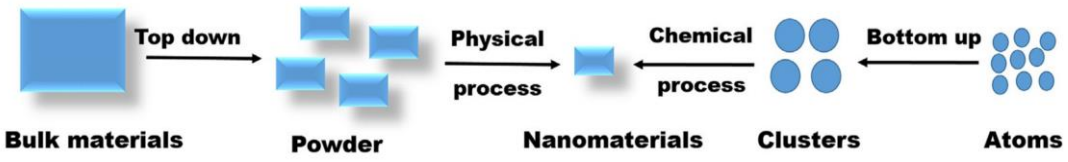

Figure 7. Synthesis of nanomaterials using top-down and bottom-up methods[83].

In the next paragraph, a series of bottom-up technique have been discussed.

1.3.5.2.1 Chemical vapor deposition (CVD)

Usually, CVD is an excellent method for producing high-quality and efficient supported metal NPs[84] on a wide range of organic and inorganic supports under very mild conditions (< 50°C). The method involves the vaporisation (sublimation) of metals and growth of the metal NPs under high vacuum in the presence of an excess of stabilizing organic solvents (e.g. aromatic hydrocarbons, alkenes, THF) and/or reducing agent (e.g. H2), and then is deposited on the support. After the deposition, a heat treatment step occurs to burn the organic ligand presented in the metal precursor. A suitable precursor for CVD needs to have adequate volatility, high chemical purity, good stability during evaporation, low cost, a non-hazardous nature, and a long shelf-life. Moreover, its decomposition should not result in residual impurities[85].
CVD can generate highly dispersed metal catalysts with a relatively narrow particle size distribution (2–8 nm) in a controlled and reproducible manner[86]. However, the method is often limited by the vapor-pressure of the precursor and mass-transfer-limited kinetics[29].

1.3.5.2.2 Solvothermal and hydrothermal methods

Hydrothermal and solvothermal methods are both useful methods for producing nanostructured materials through a heterogeneous reaction at high pressure and temperature around the critical point[87]. However, the hydrothermal process is the most well-known and extensively used one[88,89]. The two methods are both similar: they are both generally carried out in closed systems (autoclave)[90], where processing conditions are controlled by adjusting temperatures and/or pressures. The only difference is that the hydrothermal method is carried out in an aqueous medium[91], while the solvothermal method in a non-aqueous medium. They both allow a precise control of NPs size, however it implies a high cost due to the expensive autoclave.

1.3.5.2.3 Sol–gel method

The sol–gel method is a wet chemical technique that is extensively used for the development of various high-quality metal-oxide-based nanomaterials.
The name derives from the fact that, during the synthesis of the metal-oxide nanoparticles, the liquid precursor (conventionally metal alkoxides) is transformed to a sol, which is then ultimately converted into a network structure that is called a gel[92].
The synthesis process requires several steps, starting with the hydrolysis of the metal oxide in water or in presence of an alcohol to form a sol. Then there's the condensation or polycondensation forming hydroxo- (M–OH–M) or oxo- (M–O–M) bridges, resulting in metal–hydroxo- or metal–oxo-polymer formation in solution (porous structures)[93], which are then left to age. During the aging process, polycondensation continues, with changes to the structure, properties, and porosity (porosity decreases, and the distance between the colloidal particles increases). After, there is the drying, in which water and organic solvents are removed from the gel. Lastly, calcination is performed and NPs are finally produced[94].
The factors affecting the final product are precursor nature, hydrolysis rate, aging time, pH, and molar ratio between H_2O and the precursor[95].

The sol–gel method is economically friendly and has many other advantages, including the low temperature required and being easy[94]. However, it does not allow complete control of the final dimensions of the NPs.

1.3.5.2.4 Co-precipitation method

The co-precipitation method is used to prepare bimetallic alloy NPs. It involves the simultaneous precipitation of two or more metal salts[96] using precipitation agents (like sodium hydroxide, ammonia, and others). Precipitates are then aged to produce bigger particles, which are then collected via filtration or centrifugation. To remove contaminants that might have precipitated along with the product and obtain high purity NPs, additional wash with ethanol, distilled water, or other solvents are

required[97]. Particles may continue to expand beyond nanoscale if coarsening and agglomeration are not controlled. To stop growth and, thus, improve the size distribution of the NPs, some capping or stabilizing agents can be added, such as surfactants, inorganic molecules, and polymers[77]. It allows to produce very small metal NPs with high metal loadings. During coprecipitation, great care has to be taken to prevent local fluctuations in the conditions caused by, for example, temperature gradients, insufficient mixing, or concentration gradients, which can cause additional nucleation events, different or inhomogeneous growth patterns, or the precipitation of different phases[97].

1.3.5.2.5 Deposition-precipitation (DP) method

The DP pathway involves the dissolution of the metal precursor in an appropriate solvent, followed by pH adjustment (i.e. within the range of pH 5–10) to achieve the complete precipitation in the hydroxide or carbonate form. The hydroxide is subsequently deposited on the surface of the support. The final solids are then washed, dried and calcined under a flow of H_2 to reduce NPs to elemental metal. Some advantages of this method are that, by controlling the pH, it is possible to produce small NPs, as well as it allows to produce catalysts with metal loadings that exceed those obtained by impregnation which is limited by solubility[98]. However, great care has to be taken to prevent local concentrations exceeding the critical supersaturation, which would cause bulk precipitation[96].

1.3.5.2.6 Impregnation (IM)

In the impregnation method a solution of the metal precursor is added to a support in a water solution. After impregnation, the excess of water and volatile species are removed by evaporation (drying process). The remaining product is calcined under air or H2 in order to allow the growth of the metal NPs onto the support. Depending on the volume of the initial solution contacted with the support, it is possible to distinguish two types of impregnation:

- Incipient wetness impregnation (IWI), also called dry impregnation or capillary impregnation, in which the volume of the solution is equal to the volume of the pores. This means using only the amount of solution necessary to fill the pores. It is referred to as the maximum water uptake and it is calculated by slowly adding water to the chosen support until it is saturated.
- Wet impregnation, in which an excess of solution is used compared to the pore volume.

It is widely used being a simple and practical procedure, it is easy to scale-up and it involves no washing. However, it allows low control of the particle size.[97]

1.3.5.2.7 Sol immobilization (SI) method

The sol-immobilization (SI)[99] represents an effective and largely used method to synthesize supported NPs with a narrow particle size distribution. Compared to conventional techniques, such as wet impregnation and deposition–precipitation, it allows an easy and good control of metal particle size before embedding them in the support, thus reducing the influence of the support on metal dispersion[100,101]. Since usually calcination is not necessary, the final materials maintain a well-defined morphology.

The process includes the preparation of the metal NPs through reduction of the metal salt precursor in presence of both a capping or stabilizing agent (polymer, surfactant, polar molecule, etc.) and a reducing agent (sodium borohydride [NaBH4], or hydrogen donors such as hydrous hydrazine and formic acid) and the subsequent immobilization on the NPs a support[102]. The capping agent has the role to both protect and stabilize the formed NPs, as well as enhance the dispersion regardless of the support. In some cases, the stabilizer can act also as reducing agent[16].

It is important to notice how the crucial point for obtaining good metal dispersion in this technique is the immobilization step. The latter depends on the surface properties and morphology of the support[100]. Normally the immobilisation is simply performed by dipping the support in the sol and metal particles adsorbed from the solution.

Many factors affect the kinetics of NPs adsorption such as the isoelectric point (IEP), the stabiliser and the surface area of support[103]. As a general trend, metal dispersion can be increased by increasing the functionalities of the support[104], as well as by choosing the adequate capping agent[103,105]. The choice of the stabilizer depends on the desired characteristics of the final product, but also on the specific properties of the metal/substrate pair. So it has to be paid attention both to its interaction with the particles and with the support chosen[100].

Many studies reported how polyvinyl alcohol (PVA) represents a quite versatile protective agent that is able to provide a good metal dispersion regardless of the support[106]. Other examples are poly(N-vinyl-2-pyrrolidone) [PVP], poly(acryl amide), poly(acrylic acid), and poly(ethyleneimine).

The stabilizer can be removed by thermal decomposition (>300 °C) or under milder conditions by solvent washing[107]. This last method has the advantage of limiting the coarsening of metallic nanoparticles that normally occurs during thermal treatment and is applicable to non-refractory supports.

Rogers et al.[108] prepared monometallic 1 wt% Pd/TiO_2 by the sol-immobilization method using PVA stabilizer and $NaBH_4$ reductant for the hydrogenation of 4-nonylphenol (4-NP) to 4-Aminopyridine (4-AP) and reported high activity compared with other catalysts prepared by different methods[109].

In this thesis work, the sol immobilization just discussed is the method that has been chosen to synthesize the catalyst to be used in the hydrogenation of CO_2 towards higher alcohols. This reaction is an important example of using CO_2 as a resource to be converted into value-added products, such as liquid and aromatic fuels. Much attention has been paid to this response as it not only effectively alleviates climate change but also reduces the over-dependence of industries on fossil fuels. The following sections focus on this theme, starting from the problem of the increasing concentrations of CO_2 in the atmosphere.

1.4 CO_2 as problem and valuable resource

1.4.1 CO_2 emissions

Inevitably, an expanding world population, along with the global economy and industrialization, leads to a constant increase of the energy and resources demands[110,111]. Unfortunately, due to their low cost and availability, fossil fuels (coal, natural gas and oil) are still the most significant source of energy and raw materials production on which the world economy rely to meet these needs through the chemical and petrochemical industry.[112] Fossil fuels' combustion from these facilities continues to be one of the factors that most contributes to the increase of carbon dioxide (CO_2) of anthropic origin in the atmosphere. In particular, for a power plant with equal capacity, the amount of CO_2 coming from coal combustion is much higher than the CO_2 produced from natural gas combustion[112]. This is important as increased CO_2 is believed to be the main cause behind the harmful effects on the environment that have led to climate change.

CO_2 can come from a variety of natural sources, making it naturally present in the atmosphere where it can linger from ten to thousands of years[113]. It is part of the Earth's carbon cycle, namely the continuous exchange of the carbon atom within the molecule through a complex series of natural processes among the many different natural reservoirs: the ones that absorb CO_2 from the atmosphere (with a process called "carbon sequestration") are called sinks (like plants, oceans and soil), whereas the ones that release CO_2 into the atmosphere are called sources (like volcanic eruptions)[114]. Moreover, CO_2 is one of the greenhouse gases (GHG): natural molecules that, despite constituting only about 1% of the atmosphere, have a significant impact on Earth's climate. This is due to their ability to absorb most of the infrared energy emitted from the Earth's surface (after having absorbed about half of the UV-Vis one coming from the sun) rather than letting it escape into space[115]. In this way, GHGs create a heat-reflective layer that insulates the planet (keeps the heat close to Earth's surface),

maintaining the Earth's climate (habitable) at a liveable temperature (warm enough to support most forms of life) and, in particular, at about 14°C[116].

However, based on analysis from NOAA's (National Oceanic and Atmospheric Administration, US) Global Monitoring Lab, the amount of these gases in the atmosphere is increasing dramatically[117]. As a result, Earth's incoming and outgoing radiation is out of balance: more infrared radiation is absorbed and less escapes directly to space, causing an over-insulation and so an overheating of the planet. This is called the Enhanced Greenhouse Effect. CO_2 is responsible for over 60% of the "enhanced greenhouse effect"[118].

According to the Intergovernmental Panel on Climate Change (IPCC), the United Nations (UN) body for assessing the science related to climate change, CO_2's abundance and, most importantly, persistence in the atmosphere makes it the most responsible for the Enhanced Greenhouse Effect and climate change[119], and so the most dangerous and prevalent greenhouse gas (GHG), despite not being the most powerful one in terms of global warming potential (GWP):

- Methane (CH_4). Even if it doesn't stay in the atmosphere as long as a molecule of CO_2, is 25 times more powerful in terms of GWP. It accounts for about 16% of all GHG emissions coming from landfills, petroleum and natural gas (of which it represents the main component) industries, and agriculture.
- Nitrous oxide (N_2O), whose lifetime in the atmosphere exceeds a century, is 298 times more powerful than CO_2 in terms of GWP. It accounts for about 6% of the global GHG emissions coming from agriculture and livestock, including fertilizer, manure, and burning of agricultural residues.
- Industrial gases, such as fluorinated gases, meaning hydrofluorocarbons (1430-14800 times), perfluorocarbons, chlorofluorocarbons, sulphur hexafluoride (SF_6), and nitrogen trifluoride (NF_3), have heat-trapping potential thousands of times greater than CO_2. SF_6 is the most potent one, with a GWP 22800 times bigger than a molecule of CO_2 and stay in the atmosphere for hundreds to thousands of years. Accounting for about 2% of all emissions, they're used as refrigerants, solvents, and in manufacturing.

- Other GHGs include water vapor and ozone (O_3). Water vapor is actually the world's most abundant GHG, but it is not tracked the same way as other GHGs because it is not directly emitted by human activity and its effects are not well understood. Similarly, ground-level or tropospheric ozone (not to be confused with the protective stratospheric ozone layer higher up) is not directly emitted, but emerges from complex reactions among pollutants in the air[120].

Since the Industrial Revolution in 1750 to today, the amount of CO_2 has rapidly and aggressively increased of about 49.40%: from 280 ppm or less (before the start of the Revolution) to 418.33 ppm in February 2023 (the highest levels ever recorded) and will increase up to 750 ppm until 2100[117,121–123]. Twenty countries are responsible for at least three-quarters of the world's greenhouse gas emissions, with China, the United States, and India leading the way. The figure below (Figure 8) makes it clear that the current trend must be broken down if we want to prevent the disastrous effects of climate change on the habitability of our planet: not only the rising average earth's temperature we refer to as global warming prospected to increase by about 1.9°C[124]; but also the extreme weather events (such as droughts, floodings due to more frequent and intense heavy precipitation events, rising of the average sea levels by about 3.8 m, and retreat of glaciers and Arctic ice), the shifting of wildlife populations and habitats, the disruptions of food supply, the increased wildfires, and the alteration of the carbon cycle (the CO_2 released in the atmosphere is about half more than the one that natural processes can remove). However, this it's still considered one of the biggest and most complicated challenges of the 21*st* century.

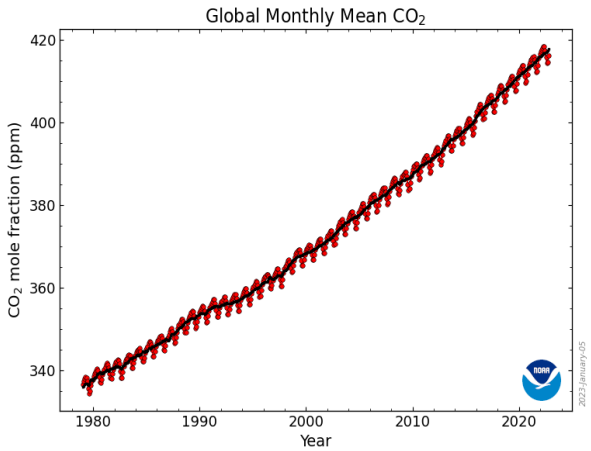

Figure 8: CO_2 global monthly mean since 1980. [Figure retrieved from NOAA's Global Monitoring Lab[117]]

1.4.2 Possible solutions

As just stated, one of the ongoing and prospective challenges would be implementing appropriate methods and strategies to mitigate greenhouse gas emissions. During the UN Climate Change Conference (COP21) in Paris, France, on 12 December 2015, in an attempt to solve this problem and move towards a climate neutral world, 197 parties signed the so called Paris Agreement[125], which aspires to limit the temperature increase to 1.5°C above pre-industrial levels[125]. This can be achieved if the GHG emission will peak before 2025 at the latest, will decline by 43% by 2030 and reach net zero by 2050. Each sector of the global economy contributing to the GHGs to the atmosphere, from manufacturing to agriculture to transportation to power production needs to evolve away from fossil fuels and swap to renewable sources, such as wind, solar, geothermal, biomass, and biofuel energies. Besides the already mentioned carbon emissions they imply, GHGs potential depletion represents another big issue. The problem is that, as previously stated, the world's economy is currently based on these resources, which means that turning them off instantly wouldn't be economical favourable. Since the agreement demands short term solutions, besides boosting energy efficiency and discouraging carbon emissions by putting a price on them, according to the Integrated Assessment Models (IAMs), other pathways consistent with the Paris target rely on large-scale greenhouse gas removal (GGR) from the atmosphere (IPCC and Climate Change, 2014). GGR 'technologies', also known as negative emissions technologies (NETs), involve the direct or indirect removal of CO_2 from the atmosphere, thereby resulting in potential sources of negative emissions[126]. They can be divided into three different categories:

- Nature-based solutions, *i.e.* afforestation/reforestation (AR), soil carbon sequestration (SCS)[127,128], coastal blue carbon[129];
- Enhanced natural processes, *i.e.* enhanced weathering of minerals (EW) ocean fertilization[130], ocean alkalinisation, microalgae culture in photobioreactors, biochar and artificial photosynthesis.
- Technology-based solutions, *i.e.* bioenergy with carbon capture and storage (BECCS)[131], direct air capture (DAC)[132].

1.4.2.1 Afforestation/reforestation (AR)

Due to plants' ability to be both carbon sinks and storages as they grow, it is important to preserve and manage existing forests and grasslands. This can be done both by avoiding deforestation and/or by planting new trees. On one hand, old forests have accumulated more carbon and have more leaves to absorb CO_2 through photosynthesis, but on the other hand young forests grow rapidly removing much more CO_2 each year from the atmosphere than older forests covering the same area[133].

According to the United Nations definition[134], afforestation and reforestation refer to planting trees, respectively, in an area that hasn't been forest for at least 50 years and in a previously forested area which has been recently deforested for other uses. Because of their large carbon sequestration potential (through photosynthesis), AR are among the most promising natural climate solutions[135,136]. However, their effectiveness depends on several factors. First, the extent of changes in albedo (*i.e.*, the amount of solar radiation reflected by a surface) and incident radiation and precipitation, both changing at different latitudes. Secondly, biodiversity loss and carbon-storage potential, that in turn depend on the species chosen to be planted. From a carbon uptake perspective, it is always preferable choose fast-growing species that absorb more carbon faster[137]. However, it is important to take into consideration biodiversity and, so, the utilization of native species, so not to disrupt the ecosystem[138]. Lastly, AR depend on natural or artificial events that can disturb it, such as fires, droughts, or land use changes. All of these factors, together with the fact that it is difficult to monitor the storage potential and global contribution to atmospheric CO2 levels, may make AR a less attractive option for climate change mitigation.

1.4.2.2 Soil carbon sequestration (SCS)

SCS is a well-known process that relies on adopting improved management practices that increase the amount of carbon captured from the atmosphere and stored in soil. Moreover, once the soil has reached saturation, these practices help keeping the carbon in the soil and avoid CO_2 to be released back to the atmosphere[139]. The advantages of

SCS include its potential beneficial effect in soil quality and crop yields[140], its low water footprint, that it can be applied without modifying land use and that it involves practices that are not only well-known and proven, but also easy and quick to implement. The main disadvantage of SCS is the limited storage capacity of the soil, which varies significantly, depending on where it is applied: the initial carbon capture rate is high, but it decreases until the soil has reached saturation[141], which generally happens after around 20 years[114].

1.4.2.3 Blue carbon

According to current studies carried out by NOAA (National Oceanic and Atmospheric Administration), coastal ecosystems (e.g. salt mangroves and coastal wetlands) annually sequester carbon at a rate ten times greater and in a quantity up to 3 to 5 times higher per equivalent area than mature tropical forests[142]. However, coastal development for housing, ports, and commercial facilities, is exposing them to an increasing destruction/damaging rate. This causes not only the loss in their carbon sequestration capacity, but also on the release of the carbon stored, which contributes to increased levels of GHGs in the atmosphere. This is why, conserving and protecting coastal habitats play an important role in reducing the effects of climate change[142].

1.4.2.4 Enhanced weathering of minerals (EW)

EW, first proposed in 1995, consists in spreading large quantities of pulverized alkaline materials (*i.e.*, silicate and carbonate minerals[143]) onto the Earth's surfaces (including extensive land areas or marine environments) to mimic and/or accelerate natural weathering processes. The latter is a slow carbonation process that is estimated to consume and absorb about one billion tonnes of CO_2 from the atmosphere every year. However, its realization implies great expenses due to necessity to mine, crush, transport and disperse the suitable rocks, as well as due to the damages to ocean ecosystems, the high water and energy consumption (comparable to coal mining), and the possible increase in the microbial organisms that produce GHGs such as methane and nitrous oxide. These carbonates may ameliorate ocean acidification, increasing its

alkalinity[144]. This is why EW leads to a higher uptake of atmospheric CO_2 compared to the one that would naturally occur. The rate of weathering depends on temperature, runoff (the availability of water to remove reaction products), grain size of rock or mineral and biological activity, like volcanoes.

1.4.2.5 Biochar

Biochar is defined as a carbon-rich material produced together with syngas and bio oil, during biomass pyrolysis[145]. Adding biochar to soils can improve their physicochemical and biological properties, which results in both an increase in their ability to absorb atmospheric CO_2 and in crop productivity due to the increased water retention[146], as well as the lower fertilizer requirements, which means reduction of N_2O and CH_4 emissions[147]. On the other hand, its high price and the detrimental effect its potential release can have on air quality due to wind and soil erosion inhibit its large-scale application.

1.4.2.6 Bioenergy with carbon capture and storage (BECCS)

Despite lacking of a singular definition, BECCS concept, first developed by Obersteiner[148] and by Keith in 2001[149], has come to be viewed as a key CO_2 removal approach. Generally, it involves:

1. Biomass production - from a residual product (e.g. sugar cane waste) or dedicated-energy crops (e.g. fast-growing tree species like willows trees) planted purely as a feedstock – which, as the plants grow, captures CO_2 from the atmosphere through photosynthesis.
2. Then, biomass is transported to the end-user or a conversion facility, where it's converted into renewable energy. In particular, it can be either combusted to produce heat or converted through digestion or fermentation to produce, respectively, gaseous or liquid fuels[150].
3. The CO_2 coming from these processes is then captured and stored. If the CO_2 stored is greater than the CO_2 emitted during biomass production, transport, conversion, and utilisation, it can lead to net negative emissions[151].

1.4.2.7 Carbon capture, utilization, and storage

In general CO2 can either be captured from point sources with a high CO_2 partial pressure, e.g. power plant or industry exhaust gases, or can be obtained directly from the air via direct air capture (DAC) technologies. DAC requires much higher energy inputs and the processing of greater gas volumes[152], which means higher costs (up to ten times higher). It is difficult to estimate the costs of CO_2 from different carbon sources due to the variety of capture technologies location-specific circumstances and variable energy and utility costs.

Originally developed for air pre-purification in air separation units and for trace CO_2 removal in confined spaces, the use of direct air capture (DAC) for global warming mitigation was first introduced by Lackner in the 1990's[153]. DAC is a method of removing CO_2 from the atmosphere using either liquid solvents operating at high temperatures (300°C-900°C) or solid sorbents (e.g., zeolites, activated carbon (AC), metal organic framework (MOF)) operating at ambient-to-low pressures and medium temperatures (80-120°C). When air moves over these chemicals, they selectively react with CO_2 and trap it, allowing the other components of air to pass through. Once CO_2 is captured, a heat treatment (above 800°C) is applied to release it from the solvent or sorbent, which can then be used for another capture cycle[152].

Nowadays, DAC has become a research hotspot, despite its many disadvantages: the sorbents can degenerate due to chemical stability after thousands of working cycles, affecting the sorption performance[154]; the low CO_2 concentration in the atmosphere (~400 ppm) requires large loading sorbents and high specific energy demand during the thermal regeneration process[155].

However, it has also many advantages: compared to BECCS and Coastal blue method, it does not require arable land and does not have to be near a coastal region, respectively. Moreover, unlike carbon capture and storage (CCS) that captures CO_2 from large point sources (meaning a specific process or group of processes), DAC technology can do it from any point or distributed sources (however, ideally this would be in proximity with both an energy source and CO_2 storage site). This means that existing industries that operate on a relatively small scale do not need to modify their

processes; CO_2 producing facilities that are geographically remote do not require extensive CO_2 transport infrastructure; DAC facilities can be co-located with renewable energy generation facilities to reduce transmission losses, and/ or with CO_2 storage facilities to minimise transport costs and infrastructure.

Going back to the process, the pulled CO_2 can be injected deep underground and permanently stored in geologic formations[156]. This is the end that most of the CO_2 should have in order to maximize DAC's climate change mitigation strategies. When combined with geological storage of CO_2, DAC is known as direct air carbon capture and storage (DACCS or DACS).

1.4.3 CO_2 utilization

Instead of "simply" being stored, the captured CO_2, can also be used as an available waste resource. That can be done both in a direct way (i.e. no chemical alteration) by using it, for example, in plastics, concrete or carbonated beverages, or in an indirect way as a cheap raw material that can be transformed into various high-value added products, in combination with renewable energy sources[7,8].
In this case, CO_2 can be supplied via the integration with various chemical plants, such as ammonia production plants or the cement industry, as well as steel and iron plants[9] or industrial and municipal wastes[10]. This route is a key strategy to not only reduce the concentration of atmospheric CO_2 through the utilization of CO_2 as feedstock, but also relieving chemical industry's dependence on fossil fuels as the main source of carbon building blocks for energy and useful chemicals production[11]. Moreover, even if would quickly lead to the release of carbon back into the atmosphere, the emissions will also be correspondingly lower compared to the petroleum-based ones.

Nowadays, CO_2 can be used to synthesize several products, such as methanol, ethanol or higher alcohols (used as clean and multipurpose fuels), but also formic acid (FA), dimethyl ether, polyols for polyurethanes, urea, carbonates. It can also be used to

produce liquid hydrocarbon (C^{5+}) fuels including gasoline (C^{5-11}), jet fuel (C^{8-16}), and diesel (C^{10-20}), wildly used as transportation fuels around the world[157,158].

Using CO_2 as a feedstock has many advantages. First, it is inexpensive, abundant, non-toxic, non-corrosive, and non-flammable and, therefore, safe to use[159]. However, CO_2 reaction mechanisms might be quite complicated due two intrinsic drawbacks: CO_2 high kinetic inertness and exceptional thermodynamic stability due to its low standard enthalpy of formation, ΔH_f = - 393.5 kJ/mol[160], and its low Gibbs energy of formation, $\Delta G°$ = - 400 kJ/mol[161], its linear structure of CO_2 with two strong double carbon-oxygen bonds (O=C=O)[12] with an average bond dissociation energy of 782.4 kJ mol^{-1} (or 391.2 kJ for each shared pair of electrons). Thus, exergonic CO_2 conversion reactions are quite difficult to be obtained, and its related industrial processes likely require a substantial energy input, optimized reaction conditions, and a catalyst with high stability and activity are required for converting CO_2 into value-added chemicals. Often the processes are more energy-demanding than the conventional ones, thus, requiring in higher operational costs and, sometimes, resulting in even higher CO_2 emissions[162].

CO_2 molecule can be used either as a weak acid or as an oxidizing agent, and it can be activated over catalyst surface through several activation methods, each generally leading to a characteristic reactivity of CO_2 and products due to the unique form of activated CO_2 during transformation[13]:

- Chemical (thermal) activation, which in turn can be divided into acid-base or metal activation, consisting in using metallic or acid-base catalysts, respectively;
- Electrochemical activation through electro catalytic processes;
- Photochemical activation through photo catalytic processes;
- Plasma activation[163].

1.4.4 CO_2 hydrogenation

In the following sections, a focus on the reaction on which this work was based is done. This is the CO_2 hydrogenation reaction to alcohols using renewable hydrogen.

1.4.4.1 The use of renewable H_2

CO_2 catalytic hydrogenation is the point of interest in this scenario. To ensure a neutral or negative carbon balance, the required H_2 should originate from a carbon neutral process such as from water dissociation by electrolysis using a renewable source of electricity as well (wind, solar, waves, etc):

$$2H_2O \xrightarrow{\Delta,\ \text{electricity or } h\nu} 2H_2 + O_2 \quad \text{(R.5)}$$

In this way, it is also possible to store renewable energy on a large and long-term scale[164]. Furthermore, other H_2 sources can be biomass pyrolysis or steam/oxygen gasification processes and reforming of biomass-derived products[165]. Other routes are still under investigation. One of them involves the production of biological hydrogen by means of a biological process involving microorganisms activated by sunlight[166].

1.4.4.2 C^1 products and applications

In both academic research and industrial practices, great progress has been made in the CO_2 hydrogenation to C1 molecules, such as methane (CH_4), methanol (CH_3OH), and formic acid (FA)[167,168]. Methane is currently used to produce chemicals, heat, and electricity. It is primarily obtained from natural gas, but it can also be synthesised through the so called methanation or Sabatier by reacting CO_2 with H_2 with H_2/CO_2 ratio equal to 4[169]:

$$(6)\ CO_2 + 4H_2 \rightarrow CH_4 + 2H_2O \qquad \Delta H_{298K} = -164.63\ \text{kJ/mol}$$

This reaction is carried out at a temperature of about 150−500 °C and pressure range from atmospheric pressure to 100 bar usually with metal-based catalysts. Moreover, it predominantly require either a fixed-bed, a fluidized-bed, or a three phase reactor.

Despite being a well-known process, first introduced in 1900, its application as an appropriate route for CO_2 utilization is hindered due to the large H_2 consumption, lower energy per unit volume and difficulties in storage compared with oxygenates (methanol, DME).

Methanol is one of the main raw materials in chemical/petrochemical industries, considered to be the transition molecule from fossil fuels to renewable energies[170]. The reason behind it lies in its extensive applications as solvent, carrier for hydrogen storage, as an easily transportable fuel (as a liquid, it can be handled and transported more easily than gases or solids[171]), and as C1 chemical feedstocks for the production of many valuable products and fuels: about 65% of the methanol produced worldwide is consumed for the production of acetic acid, methyl methacrylate, dimethyl carbonate, chloromethane, methylamines, dimethyl terephthalate, methyl terbuthyl ether (MTBE), fuel additives, and other chemicals[172]; the remaining 35% is converted into formaldehyde and the resulting products. In addition, methanol can be used to produce[166] ethylene and propylene via methanol-to-olefin (MTO) processes[173]. Currently, Carbon Recycling International (CRI)'s in Iceland is the largest CO_2-to-renewable-methanol plant, capable of producing 4000 t/year of methanol by converting about 5500 t/year of CO_2[174]. CH_3OH can be produced from several carbon-containing feedstocks, such as natural gas, coal, biomass, and CO_2. About 90% of methanol is produced from syngas (a mixture of CO and H_2) produced from gasified coal or natural gas, but the need of sustainable development is pushing for an alternative feed for methanol production. Today, there are many reports about methanol production by CO_2 hydrogenation[175] according to the reaction (7):

$$(7)\quad CO_2 + 3H_2 \rightleftharpoons CH_3OH + H_2O \qquad \Delta H_{298K} = -49.4\ kJ/mol$$

However, a more traditional route for methanol production is the gas-to-methanol process, where CO is obtained from CO_2 via the reverse water gas shift (RWGS) reaction and transformed to methanol as presented in (8) and (9):

$$(8)\quad CO_2 + H_2 \rightleftharpoons CO + H_2O \qquad \Delta H = 41.2\ kJ/mol$$

$$(9)\quad CO + 2\ H_2 \rightleftharpoons CH_3OH \qquad \Delta H = -90.6\ kJ/mol$$

Both (7) and (9) are exothermic reactions and involve a decrease of volume. This implies that they are both favoured at low temperatures and high pressures. CO hydrogenation is significantly more exothermic than CO_2 hydrogenation resulting in a higher cooling demand. For high CO_2 concentrations the methanol synthesis is inhibited by water formed in the RWGS reaction[176].

Reaction (8), instead, from a thermodynamic point of view, it's an endothermic reaction, which means $\Delta H° > 0$. This means it requires to work at high temperatures and, in particular, around 500°C because at low temperature the reaction would compete with methanation cited above (6)[177].

Fig. 9 below shows the maximum conversion determined by the chemical equilibrium for a CO- and CO_2-based feed gas. In the picture, the equilibrium limited methanol yield of CO_2 (18–58% at 200–250°C, 50–100 bar) is substantially lower than that of CO (55–89%). Based on equilibrium considerations, for the CO-based feed gas the highest methanol yield results from a H_2/CO ratio of 2, while for CO_2-based feed gas a H_2/CO_2 ratio of 3 to 1 is optimal[178].

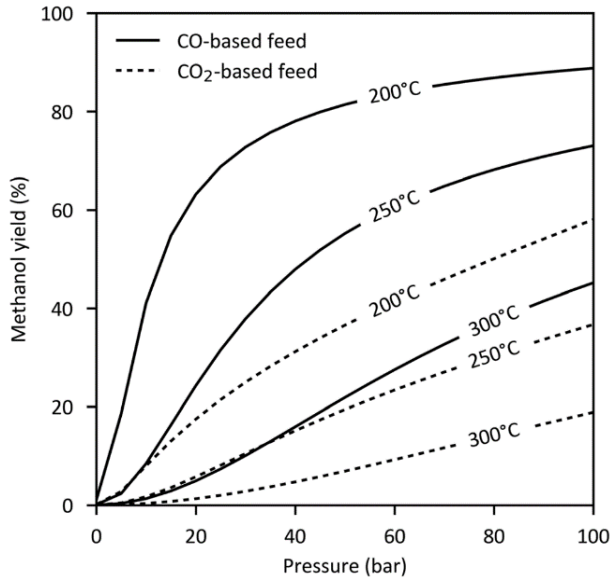

Fig 9. Equilibrium conversion of CO- or CO_2-based feed gas to methanol[178].

As reported by Ganesh in 2014[164], due to the strong C-O bonds, converting one mole of CO_2 to methanol requires an energy input of about 228 kJ and six electrons to reduce C^{4+} of CO_2 to C^{2-} of methanol.

Large impacts of reaction pressure and temperature on the catalytic performance can be evidenced. CO_2 hydrogenation to methanol ($CO_2 + 3H_2 \rightleftharpoons CH_3OH + H_2O$, $\Delta H_{298} = -49.5$ kJ/mol) is an exothermic reaction and the RWGS reaction ($CO_2 + H_2 \rightleftharpoons CO + H_2O$, $\Delta H_{298} = +41.2$ kJ/mol) is an endothermic reaction. Knowing that CO_2 is a stable, low-reactivity compound, a sufficiently high temperature is required to activate CO_2 by overcoming its energy barrier from the prospect of reaction kinetics. However, as the reaction temperature increases, even if the conversion of CO_2 increases, methanol selectivity decreases because the reaction competes with the simultaneous RWGS reaction, which depletes H_2 and generates H_2O, inhibiting methanol production. Therefore, developing an effective catalyst able to drive the CO_2 reaction under a relatively low operating temperature and moderate-pressure conditions is of crucial importance[179]. In addition to the catalyst material, another critical factor affecting the performance of CO_2 hydrogenation to methanol is the thermodynamic limitation, where a sufficiently high equilibrium conversion of CO_2 is not achievable under a moderate low pressure.

Currently, all commercially applied low-pressure catalysts are based on CuO and ZnO in most cases on a carrier of Al_2O_3 with variable stabilising additives and promoters like Zr, Cr, Mg and rare earth metals[180]. CO_2-based feed gases usually show lower space time yields (STY) in the order of 0.4–0.8 kg $l_{cat}^{-1}h^{-1}$ (40–100 bar GHSV around 10 000 h^{-1}), compared to 0.7–2.3 kg for the CO-based feed gases[181].

Catalyst impurities (residual amounts of alkalis), high pressures, high temperatures (requiring adequate control of the converter temperature), higher CO/H_2 and CO/CO_2 ratios, as well as lower space velocities (higher residence time), promote the formation of thermodynamically favoured by-products: higher alcohols (predominantly ethanol), esters (mainly methyl formate), ether (dimethyl ether), ketones (mainly acetone) and hydrocarbons[178].

In industrial applications, the common catalyst life time varies from 4 years[182] up to 8 years. Life time is limited by catalyst deactivation caused by thermal sintering and poisoning (blocking of active sites), which for copper catalysts is mainly due to

chlorides and sulphur compounds. In particular, sintering happens at temperatures above 227°C for copper and above 300°C for ZnO)[183]. Other examples of poisons reported in industrial applications are arsenic or carbonyls, causing a decrease of selectivity due to promotion of FT side reactions[184]. To protect the catalysts, a prior gas cleaning is done to remove these poisons and guard beds are often installed[185].

Methanol can also be converted to DME via catalytic methanol dehydration (10) based on either Langmuir-Hinshelwood[186] or Eley-Rideal[187] mechanisms:

$$(10) \quad 2\ CH_3OH \rightleftharpoons CH_3OCH_3 + H_2O \qquad \Delta H_{298K} = -23.4\ kJ/mol$$

DME is a colourless, non-toxic, non-corrosive ether, that can be employed as a clean fuel and chemical building block for the production of valuable materials such as light olefins (ethylene and propylene)[188], alkyl aromatics as a hydrogen source in fuel cells, methyl acetate and dimethyl sulfate[189].
As for formic acid, the hydrogenation reaction is the following:

$$(11) \quad H_2 + CO_2 \rightleftharpoons HCO_2H$$

The first report on CO2 hydrogenation to formic acid was by Farlow and Adkins in 1935 using Ni-Raney as catalyst[190].The renewed interest toward this process is mainly due to two advantages, involving the easy reaction conditions and its use as a potential liquid "hydrogen-carrier". The two reactions, namely CO_2 hydrogenation and FA decomposition into the starting CO_2 and H_2, give a quasi-CO_2-neutral cycle.

1.4.4.3 C^{2+} products and applications

CO_2 hydrogenation to C^{2+} higher alcohols (HA)[191–194] remain a great challenge in research[195]. This is due the lack of highly effective and selective catalysts with high stability, as well as for the complexity of various reaction routes and the uncontrollability of C–C coupling. Other than that, to promote the formation of HA, it

is required, prior to C–C coupling, a distinct balance between dissociative C–O bond adsorption and activation (alkylation) to get surface alkyl species and non-dissociative C–O activation (alcohol formation)[196] through CO insertion into *CHx to form CH_3CO* species, followed by CH_3CO* hydrogenation to ethanol[197]. Generally, the mismatching of these processes in kinetics and the existence of various side reactions (such as the formation of water that can easily deactivate the catalysts) would result in low activity and low selectivity of HA. Besides their production process being more challenging, higher alcohols have various advantages compared to other potential fuels, including higher energy density and lower toxicity compared to methanol. The most useful HA are C_2–C_5 alcohols, some of which can be used directly as transportation fuels, either alone or in gasoline blends, to extend gasoline supplies and enhance octane levels, thus improving the engine performance[198]. Among these C_2–C_5 alcohols, ethanol has been used as a fuel additive in many countries, such as the US, Canada, Brazil, and Sweden. Developing countries, such as China, have also started promoting ethanol gasoline[199]. These short-chain alcohols are also used as solvents or starting reagents in many chemical products. By contrast, long-chain alcohols (C^{5+}), mainly used as reaction intermediates and surfactants, are much less required. The demands of these HAs are foreseen to increase dramatically in the short run due to the growing world population[200]. Nowadays, ethanol, along with butanol, is primarily produced by fermentation of sugars from agricultural products such as potato, corn, and sugarcane[201]. The wide industrialization of this technology is hampered both by the food shortages, due to the large consumption of agricultural products, and by the huge investment required for the product- separation process. On the other hand, heavier alcohols are mostly prepared by commercialized-route involving the hydration of corresponding petroleum-derived alkenes over acid catalysts[202]. Because of increasing demands, alternative technologies for HAS have been explored, and some of them have met with industrialization. For example, the novel CuFe-based catalysts for the synthesis of mixed-alcohol via syngas, developed by the Institute of Coal Chemistry (Chinese Academy of Sciences). Furthermore, the Dalian Institute of Chemical Physics (Chinese Academy of Sciences) has built the first plant for ethanol production from coal with the indirect route, including coal to syngas, syngas to methanol/DME, methanol/DME carbonylation, followed by hydrogenation to

ethanol[203]. Even if much progress has been made both industrially and academically in the past few years, developing new more efficient catalysts is still under continuous investigation.

1.4.4.4 CO_2 to C^{2+} mechanism

The mechanisms for C^{2+} production generally involves two indirect pathways that are classified by the intermediates, as shown in Figure 10.

- Modified Fischer-Tropsch (MFT) process, in which CO_2 hydrogenation results first in CO formation (RWGS) and further direct hydrogenation of CO (Fischer−Tropsch synthesis, FTS) to hydrocarbons.
- Methanol-to-hydrocarbon (MTH) process, in which CO_2 hydrogenation results first in methanol, which is converted to hydrocarbons via further hydrogenation[203].

When CO serves as the intermediate to form C^{2+} hydrocarbons, there are several bottlenecks to overcome. Since RWGS and FTS are, respectively, endothermic and exothermic reactions, a major issue is to find the temperature region compatible for both reactions. Another bottleneck is to overcome the intrinsic limitation of traditional FTS process, which proceeds via surface polymerization of CH_x and usually produces hydrocarbons following the Anderson−Schulz−Flory (ASF) distribution. According to this model, the selectivity for target products is inevitably restricted by theoretical limits such as 58% for lower olefins, 45% for gasoline, and 30% for diesels[204]. To break this limit and control selectivity, bi-functional FT catalysts were first successfully proposed by Chang et al.[205] in 1978. They have multifunctional active sites that allow for the secondary reactions (such as oligomerization, isomerization, and aromatization), making possible to produce hydrocarbons with the certain desired carbon number range[206]. They contain metallic (syngas to alcohol) and acidic (alcohol to hydrocarbon) components[207].

When methanol is the intermediate to form long-chain hydrocarbons, the issue is the temperature since the high temperature (≥350 °C) kinetically required for methanol-to-olefins process, is thermodynamically unfavourable for CO_2 hydrogenation into methanol. A solution is to construct complementary active sites for CO_2 conversion to methanol and the subsequent MTH. The component for methanol synthesis generally involves metal oxides such as In2O3 and ZnO-ZrO2, whereas that for MTH comprises molecular sieves such as SAPO-34 and HZSM-5[191,208].

In addition to constructing multifunctional active sites for long-chain products, another promising strategy is to precisely construct the active site that comprises specific number of atoms within a proper distance. This strategy holds great potentials in breaking the theoretical limits of selectivity, especially for ASF distribution. For the active sites with geometric confinement, possibility of chain growth is likely to be highly sensitive to the length or configuration of the products. For example, dual Cu sites with a proper distance (2.70 ± 0.01 Å) enabled high selectivity (>99%) for ethanol[209]. Specifically, one Cu site adsorbed methanol, while the other adsorbed formyl species. During the formation of C−C bond, the formyl underwent a nucleophilic attack on the carbon of methanol[209].

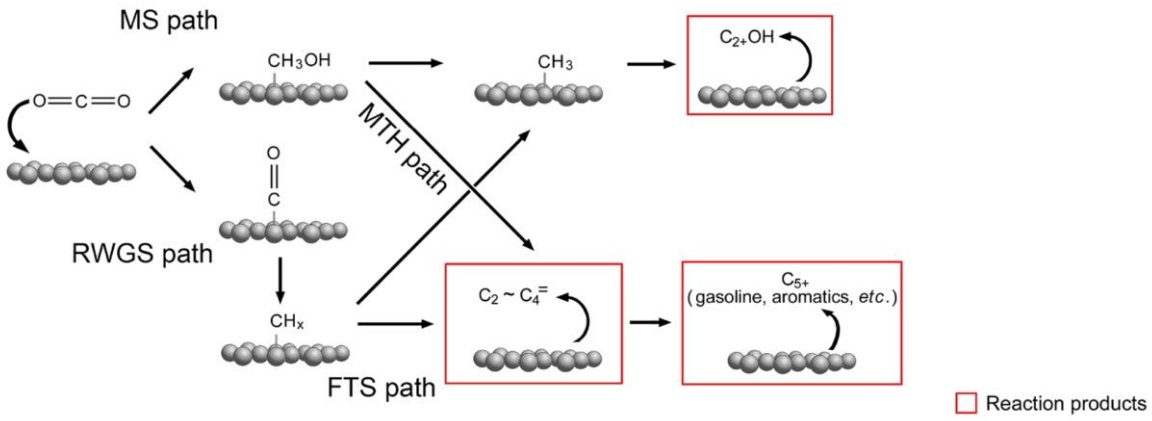

Figure 10. Reaction paths for the hydrogenation of CO_2 into higher alcohols, lower olefins, aromatics, and gasoline. The reaction products are enclosed in red solid lines[167].

1.4.4.5 CO_2 hydrogenation to C^{2+} catalysts

The synthesis of HAs requires rationally designed catalysts that are able to promote the CO_2 partial reduction to CO, the controlled growth of carbon chains (C–C coupling) and to accelerate the insertion of oxygen-containing intermediates (e.g., CHO*, CO) into the carbon chains (–OH group formation and insertion)[210–212]. Typical catalysts that exhibit preferable catalytic performances in CO_2 hydrogenation to HAs include Rh-based catalysts[213], Co-based FTS[214], Cu-based MS catalysts[215], and Mo-based catalysts[216] on metal oxide supports (e.g., Fe_2O_3, Co_3O_4, Al_2O_3, etc.)[217,218]. As a result, CO_2-to-HA catalysts are classified into four categories, namely noble-metal-based catalysts (Rh-based, Pt-based, Pd-based, and Au-based), Co-based catalysts, Cu-based catalysts, and Mo-based catalysts, respectively.

1.4.4.5.1 Rh-based catalysts

Rh-based catalysts have been widely used in selective CO hydrogenation to C^{2+} oxygenates due to their ability to simultaneously catalyse CO dissociation and insertion over their atomically adjacent Rh^0-Rh^{n+} species[219]. Among all HAs, ethanol is the dominant product over the Rh-based catalysts due to its relatively low C–C coupling ability[220]. According to the record, Rh-based catalyst used for CO_2 hydrogenation via syngas to ethanol was first reported by Tanabe et al.[213].

Recently, it was highlighted the importance of the support and, in particular, of the hydroxyl groups on the surface of support, presumably offering the stabilization of polar surface species, to improve ethanol selectivity in CO_2 hydrogenation[221].

Among various supports for Rh, SiO_2 was most often used[210,222,223], but also TiO_2 and Fe_3O_4[224–226], and mesoporous material (e.g., MCM-41) have been underlined. The synergism of high Rh dispersion and high-density hydroxyl groups on TiO_2 improves the reaction. Mesoporous material, instead, guarantees high dispersion of Rh nanoparticles owing to the high surface area over its mesoporous structure[223].

In general, CO_2 hydrogenation over unpromoted Rh catalysts mainly favours C^1 species (e.g., CO or CH_4). Thus, alkali and/or transition metals are required to shift the

catalyst selectivity toward C^{2+} oxygenates in CO_2 hydrogenation[196]. Several studies, confirmed Li, Fe[209,222,223,226], and V to be the most effective ones[210,223,224,227–230]. One of these was conducted by Arakawa et al.[210,222,224]. After an extensive screening of 28 promotors, they found Li-modified and Fe-modified Rh-SiO_2 catalysts to improve ethanol selectivity in CO_2 hydrogenation, respectively with 2–5 wt % and 3 wt % loading. In particular, the best results were obtained over the RhFe-SiO_2 catalyst at 5 MPa and 260°C, with CO_2 conversion of 26.7% and ethanol selectivity of 16.0%. According to the reported results, both Li and Fe addition can increase the electron density of Rh, leading to an increase the amount of bridged CO species[210]. For Li this means decreasing the number of unoccupied Rh sites for H_2 adsorption (suppressing methanation) and promoting CO insertion into CH_3– Rh, hence favouring the ethanol synthesis[210,224].

A significant improvement of CO_2 conversion of 12.1% and ethanol selectivity of 24.1% was also observed over the V-modified Rh/MCM-41 catalyst[223] at 0.3 wt % loading. V was found to promote the ethanol synthesis by forming the VO_x-Rh interfacial sites, which can also improve the fraction of Rh^+ species, enhancing CO adsorption. The amount of dissociative adsorbed CO was almost equal to the non-dissociative CO adsorbed, resulting in the highest ethanol selectivity and yield.

The best catalytic performance was obtained over RhFeLi/TiO_2 catalyst at 3 MPa and 250°C obtained 31.3% of ethanol selectivity and high stability after 20 h testing[221]. However, these catalysts are not ready for application because of the high cost of Rh.

1.4.4.5.2 Other noble-metal catalysts

Pd, Pt, and Au were also investigated in CO2 hydrogenation to HAS[213–215]. Aiming at reducing the high cost of commercial noble-metal catalysts, single-atom heterogeneous catalysts have been particularly explored in recent years[231]. An impressive catalytic performance in CO_2 hydrogenation to ethanol was obtained over Pd/Fe_3O_4 single-atom catalyst at 300°C and atmospheric pressure with ethanol selectivity of 97.5% and ethanol STY of 0.41 mmol $g_{cat}^{-1}h^{-1}$[232]. In comparison, Pd/Fe_3O_4 catalyst containing Pd nanoparticles demonstrated to be less selective to ethanol (<15%), with CO as the main product. In the study, it was theorized that Pd

single atoms and Fe_3O_4 constructed specific active sites for C–C coupling. The support might also help stabilizing the Pd single atom, reducing the chance for the surface moieties to diffuse across to other neighbour atoms for deep hydrogenation. Additionally, hydroxyl groups have also been proven to be favourable for improving alcohol selectivity in CO_2 hydrogenation[233–235]. However, as in general happens for single-atom catalysis, as the temperature increased, there was sintering of the Pd single atom on the surface leading to catalyst deactivation.

The catalytic performances of the catalysts reported above were all evaluated in fixed-bed reactors. However, recent studies proved that the catalyst and reactants/intermediates interaction may require sufficient contact time to achieve high HAS selectivity. This is why, recently, it has been investigated the use of batch-wise tank reactor in a solvent, which gives better results due to the recirculation. Wang et al.[226] found that for the tank reactor, the choice of solvent is an important factor that greatly affects the catalytic performance. They studied Au catalyst supported on TiO_2 and tested it at 6 MPa and 200°C with ethanol selectivity of over 99%, using DMF as the solvent. Compared with NMP, cyclohexane, THF, and water, DMF was the most appropriate solvent, exhibiting unique advantages for CO_2 dissolution and interaction between CO_2 and catalyst.

He et al.[218] tested Pt-Co_3O_4 in a tank reactor using different solvents. They found polar solvents, such as water, DMI, and NMP were better solvents for alcohol synthesis. They managed to obtain highest HAS selectivity of 72.0% was obtained in a water, outperforming those results tested in fixed-bed reactors. This may be due to the solvent stabilization, which may involve H-bonding to alcoholic species. In particular, $C^{2+}OH$ was obtained with high selectivity in water. The D_2O-labeling experiments proved that water was involved in the reaction and promoted the reaction kinetically by providing a hydrogen source.

Later, Bai et al.[236] developed Pd–Cu nanoparticles supported on TiO_2 obtaining outstanding catalytic performance, even at mild and clean reaction conditions (3.2 MPa and water as the solvent), with 92.0% of ethanol selectivity and 41.50 mmol $gcat^{-1}$ h^{-1} of ethanol STY.

1.4.4.5.3 Co-based catalysts

Co shows intrinsically very low RWGS activity, but strong hydrogenation ability, thus acting primarily as methanation catalyst in CO_2 hydrogenation[237,238]. Co-based catalyst catalysing CO_2 hydrogenation to ethanol were first tested by Arakawa et al.[239] with ethanol selectivity of only 7.9%. To improve the C^{2+} alcohol synthesis over Co-based catalysts, Ouyang et al.[240] tried synthesizing Pt supported on Co_3O_4. However, the results were not very promising: at 2 MPa and 200°C they obtained a C^{2+} alcohol yield of 0.56 mmol g_{cat}^{-1} h^{-1} and a $C^{2+}OH$ fraction of only about 22%. Using mesoporous Co_3O_4, improved the ability of carbon-chain growth and so increase of $C^{2+}OH$ yield (0.75 mmol g_{cat}^{-1} h^{-1}) and $C^{2+}OH$ fraction (41.8%)[241]. Co_3O_4 nanorods, synthesised by Yang et al.[211], showed low reducibility and high RWGS activity. Cu supported on Co_3O_4 nanorods catalysts exhibited CO_2 conversion of 13.9% with ethanol yield of 1.87 mmol g_{cat}^{-1} h^{-1}at 3 MPa and 250°C.

Another strategy to improve the C^{2+} alcohol synthesis was to vary the support in order to find the one that exhibited a strong interaction with Co to stabilize the active Co centers (the CoO or Co_2C phases) and suppress the complete reduction of Co_3O_4 to metallic Co and enhance HAs production. Several Na-promoted Co catalysts supported on different supports (Al_2O_3, ZnO, TiO_2, SiO_2, and Si_3N_4) were investigated in Co-catalysed CO_2 hydrogenation by Zhang et al.[242]. Among them, inert supports and, in particular, SiO_2, and Si_3N_4 were the most promising one to favour the formation and stabilization of Co_2C on their surface, which are known to be active sites in CO_2 hydrogenation to ethanol. However, as the temperature reached 400°C, Co_2C would be reduced to Co. Na–Co/SiO_2 showed 18.8% of CO_2 conversion, 8.7% of C^{2+} alcohols selectivity, and 87.5% of $C^{2+}OH$ fraction.

Furthermore, the pre-treatment conditions of catalyst was found having great impact on catalytic performance. Gnanamani et al.[243] revealed that catalysts activated by prolonged CO treatment exhibited the highest alcohols selectivity (73.2%) and $C^{2+}OH$ fraction (about 90%) due to the formation of cobalt carbide. By contrast, catalysts reduced by H_2 exhibited high methane selectivity (>70%) because of the formation of metallic Co.

Moreover, alkalis addition has proved to be very efficient in Co-based catalysts to improve the RWGS activity and suppress methanation, improving carbon-chain growth, regardless of whether the product is a HA or a HC[196,244]. Gnanamani et al.[243], comparing the structure differences of catalysts with or without Na^+ promoters before and after reaction by XRD and TEM, although cobalt carbide was produced in catalysts both with or without Na^+ after CO reduction. They concluded that Na+ is essential in preserving the cobalt-carbide phase.

1.4.4.5.4 Cu-based catalysts

Cu supported catalysts using metal oxides (such as ZnO, ZrO_2, and ZnO/ZrO_2) as supports, have the intrinsic tendency to favour the formation of C1 alcohols[196,199,245]. This is why, a great number of researches have been focused on modifying Cu-based catalysts in order to improve the ability of C–C coupling (the formation of CHx species, either from direct C–O dissociation or H-assisted C–O dissociation) and shift the main product to C^{2+} alcohols from syngas in fixed-bed reactors[246,247].

The Cu catalysts modification can be applied following two strategies:

(1) Alkali addition, which act as an active site for H_xCO-H_xCO coupling, as well as the non-dissociative activation of CO[248,249] and inhibit methanation by reducing hydrogen activation capacity through its coverage of the active sites[250,251]. The HAS selectivity over alkali-modified Cu-based catalysts has been shown to increase with the metal's basicity strength, i.e., Cs > Rb > K > Na > Li[252]. However, excess alkalis showed a negative effect toward HAS due to the severe coverage of active sites[248,253] and for most reported alkali-modified Cu-based catalysts, methanol was still the main alcohol product[246].

(2) FTS (Fe and Co) elements addition, which act non only as a promoter, but also as an active site for H_xC–H_xC coupling[254]. The Cu-Fe carbides interface facilitate the non-dissociative CO activation and CO insertion into surface alkly species to C^2-oxygenates and, thus, enhance ethanol selectivity in CO hydrogenation to ethanol[255]. To promote HAS it's important to control the Cu/Fe molar ratio and build abundant Cu–Fe interfaces[254].

Li et al.[14] used the K-modified CuZn catalyst in CO2 hydrogenation to HAS at 6 MPa and 350°C, obtaining C^{2+} alcohol yield of 7.3 mg $mL_{cat}^{-1}h^{-1}$ and $C^{2+}OH$ fraction of 28.1%.

Takagawa et al.[256] first reported the K/Cu– Fe–Zn catalyst with CO2 conversion of 44.2% and ethanol selectivity of 19.5% at 7 MPa and 300°C.

Some researchers reported the enhancement of the selectivity and yield of HA with the addition of K_2O promoters[250]. Guo et al. reported the K_2O-modified $CuZnFeZrO_2$ catalyst with K2O loading in the range of 0%–7%, suppressing MS and obtaining HA yield of 2.55 mmol mL_{cat}^{-1} h^{-1} and $C^{2+}OH$ fraction of 38.3% at 3 MPa and 320°C.

Xu et al.[15] recently studied the effect of Cesium (Cs) in CO_2 hydrogenation over CuFeZn catalysts, discovering its role in weakening the hydrogenation ability of catalysts, improving both CO2 conversion and product selectivity. They also studied the effect of Cu/Fe molar ratio on HAS and realized the best activity at a Cu/Fe ratio of 0.8. So they developed a Cs-$C_{0.8}F_{1.0}Z_{1.0}$ catalyst (3 wt %) and tested it at 5 MPa and 330°C, obtaining HA yield of 1.47 mmol g_{cat}^{-1} h^{-1} and HA fraction of 93.8%.

Li et al.,[16] studied the effect of Fe promoters on CO_2 hydrogenation to HA and found out that the synergistic effect between Cu–Fe and Zn–Fe interactions led to the higher catalytic activity by forming more Cu and Fe carbides species. The best catalytic performance was obtained at 6 MPa and 300°C with the $CuZnFe_{0.5}K_{0.15}$ catalyst with a Cu/Fe molar ratio of 2. CO_2 conversion was 42.3%, alcohol selectivity 36.7%, HA yield 148.1 mg mL_{cat}^{-1} h^{-1} and HA fraction 87.1%.

Guo et al.[17] studied the optimization of the catalyst loading, finding that indicated that the HAS from CO2 hydrogenation can be effectively conducted over the optimal CZK(1.5)//CFCK(4.5)* two-stage bed Cu-based catalyst system due to the cooperative effect of both increasing the C-C coupling and product conversion. They tested it at 6 MPa and 350°C, obtaining HA yield of 72.4 mg mL_{cat}^{-1} h^{-1} and HA fraction 55.3%.

**For convenience, $Cu_{25}Fe_{22}Co_3K_3$ catalyst was denoted as CFCK and the $CuZnK_{0.15}$ catalyst was denoted as CZK[17].*

Metal Organic Framework (MOF)** supported Cu-based catalysts have also been widely used in CO_2 hydrogenation[257,258], but their selectivity is mainly directed towards methanol as the only alcohol product. Lately, An et al.[18] achieved a high

ethanol selectivity (over 99%) and ethanol STY of 87.9 mmol g_{cat}^{-1} h^{-1} at 2 MPa and 100°C by using MOF as a support (in particular Zr_{12}-bpdc*) and tank reactors. The latter exhibited better catalytic activity compared with the low C^{2+} oxygenates selectivity in fixed-bed reactors. Moreover, the higher catalytic activity was attributed to the cooperative nature of bimetallic Cu^{I} sites, which facilitated H_2 activation, but also the direct C–C coupling with the assistance of Cs promoters. By comparison, over the Cu^{0}-ZrO_2 catalyst, the agglomeration of Cu nanoparticles lead to the absence of ethanol product, which means that methanol was the main product.

*** MOFs are crystalline extended structures constructed by stitching together inorganic polynuclear clusters, named secondary building units (SBUs), and organic linkers by strong bonds. SBUs help to build potentially porous periodic networks by linking organic ligands.*

**[1,1'-biphenyl]-4,4'-dicarboxylate (bpdc)*

Additionally, zeolites as supports have been applied in direct hydrogenation of CO_2 to ethanol. Recently, Ding *et al.*,[194] reported a highly active Cu-based catalyst applied in fixed-bed reactors: the Cu@Na-Beta catalyst with 2–5 nm Cu particles embedded in the Na-beta zeolite. They tested it at 2.1 MPa and 300°C, obtaining a high ethanol selectivity of 79% and ethanol STY of 8.65 mmol g_{cat}^{-1} h^{-1} with CO as the only by product. The "entrapment" of the small Cu particles in the porous structure of zeolite stabilizes the active surface, promoting the reaction of adsorbed CO_2 and methyl intermediates to ethanol.

1.4.4.5.5 Mo-based catalysts

Several studies use Mo-based catalysts (e.g., Mo_2C and MoS_2) for CO hydrogenation to HA[259,260]. However, there are only a few reports about Mo-based catalysts used for CO_2 hydrogenation to HA, which is due to the low CO_2 conversion and low C^{2+} alcohol selectivity obtained using these catalysts. Strong metal-support interaction, as well as the choice of the right solvent appears to be of great importance for the selective HAS. Moreover, alkali addition was theorized to play a dual role of both suppressing hydrocarbon synthesis and favouring alcohol formation, while the presence of Co contributed to the production of ethanol.

Tominaga *et al.*,[216] was the first to perform CO_2 hydrogenation to HA using alkali-promoted Mo-based catalyst, obtaining different HA selectivity.

Catafat *et al.*,[261] worked on CO_2 hydrogenation to alcohols using K-promoted $CoMoO_4$ catalysts, but the catalytic results were not very promising with only 7.2 % of CO_2 conversion and 6.5 % of ethanol selectivity.

Chen *et al.*,[262] tried to use Mo_2C supported metal (e.g., Cu, Pd, Co, and Fe) catalysts in tank reactors. The addition of Cu and Pd enhanced the production of methanol from CO_2 via formate intermediate, while Co and Fe enhanced the chain-growth ability and improved the formation of ethanol via CO intermediate.

Liu *et al.*,[263] used MoCoK sulfide catalysts at 5 MPa and 320°C, obtaining CO_2 conversion of 8.1%, C^{2+} alcohols selectivity of 15.9%, and $C^{2+}OH$ fraction of 27%.

1.4.4.5.6 Recap

As for the reactions carried out in a fixed-bed reactor, the catalyst groups can be ranked respect to their HA yields as follows: Cu-based catalysts > noble-metal catalysts > Co-based catalysts. Cu-based catalysts generally exhibit high CO2 conversion with moderate HA selectivity. Noble-metal catalysts show high HA selectivity but low CO2 conversion. Although Co-based catalysts exhibit comparable CO2 conversion, the HA selectivity is still too low due to the strong methanation ability. The “entrapment” of small Cu particles in the Na-beta catalyst showed outstanding catalytic activity with 79% of ethanol selectivity and 8.65 gcat-1 h-1 of STY, even at mild conditions (at 2.1 MPa and 300°C).

2 Aim of the study

The catalytic transformation of captured CO_2 to liquid fuels such as methanol, ethanol, and jet fuel using renewable energy can not only mitigate worldwide climate change by reducing carbon emission through the utilization of CO_2 as feedstock, but also decrease the industries enormous reliance on fossil fuels.

Given the overall low efficiency of the available catalysts for the CO_2 hydrogenation to higher alcohols process, the aim of this thesis project was investigating new catalysts and, more importantly, alternative catalyst synthesis methods. This is done in an attempt to enhance the commercial ethanol production since it represents a highly valuable way to lower CO_2 emissions.

Conventional techniques, such as wet impregnation and deposition–precipitation, although easy to apply, do not allow a good control over the size of the metal NPs. This is why, as synthesis method, sol immobilization was chosen. This technique allows, instead, a good control of metal particle size before embedding them in the support, thus reducing the influence of the support on metal dispersion. Moreover, for an even higher dispersion of Rh nanoparticles, a high-surface-area support (mesoporous silica) was chosen.

Following the indications given by the literature, as well as the footsteps of the catalytic testing performed by the previous students in the research group, Rh-based catalysts have been chosen as metal catalyst. In particular, supported Li-doped rhodium nanoparticles both mono- (Rh/mesoSiO$_2$@Li) and bi-metallic (RhFe/mesoSiO$_2$@Li) with a nano-alloy morphology. Fe and Li have already been tested before and displayed promising promoting behaviour at lower[210,222,264].

To synthesise RhFe alloy nanoparticles, a hybrid method that combines sol immobilization with impregnation was developed.

Apart from the synthesis method, this study focused on how the morphology of the support, as well as the reaction conditions, the molecular weight of the active phase and the presence of promoters can influence the catalytic activity of the catalyst in the CO_2 hydrogenation reaction. In the end, several characterization techniques (TEM, XPS, BET) were performed to gain insight into the characterization of the material.

3 Experimental part

3.1 Catalyst Selection

After a catalyst screening, Rh-based catalysts on a mesosilica support were chosen to perform the CO_2 hydrogenation reaction. From literature results, Rh showed adequate ethanol selectivity and seemed not to produce higher hydrocarbons at low pressures. Noble metal elements such as Rh are generally known for their ability in activating CO_2 and catalysing C-C coupling[19]. The second reason for choosing this catalyst was to then be able to compare it with the Rh-based catalysts on commercial silica support previously studied in the research group.

To identify the role of each component in the catalyst, thirteen different catalysts were prepared. The tested catalyst are summarized in the following table:

Rh/SiO2	**Rh/mesoSiO$_2$**	**Rh/mesoSiO$_2$@Li**	**Rh1Fe1/mesoSiO$_2$@Li10**
Rh0.25/SiO$_2$	Rh0.25/mesoSiO$_2$	Rh1/mesSiO$_2$@Li0.5%	Prepared with Sol-immobilization + IWI
Rh0.5/SiO$_2$	Rh0.5/mesoSiO$_2$	Rh1/mesoSiO$_2$@Li1%	Prepared with IWI + Sol-immobilization
Rh1/SiO$_2$	Rh1/mesoSiO$_2$	Rh1/mesoSiO$_2$@Li10%	
		Rh2/mesoSiO$_2$@Li10%	
		Rh3/mesoSiO$_2$@Li10%	

Table 1. Summary of all catalysts synthetized in this study.

It is possible to notice how, for the catalyst screening, the same catalyst was tested at different loading of active phase (Rh) and Li promoter. In particular, the test was done first on 0.25wt% Rh, then on 0.5wt% Rh, and finally on 1wt% Rh catalysts supported on meso-SiO_2 at 20 bar for a temperature range that goes from 180 °C to 250°C. Afterwards, the same amount of Rh (Rh 1 wt%) was maintained increasing the amount

of Li promoter (before 0.5%, then 1% and then 10% of Li) in order to find the minimum amount of promoter at which a significant catalytic improvement is showed. After having selected the desired amount of Li to add, Rh catalyst on mesosilica with 10% Li was tested this time increasing the amount of active phase: first 1Rh wt%, then 2Rh wt% and finally Rh3 wt%. The pressure adopted was always 20 bar, but this time the temperature chosen was only one (250°C).
Later, a bi-metallic catalyst was synthesised using Fe as second metal and maintaining the same amount of Rh (1 wt%) and the same amount of Li promoter. An attempt was done to synthesise the same catalyst adopting two different synthesis methods: first using sol-immobilization method and then incipient wetness impregnation method, and then viceversa.

3.2 Catalyst synthesis (synthetic protocols)

All the synthetic procedures described are conducted in the chemical laboratory in the building 67 of the Catalysis Engineering department of Applied Science at TUDelft University of Technology in Delft, Netherlands. The methodologies follow a green and safe approach (risk of category 2) and have been widely optimized and employed in several papers[265–267].

3.2.1 Solvents and reagents

Pluronic-p123 (Poly(ethylene glycol)-block-poly(propylene glycol)-block-poly(ethylene glycol), MF: $C_7H_{16}O_4$, MW: 164.2g/mol), Hydrochloric Acid (HCl, MW: 36.46g/mol), TEOS (Tetraethyl orthosilicate, MF: $C_8H_{20}O_4Si$, MW: 208.33g/mol), Lithium Chloride (LiCl), Rhodium(III) Chloride Trihydrate ($RhCl_3 \cdot 3H_2O$), polyvinyl alcohol (PVA, Mw: 13000-23000), Sodium Borohydride ($NaBH_4$, MW: 45.87g/mol), Iron Chloride ($FeCl_3$, MW: 162.2g/mol), Iron(III) nitrate hydrate ($Fe(NO_3)_3 \cdot 7H_2O$, MW = 367.9667 g/mol).

3.2.2 Meso-SiO_2

A Pluronic-p123 (Poly(ethylene glycol)-block-poly(propylene glycol)-block-poly(ethylene glycol)) solution was prepared by dissolving 6g in 134 ml of distilled water previously acidified with HCl (1M). The mixture was heated at 40°C overnight. After, to obtain a polymeric solution, 9 mL of TEOS (Tetraethyl orthosilicate) was added. The solution was covered and stirred overnight at 60°C. Subsequently, the reaction mixture was dried in air for 24h to complete the crosslinking. At the end, the solid obtained was dried in the oven at 80°C overnight. The as-prepared product was treated in the muffle with the following heating route: 1 step, heating at 5°C/min to reach 600°C; 2 step, isotherm at 600°C for 5 hours.

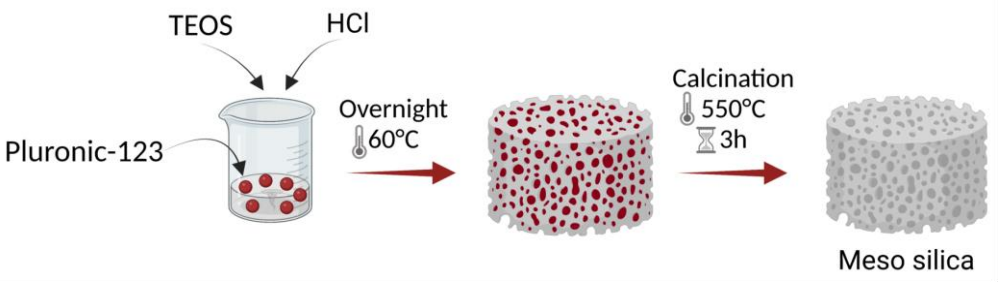

Figure 11. Synthesis of support.

3.2.3 Meso-SiO_2@Li

A Pluronic-p123 (Poly(ethylene glycol)-block-poly(propylene glycol)-block-poly(ethylene glycol)) solution was prepared by dissolving 6g in 134 ml of distilled water previously acidified with HCl (1M). The mixture was heated at 40°C overnight. After, to obtain a polymeric solution, 9 mL of TEOS (Tetraethyl orthosilicate) and LiCl were added, different amount of the lithium salts was used in order to modify the doping degree. The solution was stirred overnight at 60°C. Subsequently, the reaction mixture was dried in air for 24h to complete the crosslinking. At the end, the solid obtained was dried in the oven at 80°C overnight. The as-prepared product was treated in the muffle with the following heating route: 1 step, heating at 5°C/min to reach 600°C; 2 step, isotherm at 600°C for 5 hours.

3.2.4 Rh/Meso-SiO_2 and Rh/Meso-SiO_2@Li

A colloidal Rh solution was prepared by dissolving 0.32 g (1.5 mmol) of $RhCl_3 \cdot 3H_2O$ in 200 mL of distilled H_2O. Then 12,7 mL were taken from the initial solution and diluted to 747 mL of distilled H_2O, to which was added a volume of 1% w/w polymer aqueous solution to obtain the desired Rh:PVA weight ratio. After 3 min, a freshly prepared aqueous solution of $NaBH_4$ (Rh:$NaBH_4$ = 1:5 mol/mol) was added. A gray-brown Rh0 sol was immediately formed. The colloidal solution was stirred for 30 min and, at the end, the Rh colloidal nanoparticles were immobilized by adding the meso-silica (and mesosilica@Li for preparing the Rh/mesosilica@Li) under vigorous stirring. The solution was acidified at pH 2 by using sulfuric acid. To have a nominal metal loading of 1 wt%, the amount of support was calculated. The mixture was stirred overnight at room temperature. Then, the catalyst was centrifuged several times and was washed with hot distilled water to remove ionic species and the polymeric stabilizers, until a neutral pH was reached. After drying overnight at room temperature, the solids were dried at 80°C in an oven for 4 h in static air conditions.

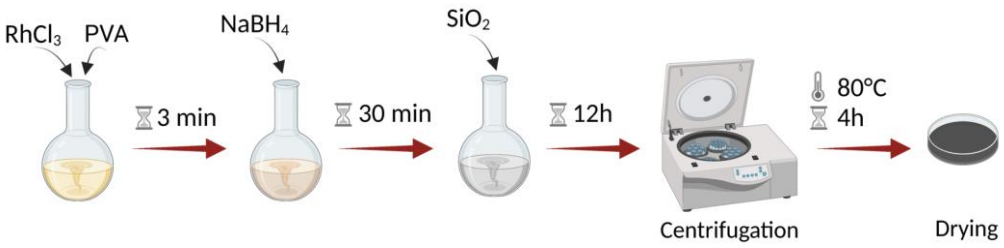

Figure 12. Metal loading.

3.2.5 RhFe/Meso-SiO_2@Li

To prepare 100 ml of Fe stock solution, 0.307 g of Iron(III) nitrate hydrate ($Fe(NO_3)_3 \cdot 7H_2O$, MW = 367.9667 g/mol).

Unfortunately, it was not possible to use the same procedure (sol-immobilization) also for the preparation of the RhFe alloy supported nanoparticles, since Fe tends to easily and rapidly oxidise, thus not allowing to obtain the metallic state. Therefore, an hybrid method was developed combining the sol-immobilization method with the impregnation method. First, Rh/meso-SiO_2 doped with Li was prepared with the

classical sol immobilization mentioned above. After having centrifuged it, let it dry overnight and then put in an oven at 80°C for 4 h in static air conditions, the impregnation was performed to produce the RhFe alloy. The catalyst is dispersed in a solution containing Fe^{3+} at wt 0.5% (so to have 1% metal loading with Rh), which is then put on a plate at 40-50°C and let it be absorbed on the support as the water evaporates.

3.3 – Catalytic activity testing

For the catalytic testing, before loading the catalyst in the reactor tube, it was first pelletized using hydraulic press with a force of 5 kton. The catalyst was then crushed and sieved in order to get a particle distribution between 180 - 300 µm. After, a 100 mg of catalyst was loaded into the reactor tube, with on one side quartz wool and a support rod to hold the catalyst in place (Figure 13).

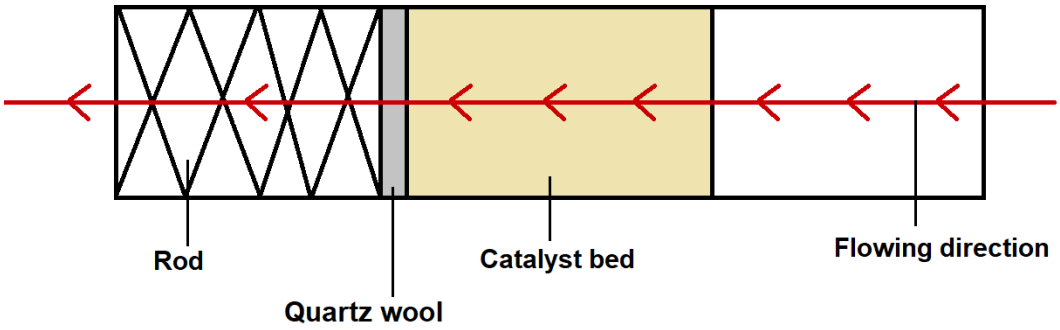

Figure 13. Reactor tube in pressure setup.

The reactor tube with catalyst was placed in the CO_2 hydrogenation setup and tightened. Subsequently, the setup was leak tested at 20 bar. If no leaks were detected the catalyst was reduced under a hydrogen flow of 15.2 mL/min with the reactor temperature set at 200 °C under atmospheric pressure. A high pressure thermal mass flow controller (Bronkhorst, Hi-Tec) was used to control the flow of hydrogen to the reactor system. These conditions are kept for about 1 hour. After that, the reactor is cooled down. Once the reactor has reached room temperature, the pressure of the gas feed line is set to 20 bar and CO_2 flow to 6.4 ml/min, so that a 1/3 CO_2/H_2 ratio is applied. As soon as the flow composition remains constant in time (reaches a steady

state), the hydrogenation reaction can start. Using temperature-programmed control, the reactor tube is kept at 180 °C for 4 hours and then, at 210°C for 3h, 230°C for 3h, 250°C for 3, and at the end 0°C for e[8]h in order to make it cool back to room temperature. Once the reaction is complete, the set pressure is slowly decreased, the H_2 flow is set back to 0 ml/min, the CO_2 valve is closed.
For some tests, the reaction was performed at only one temperature and, in particular, by keeping a constant temperature of 250°C for 6 hours.

A similar procedure was then followed for the testing at 80 bar. The inlet of syringe pump was connected to a high-pressure mixture of CO_2/H_2 line. It is important to make sure to first empty the line. Then, the CO_2/H_2 valve is opened to let the mixture flow, until the desired (80 bar) pressure is reached. After stabilization, the reaction can be started by increasing the temperature activating the temperature-programmed control.

3.4 Formulas

Selectivity, conversion, and STY were calculated using the following formulas:

$$C_{CO_2}(\%) = \frac{\text{moles of } CO_{2(in)} - \text{moles of } CO_{2(out)}}{\text{moles of } CO_{2(in)}} \times 100\,\% \qquad \text{(eq.3)}$$

$$S_{ROH}(\%) = \frac{\text{moles of ROH}}{\text{moles of } CO_{2(in)} - \text{moles of } CO_{2(out)}} \times 100\,\% \qquad \text{(eq.4)}$$

$$S_{CO}(\%) = \frac{\text{moles of CO}}{\text{moles of } CO_{2(in)} - \text{moles of } CO_{2(out)}} \times 100\,\% \qquad \text{(eq.5)}$$

$$S_{CH_4}(\%) = \frac{\text{moles of } CH_4}{\text{moles of } CO_{2(in)} - \text{moles of } CO_{2(out)}} \times 100\,\% \qquad \text{(eq.6)}$$

3.5 Characterization techniques

After the testing, the catalysts were analysed using several characterization techniques, XPS, N_2 adsorption and TEM. The characterization analysis of the products synthesized in this thesis were performed using the instruments present in the Department of Chemical Engineering "Applied Science" of TUDelft University of Technology in Delft, Netherlands.

3.5.1 X-ray photoelectron spectroscopy (XPS)

XPS experiments were conducted using a K-alpha Thermo Fisher Scientific spectrometer equipped with a monochromated Al K-alpha X-ray Source and a Flood Gun to avoid charging of the sample. The electron energy analyzer was operated with a pass energy of 50 eV, and every location was scanned ten times.

X-ray photoelectron spectroscopy (XPS) is a surface characterization technique used to measure the elemental composition and chemical and electronic state (valence state and type of surrounding chemical environment) of atoms within a material. This spectroscopy is based on the photoelectric effect (PE), according to which when a material is hit by photons (Fig. 14), an internal electron of an atom of the material can absorb the entire energy of the incident photon and then be expelled (as photoelectron) with a kinetic energy T proportional to the energy of the incident photon and to the binding energy of the corresponding electron shell (or subshell) of the photon. PE was discovered by Hertz in 1887 and proved mathematically by Einstein in 1905[268] in the equation:

$$KE = h\nu - BE \quad \text{(eq. 7)}$$

where hυ is the energy of the incident photon, BE the binding energy of the electron, referred to the vacuum level and KE the kinetic energy of the ejected electron[269].

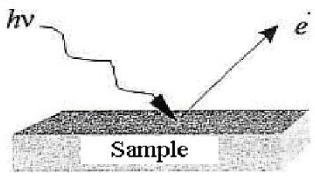

Figure 14. Photoelectric effect.

The probability of this effect is greatest when the energy of the incident photon is equal to or slightly greater than the binding energy of the electron in its shell.

The XPS technique studies the energy spectrum of the electrons emitted from the surface of the sample (in very high vacuum conditions)[270], obtaining a graph of the binding energy as a function of the total electron count. Fig. 15 shows a schematic representation of the XPS process. Since the binding energies of the electrons emitted through the XPS are discrete (quantized) and depend on the nature of the elements, it is possible to associate a particular XPS peak with a chemical species in a unique and well-defined way. Furthermore, for each chemical element, the signal intensity is related to its concentration on the sample surface.

Interestingly, the observed binding energies also depend on the oxidation state and the surrounding chemical environment. A change in these aspects gives rise to small translations in the position of the peak (the so-called "chemical shifts").

According to the Koopmans approximation[271], the ionization energy E0 is equal to the energy of the ejected electron. However, this approximation neglects the fact that the remaining electrons adjust their distributions as ionization occurs and neglects effects due to electron correlation. To take these factors into account, it is possible to insert a correction factor φ (the work function of the spectrometer) and the equation becomes[272]:

$$KE = h\nu - BE - \varphi \quad \text{(eq.8)}$$

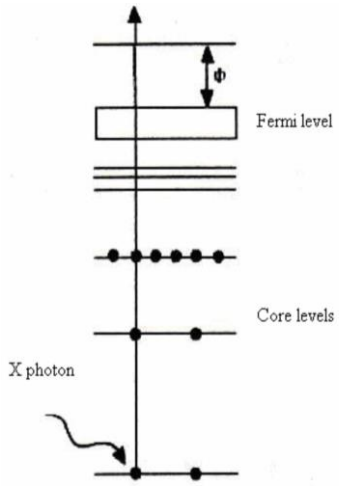

Figure 15. Schematization of the XPS process.

The ejection of an electron from an inner shell creates a hole, representing an electronically excited state, followed by electron shell rearrangement. In particular, this energized state can decay through two distinct relaxation pathways:

- The x-ray emission or X-ray fluorescence (radiative decay), Fig. 16(a), according to which the hole is filled by an electron from an outer shell, which decays by emitting an X-ray photon with equal energy to the difference in binding energy of the two levels involved in the electronic transition.
- The non-radiative Auger decay, Fig. 16(b), according to which the hole is filled by an electron from an outer shell as in the previous case, but the excess energy is transferred to another electron of the outer shell, which it is then emitted (Auger electron) creating a doubly ionized final state.

While the kinetic energy of the Auger electrons depends exclusively on the energies of the levels involved (characteristic of each element and of the valence state) and is therefore independent of the energy of the photons, for that of the XPS electron instead it is the opposite. This aspect allows to distinguish Auger electrons from photoelectrons[273].

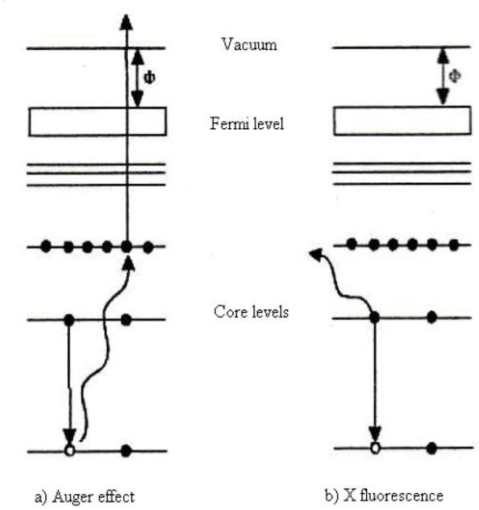

Figure 16. Schematic representation of the Auger effect (a) and X-ray fluorescence (b)

A typical XP spectrum (Figure 17) appears as a graph in which the abscissa axis refers to the BE, expressed in eV, while the intensities of the XP peaks are reported in the

ordinate. Background usually increases with BE due to inelastic photoelectron scattering.

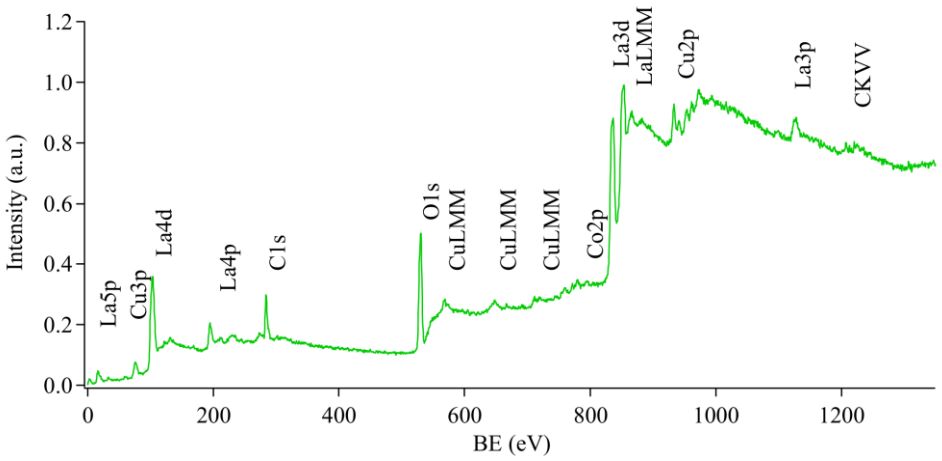

Figure 17. Example of an extended XP Spectrum.

In the spectrum shown in Fig. 17 the bands due to the photoelectrons coming from the core levels (La5p, Cu3p, C1s…) and the peaks due to the Auger effect (CuLMM, CKVV, …) are clearly evident: the so-called "primary structure" of a spectrum. The photoelectronic peaks are indicated with an alphanumeric abbreviation which includes the chemical symbol of the element, followed by the level occupied by the emitted electron.

As far as the Auger electrons are concerned, however, it is customary to mention the levels involved in the decay process. In addition to the "primary structure", it is possible to obtain much more detailed information, that is, to outline the "secondary structure" of a sample, by analyzing the position and shape of the photoelectronic bands. This investigation involves the minor intensity peaks that form as a result of the radiation (satellite peaks - which are observed if the source is not monochromatic - or ghost peaks - which originate from contamination of the source) or signals deriving from multielectronic processes, such as example the shake up, the shake off or the division of multiplets. The shake up and the shake off arise from the interaction of a photoelectron with electrons of the valence band, the splitting of the multiplet occurs when unpaired electrons are present. Measurements can be affected by surface loading effects, for example insulating materials, when bombarded by X-rays, acquire a surface charge. The positive charge causes the emitted electrons to lose an aliquot of

KE which records a BE that is apparently higher than the real one. To overcome this problem, the BE of C1s (285 eV) is used as a reference. In this way, the difference between the position (*i.e.*, the BE) of the measured C1s band and the aforementioned one of 285 eV allows to trace the loading value. Finally, the XPS analysis allows to determine the relative quantities of the elements present on the surface of the investigated sample.

In general, the intensity of the photoelectronic bands depends on various other factors, some of which are specific to the sample (composition, differential cross-section, probability of electron leakage without loss), others due to the characteristics of the instrument (X-ray flux, angle acceptance solidity of the electronic analyzer, investigation efficiency of the instrument), which is why the measurements must be read in relative and not absolute terms[274].

3.5.2 Nitrogen adsorption analysis

The nitrogen adsorption technique measures the amount of gas adsorbed or desorbed from the surface of the material as a function of temperature and partial pressure of the adsorbate. This analysis allowed the study of material parameters, such as the specific surface area (SSA) or BET area, the porous volume, the mean diameter and the distribution of the pores. To carry out the measurement, the sample was ground into a powder, weighed, placed in the sample holder and pre-treated under vacuum at 120°C. Then, nitrogen is adsorbed on the surface of the material under examination at its liquefaction temperature at -196°C using a Quantachrome autosorb degasser and autosorb-6B or a Micromeritics TriStar II 3020. The adsorption portion of the N_2 gas adsorption–desorption isotherms was used to calculate the pore size distribution. The analysis is divided into two parts. First, the sample is placed in an airtight glass burette and is subjected to a degassing for 16 h at 200 °C in order to eliminate any impurities and/or water already adsorbed on the surface of the sample[275]. Secondly, there is the actual analysis in which the burette is placed in a bath of liquid N_2 and gaseous N_2 is

sent for the adsorption/desorption cycle. At the end of the measurement, the data that allow the construction of the isotherm are obtained.

To obtain the value of the specific surface area, the BET model (Brunauer-Emmett-Teller) is used calculated via the multipoint BET method over a linear range of relative pressures between 0.05 and 0.26 using 20 to 21 data points. The BJH model (Barett, Joyner and Halenda) is used to obtain the pore size distribution value based on the physisorption equilibrium isotherms. The data is represented in curves, called nitrogen adsorption isotherms. According to the IUPAC classification (Figure 18), there are six types of absorption isotherms[20]. Materials with mainly narrow micropores (such as such as zeolites and some types of activated carbon) display type I or Langmuir isotherm, where the pores fill at very low relative pressure with a steep uptake, because of considerable adsorbent-adsorbate interactions[21]. The transition point from monolayer coverage to multilayer begins at point B in Figure 18. Nonporous and macropores materials mainly yield isotherms of type II (reversible isotherms), where N_2 molecules are absorbed in mono/multi-layers without restriction. Type IV isotherm is characteristic of micro- and mesoporous solids, and therefore also typical of the substrates studied in this thesis work. Initially, the curve follows the same profile as the type II isotherm. Then, by further increasing the pressure, the interactions between gas molecules and adsorbent mesopore surface lead to a rapid vertical stretch due to the capillary condensation (*i.e.*, the gas adsorbed inside the mesopores is no longer stable in the vapor and condensate). The initial zero slope of types III and V at low relative pressure reflects weak adsorbate-adsorbent interactions, comparable to the adsorbate-adsorbate interactions. This type of isotherms does not allow the estimation of the solids monolayer capacity and thus SSA. Type VI corresponds to stepwise multilayer adsorption on a uniform non-porous surface[22].

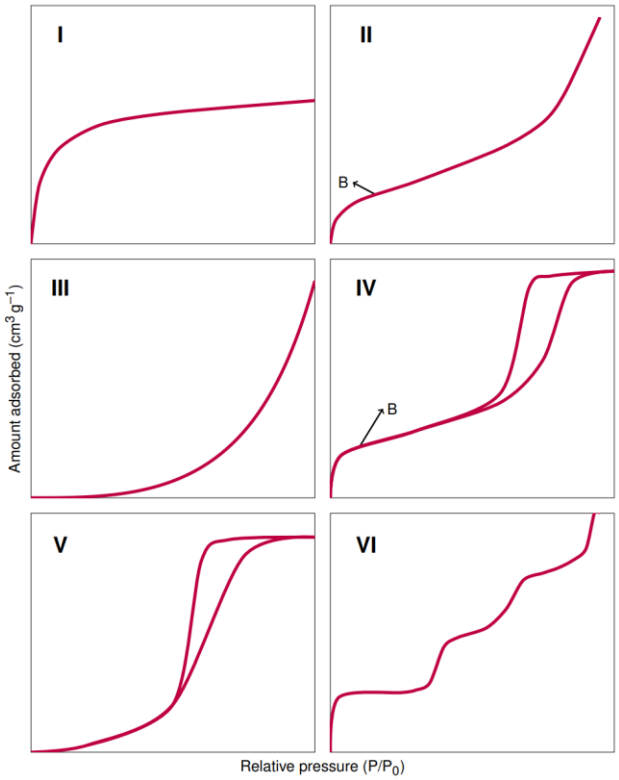

Figure 18. The IUPAC classification of adsorption isotherms showing both the adsorption and desorption pathways. Note the hysteresis in types IV and V[23].

Often, in the type IV isotherm, typical of mesoporous adsorbents, the presence of an hysteresis loop is observed. This is because the desorption curve does not correspond to the adsorption one. In presence of hysteresis, IUPAC further classifies porous materials according to the shape that the hysteresis loop takes (Figure 19). According to IUPAC, type H1 is often associated with porous materials with well-defined cylindrical pores. In contrast, the H2 type is attributed to materials with a disordered pore size and shape distribution. Materials giving rise to hysteresis with the form H3, in which there is no adsorption limit at high P/P_0 values, have slit-shaped pores due to aggregates of particles arranged in thin layers. Finally, H4-type hysteresis is often associated with materials containing both micropores and mesopores[22].

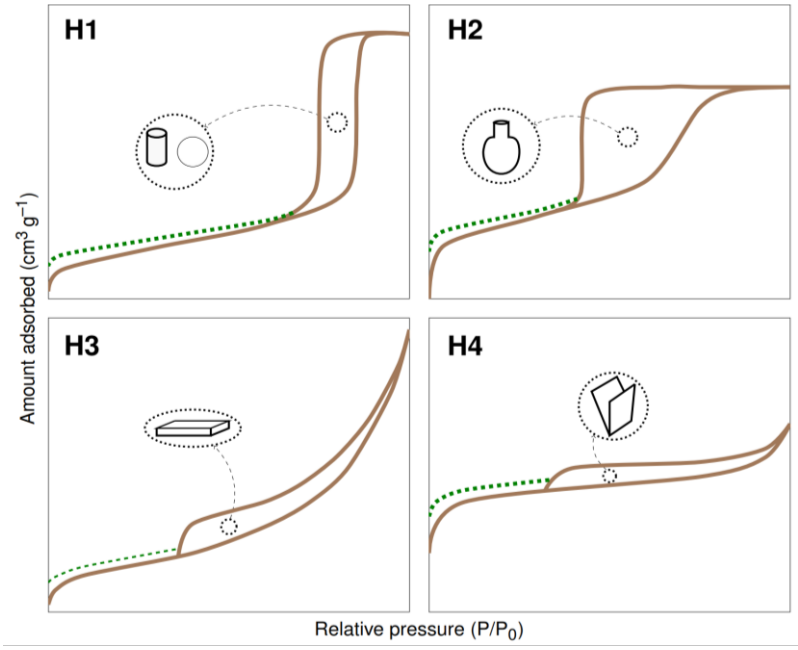

Figure 19. The relationship between pore shape and the adsorption-desorption isotherm[23]

3.5.3 Transmission electron microscopy (TEM)

Transmission electron microscopy (TEM) is a technique by which an electron beam is transmitted through a very thin sample (5 to 500 nm) and two-dimensional images of nanoparticles are generated, from which is possible to determine particle size by hand from the images using ImageJ software. For the observation of the sample, a FEI Tecnai F20 electron microscope was used, equipped with a FEG and operated at 200 kV. It is necessary to create a vacuum inside the microscope (P = $10^{-4}/10^{-5}$ mbar) to reduce the interaction between electrons and gas molecules. The image provided by an electron microscope is formed in a cathode ray tube synchronized with a beam of charged particles, mainly electrons, which scan the surface of the object. The electrons are generated by a source, generally made up of a tungsten filament, which emits charged particles by the thermionic effect; these are then accelerated by a potential difference varying between 0.3 and 30 KV. After, a system of electromagnetic lenses provides a reduced image of the source in the sample plane. The electrons pass into the scanning system where they are deflected by magnetic fields which scan the surface of the sample. The electron beam that strikes the sample has a synchronized movement with the beam that excites the fluorescent elements of the screen, thus allowing the image to be displayed.

4 Results and discussion

In this chapter, the obtained results from the tested catalysts are shown and discussed. The material is then characterized using TEM, XPS and BET techniques.

4.1 Catalytic activity testing

CO_2 hydrogenation to ethanol follows these reaction steps:

$$(12)\ CO_2 + 6H_2 \rightleftharpoons C_2H_5OH_{(g)} + 3H_2O_{(g)} \qquad \Delta H = -173.7\ kJ/mol$$

$$(13)\ 2CO + 6H_2 \rightleftharpoons C_2H_2OH_{(g)} + H_2O_{(g)} \qquad \Delta H = -255.9\ kJ/mol$$

$$(14)\ CO + H_2O_{(g)} \rightleftharpoons H_2 + CO_2 \qquad \Delta H = -41.1\ kJ/mol\ (3)$$

Eqs. (12) and (13) are both exothermic and thermodynamically controlled. Therefore, the literature reports that the CO_2 hydrogenation to ethanol should be performed at a low temperature (around 200°C) to have a good conversion and selectivity[1]. During the process, a water gas shift (WGS) reaction also occurs (14), which is essential in affecting the equilibrium of CO and CO_2 hydrogenation reactions. The RWGS reaction (reverse of 14) can also occur, which partially reduces the CO_2 into CO and is the source for ethanol synthesis.
Moreover, the product carbon oxides methanation reaction can also occur[2,3]:

$$(15)\ CO + 3H_2 \rightleftharpoons CH_4 + H_2O \qquad \Delta H_{298K} = -206.2\ kJ\ mol^{-1}$$

$$(6)\ CO_2 + 4H_2 \rightarrow CH_4 + 2H_2O \qquad \Delta H_{298K} = -164.63\ kJ/mol$$

For the catalyst screening, the same catalyst was first tested at different Rh loading (0.25wt%, 0.5wt%, and 1wt%); then, at different Li quantities (0.5wt% and 1wt%) keeping the same wt%Rh (1wt%). The same reaction was performed at 20 bar and varying the temperature from 180 °C to 250°C and under 10 ml/min of CO_2/H_2 flow with a molar ratio of 1/3. After, the reaction was performed keeping a constant loading of Li (10wt%), but varying the one of Rh (1wt% and 3wt%), and then keeping a constant Li and Rh loadings (10wt% and 1wt%, respectively), but adding a second

metal (Fe) at 1wt%. In this case, the pressure was kept at 20 bar, but at a constant temperature of 250°C for 6h, always under 10 ml/min of CO_2/H_2 flow with a molar ratio of 1/3. The 1wt%Rh/meso-SiO_2@Li10% and the 1wt%RhFe/meso-SiO_2@Li10% catalysts were tested also at 80 bar and at 250°C, under 10 ml/min of CO_2/H_2 flow with a molar ratio of 1/3.

4.1.1 Rh/meso-SiO_2

The first results of the catalytic activity testing for Rh/meso-SiO_2 at different Rh loading are displayed in Figures 20-22.

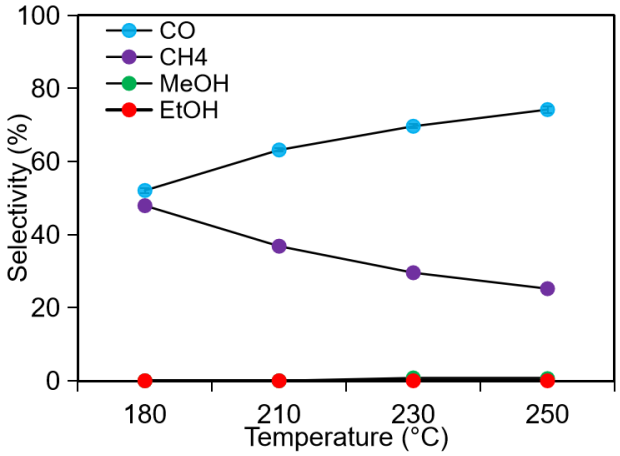

Figure 20. Results of catalytic testing of a 100mg of 0.25wt% Rh/meso-SiO_2 under a flow of 20 mL/min of CO_2/H_2 with a molar ratio of 1/3 at 20 bar.

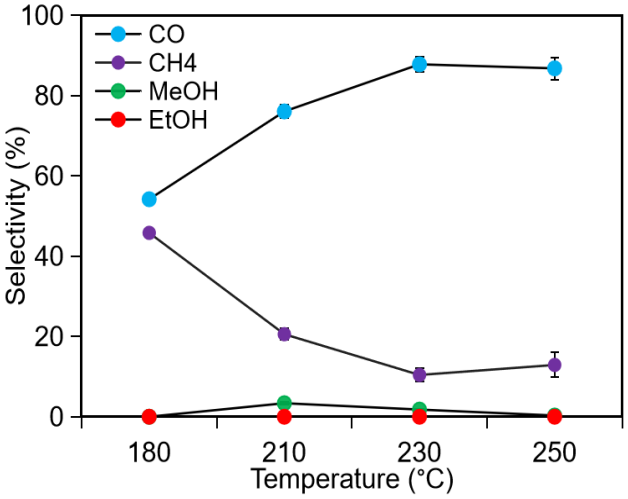

Figure 21. Results of catalytic testing of a 100mg of 0.5wt% Rh/meso-SiO_2 under a flow of 20 mL/min of CO_2/H_2 with a molar ratio of 1/3 at 20 bar.

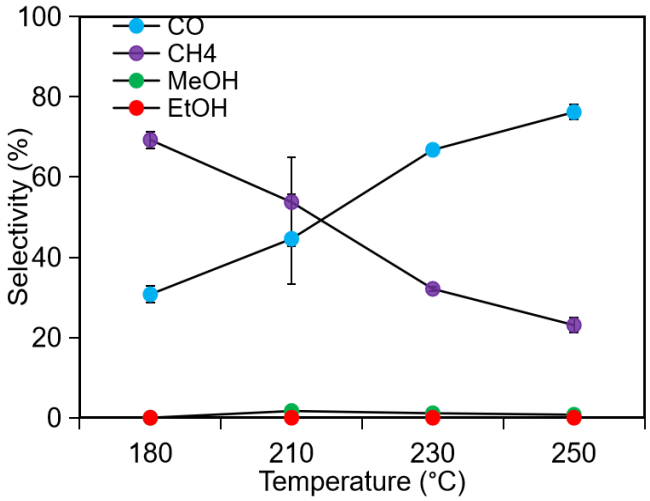

Figure 22. Results of catalytic testing of a 100mg of 1wt% Rh/meso-SiO_2 under a flow of 20 mL/min of CO_2/H_2 with a molar ratio of 1/3 at 20 bar.

Theoretically, as the temperature increases, as CO_2 conversion should increase, the selectivity of methanol should decrease since the reaction competes with the RWGS reaction. However, in practice, during catalytic testing, this doesn't always happens. Indeed, in the above graphs (Figure 20-22), this trend is not perfectly respected, which does not mean that there is any problem with the reaction or the data analysis, also because the variations of methanol selectivity with the temperature are negligible (only about 1-2%). In all three graphs (Figure 20-22), a slight increase of methanol selectivity was observed when the temperature reached 210°C and then decreased again around 250°C (see Table 2 below).

The most important information that can be gleaned from these results is that as the Rh concentration increases, the methane concentration increases, which means that the methanation activity is highly favoured, especially at Rh1 wt%. On the other hand, this could also justify the decrease of CO selectivity with increasing Rh burden. Indeed, one explanation could be that the increase in active phase (Rh) could have likely led to the CO produced being further transformed into methane

For lower Rh concentrations (0.25 wt% Rh), CO concentration is much higher, which means that the RWGS reaction is more active. With 0.5 wt% Rh, however, there is a balance between RWGS and methanation.

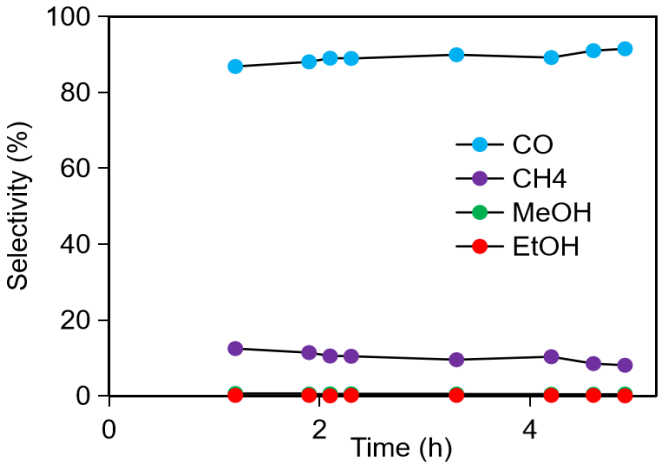

Figure 23. Results of catalytic testing of a 100mg of 0.25wt% Rh/meso-SiO_2 under a flow of 20 mL/min of CO_2/H_2 with a molar ratio of 1/3 at 20 bar.

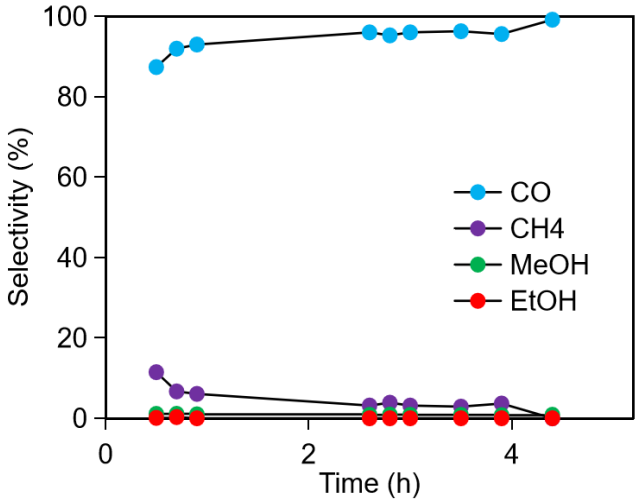

Figure 24. Results of catalytic testing of a 100mg of 0.5wt% Rh/meso-SiO_2 under a flow of 20 mL/min of CO_2/H_2 with a molar ratio of 1/3 at 20 bar.

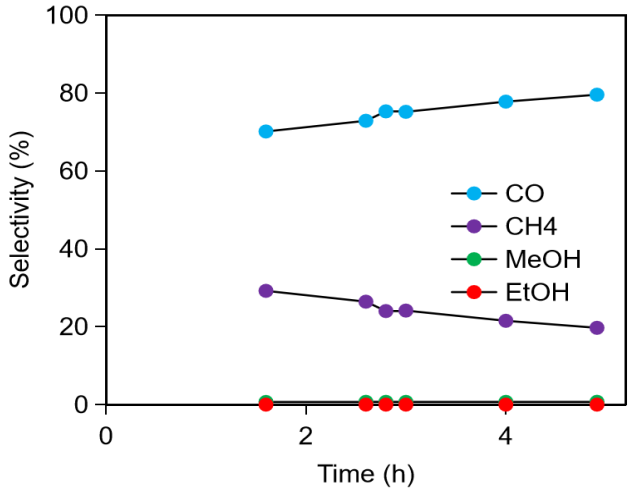

Figure 25. Results of catalytic testing of a 100mg of 1wt% Rh/meso-SiO_2 under a flow of 20 mL/min of CO_2/H_2 with a molar ratio of 1/3 at 20 bar.

Figure 23-25 show the test performed using same catalysts but maintaining the same reaction temperature (250°C) in order to check catalyst stability and spot any possible deactivation effect. However, the same trend was observed: as Rh loading increases, methane concentration increases, while CO concentration decreases. Overall, Figures 23-25 showed a constant trend, proving the stability of the catalyst during the reaction.

As for the ethanol, unfortunately, it was not detected in the products mixture, meaning the unpromoted catalyst is non-selective for ethanol production.

As regards the conversion (Figure 26), although it was low for all three samples, it maintained an almost constant value during all the reactions.

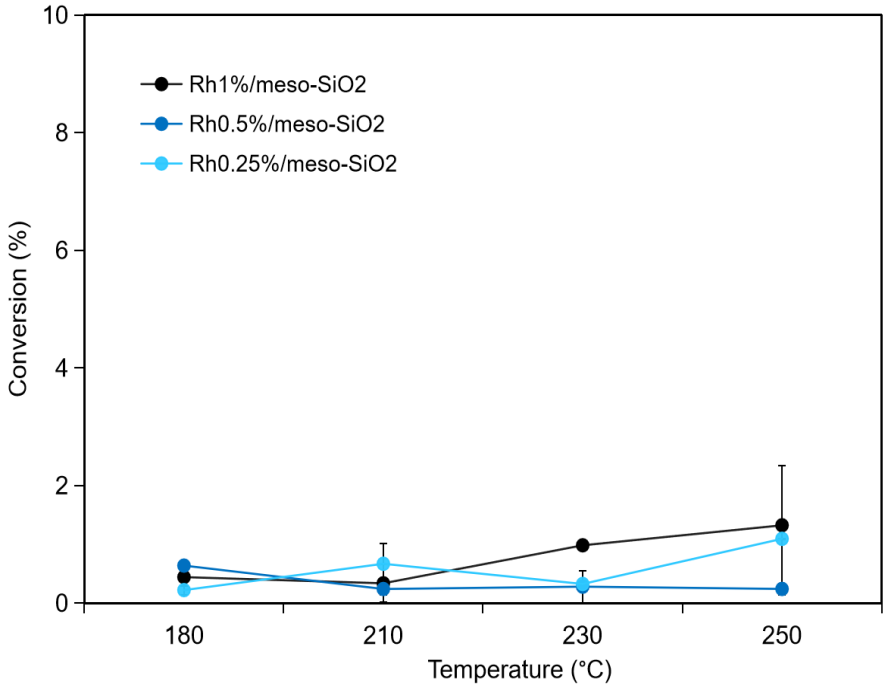

Figure 26. Results of catalytic testing of a 100mg of 0.25wt% Rh/meso-SiO_2, 0.5wt% Rh/meso-SiO_2 and 1wt% Rh/meso-SiO_2 under a flow of 20 mL/min of CO_2/H_2 with a molar ratio of 1/3 at 20 bar.

All the results are summarized in the table below (Table 2).

Rh (%)	T (°C)	p (bar)	Selectivity (%)				C balance (%)	CO_2 conversion (%)
			CO	CH_4	MeOH	EtOH		
0.25	180	20	52.1	47.9	0.0	0.0	99.8	0.2
	210	20	63.2	36.8	0.0	0.0	99.5	0.7
	230	20	69.7	29.6	0.8	0.0	99.9	0.3
	250	20	74.2	25.2	0.6	0.0	99.4	1.1
0.5	180	20	54.2	45.8	0.0	0.0	99.4	0.6
	210	20	76.1	20.6	3.4	0.0	99.9	0.2
	230	20	87.8	10.4	1.8	0.0	99.9	0.3
	250	20	86.8	12.9	0.3	0.0	100.0	0.2
1	180	20	30.8	69.2	0.0	0.0	99.6	0.4
	210	20	44.6	53.7	1.7	0.0	99.8	0.3
	230	20	66.8	32.1	1.1	0.0	99.3	1.0
	250	20	76.2	23.1	0.7	0.0	99.3	1.3

Table 2. Summary of catalytic results obtained for Rh/meso-SiO_2 with increasing metal loading (0.25%, 0.5%, and 1%) tested from 180°C to 250°C of CO_2/H_2 with a molar ratio of 1/3 at 20 bar..

4.1.2 Rh1%/meso-SiO_2@Li0.5% and Li1%

In an effort to try to improve the selectivity of ethanol, the catalyst was doped with the addition of Li. Alkali promoters are required to shift the catalyst selectivity toward C^{2+} oxygenates in CO_2 hydrogenation[4]. To find the lower limit at which the catalytic activity would start to show better results, Li was first added in a very low amount (0.5%). After that, its amount was doubled to 1%. As can be seen from figures 27 and 28 below, going from Li0.5% to Li1%, there was an actual increase in both the methanol and ethanol selectivity, going from 0.4% to 1.7% and from 0 to 0.6% respectively. Methane and CO instead maintained a more or less constant value, showing selectivities of approximately 20% and 80% respectively (Table 3).

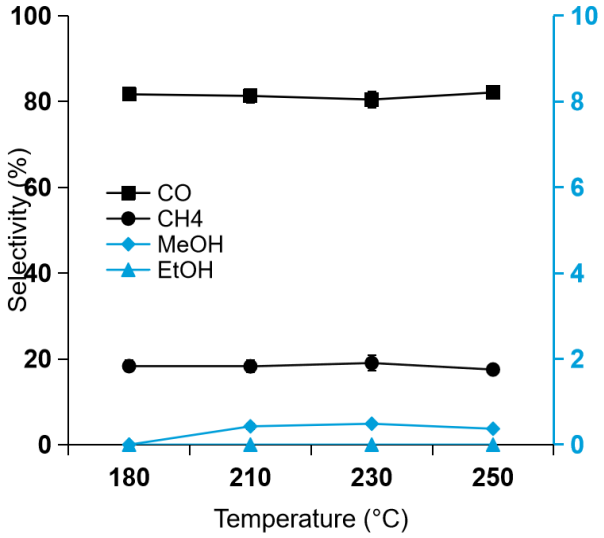

Figure 27. Results of catalytic testing of a 100mg of 1wt% Rh/meso-SiO_2 with 0.5%Li under a flow of 20 mL/min of CO_2/H_2 with a molar ratio of 1/3 at 20 bar.

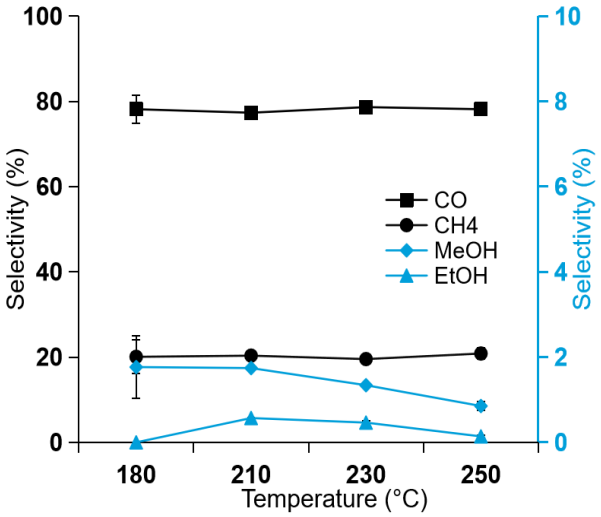

Figure 28. Results of catalytic testing of a 100mg of 1wt% Rh/meso-SiO_2 with 1%Li under a flow of 20 mL/min of CO_2/H_2 with a molar ratio of 1/3 at 20 bar.

As for the conversion (Figure 29), it remained almost constant between the two catalysts, with a slight increase from 180°C and 210°C using the catalyst doped with Li1% (see Table 3).

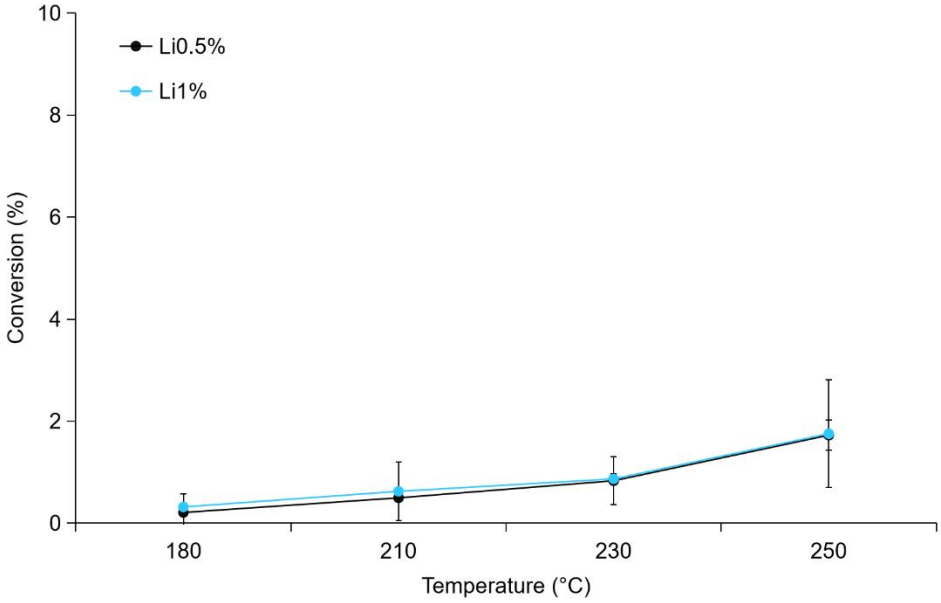

Figure 29. Results of catalytic testing of a 100mg of 1wt% Rh/meso-SiO_2 with 1%Li under a flow of 20 mL/min of CO_2/H_2 with a molar ratio of 1/3 at 20 bar.

Also this time, the results are summarized in the following table:

Li (%)	T (°C)	p (bar)	Selectivity (%)				C Balance (%)	CO_2 conversion (%)
			CO	CH_4	MeOH	EtOH		
0.5	180	20	81.7	18.3	0.0	0.0	99.9	0.2
	210	20	81.3	18.3	0.4	0.0	99.8	0.5
	230	20	80.5	19.0	0.5	0.0	99.7	0.8
	250	20	82.1	17.5	0.4	0.0	99.4	1.7
1	180	20	78.2	20.1	1.8	0.0	99.9	0.3
	210	20	77.3	20.4	1.7	0.6	99.9	0.6
	230	20	78.7	19.5	1.3	0.5	100.0	0.9
	250	20	78.2	20.9	0.9	0.1	99.9	1.8

Table 3. Summary of catalytic results obtained for 1 wt% Rh/meso-SiO_2 with increasing Li loading (0.5% and 1%) tested from 180°C to 250°C under a flow of 20 mL/min of CO_2/H_2 with a molar ratio of 1/3 at 20 bar.

4.1.3 Rh1%/meso-SiO_2@Li10%

By increasing the amount of promoter (Li10%), there was a great increase in CO_2 conversion, passing from 1.8% to 14.2% at 250°C (Figure 32), while for methanol and ethanol selectivity there is no significant change. Moreover, by increasing the active phase (using 3wt%Rh) while keeping the same quantity of Li promoter (Li10%), there is actually a slight decrease in methanol and ethanol selectivity (Figure 31), but a huge decrease in CO_2 conversion (Figure 32), which passed from 14.2% with 1wt%Rh to 2.1% with 3wt%Rh.

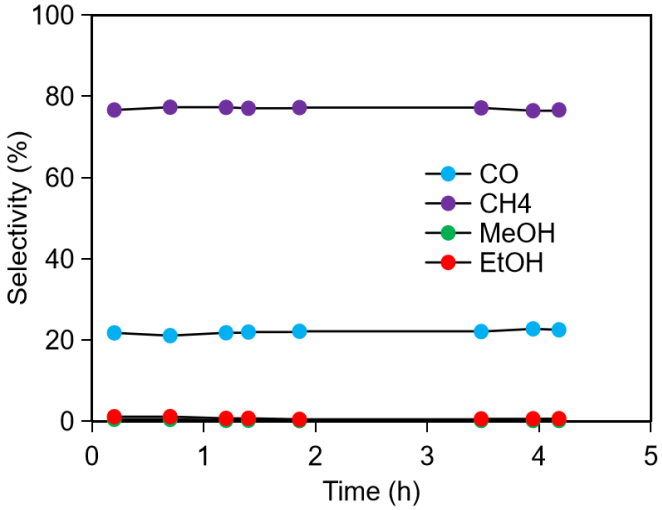

Figure 30. Results of catalytic testing of a 100mg of 1wt% Rh/meso-SiO_2 with 10%Li under a flow of 20 mL/min of CO_2/H_2 with a molar ratio of 1/3 at 20 bar.

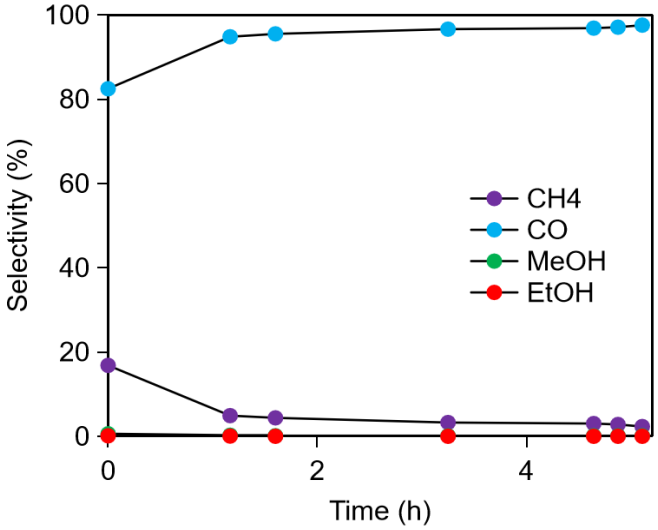

Figure 31. Results of catalytic testing of a 100mg of 3wt% Rh/meso-SiO_2 with 10%Li under a flow of 20 mL/min of CO_2/H_2 with a molar ratio of 1/3 at 20 bar.

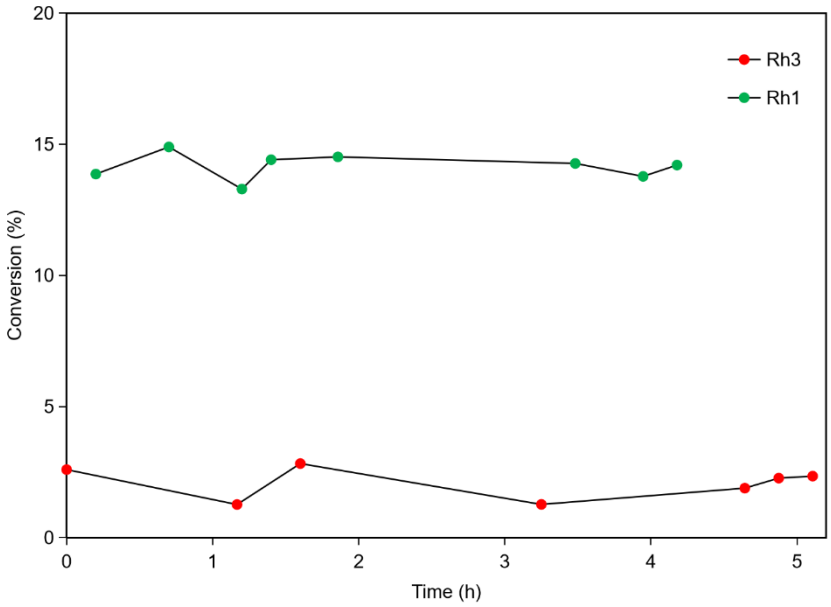

Figure 32. Results of catalytic testing of a 100mg of 1wt% and 3wt% Rh/meso-SiO_2 with 10%Li under a flow of 20 mL/min of CO_2/H_2 with a molar ratio of 1/3 at 20 bar.

4.1.4 Rh1%/meso-SiO_2@Li10% – 80 bar

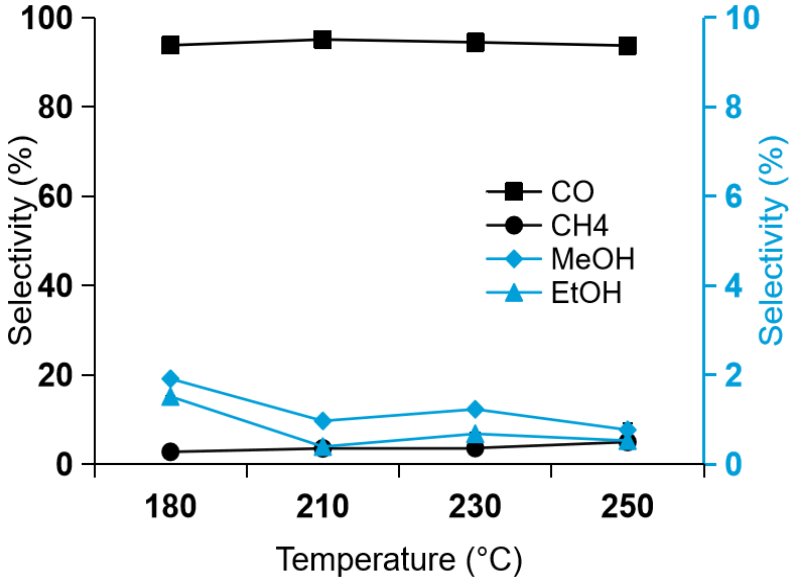

Figure 33. Results of catalytic testing of a 100mg of 1% Rh/meso-SiO_2 with 10%Li under a flow of 20 mL/min of CO_2/H_2 with a molar ratio of 1/3 at 80 bar.

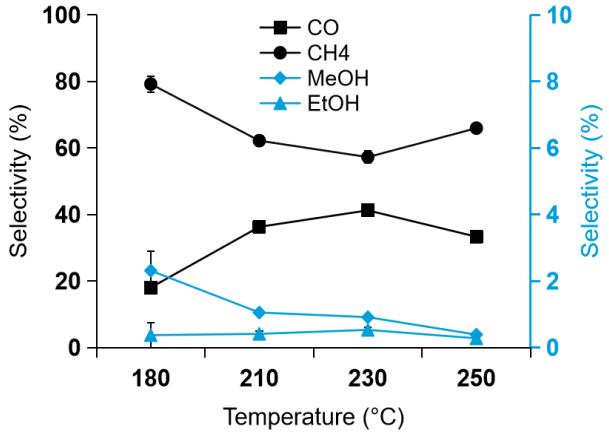

Figure 34. Results of catalytic testing of a 100mg of 3% Rh/mesosilica with 10%Li under a flow of 20 mL/min of CO_2/H_2 with a molar ratio of 1/3 at 80 bar.

As just discussed above, no improvement has been recorded for Rh/meso-SiO_2 doped with Li10% by increasing the active phase from 1wt% to 3 wt% (Figure 30 and 31) and the best results in terms of CO_2 conversion were actually obtained with the one with lower Rh loading. However, both catalysts (1wt%Rh/meso-SiO_2@Li10% and 3wt%Rh/meso-SiO_2@Li10%) were tested also at 80 bar (Figure 33 and 34). CO_2 conversion increases with increasing pressure because thermodynamically, ethanol formation is favored at high pressure[5]. As shown in the table below, surprisingly, compared to the 20 bar test, CO_2 conversion remained steady for 1wt%Rh/meso-SiO_2@Li10% at 80 bar, while quadruplicate in case of 3wt%Rh/meso-SiO_2@Li10% passing from 2.1% to 10.7%. An opposite trend was recorded for methane and CO selectivities. By increasing the pressure from 20 bar to 80 bar, while for 1wt%Rh, methane significantly decreased (from 76.8% to 5%) and CO increased (from 22.1% to 93.8%), for 3wt%Rh it was the opposite: methane had a distinct increase (from 5.4% to 66%) and CO decreased (from 94.4% to 33.3%).

The results obtained are summarized in the following table:

Rh (%)	T (°C)	P (bar)	Selectivity (%)				C Balance (%)	CO_2 conversion (%)
			CO	CH_4	MeOH	EtOH		
1	250	20	22.1	76.8	0.3	0.8	99.9	14.1
	250	80	93.8	5.0	0.7	0.5	100.0	14.1
3	250	20	94.4	5.4	0.2	0.0	99.9	2.1
	250	80	33.3	66.0	0.4	0.3	100.4	10.7

Table 4. Summary of catalytic results obtained for 1 wt% and 3 wt% Rh/meso-SiO2 with 10% Li tested from 180°C to 250°C at 20 and 80 bar flow of 20 mL/min of CO_2/H_2 with a molar ratio of 1/3.

4.1.5 1wt% RhFe/meso-SiO_2@Li10% – 20 bar vs 80 bar

At this point, a bimetallic catalyst was synthesized by adding Fe to the Rh-supported catalysts using first the sol immobilization method and then the IWI method. This was done since transition metals, especially Fe, has showed to shift the catalyst selectivity toward C^{2+} oxygenates in CO_2 hydrogenation[4]. Compared to the monometallic catalyst (1wt% Rh/meso-SiO_2 with 10wt% Li) showed in Figure 30, for the bimetallic catalyst (Figure 35) a slight increase in both methanol and ethanol selectivity, as well as in CO_2 conversion (5%) were recorded.

By testing the same catalyst at 80 bar (Figure 37), a significant increase in methanol selectivity was recorded especially at 180°C (19.5%). Then, it slowly decreased as the temperature increased until reaching 5.8% at 250°C. This might be due to deactivation effects due to the sintering of the particles at high temperatures. It can also be due to the RWGS reaction with which it competes at higher temperatures. However, compared to the catalyst tested at lower pressures (Figure 35), there is an increase in methanol selectivity at 250°C, passing from 1.3% at 20 bar to 5.8% at 80 bar, and only a slight increase for ethanol selectivity and CO_2 conversion, respectively, passing from 0.2% at 20 bar to 0.9% at 80 bar, and from 5.0% at 20 bar to 6.8 at 80 bar. The changes are not very relevant, if compared with those reported in the literature.

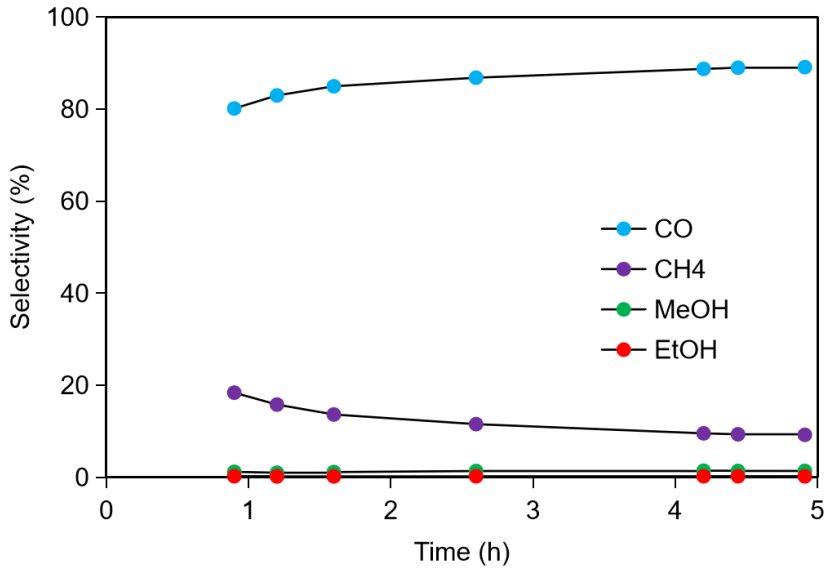

Figure 35. Results of catalytic testing of a 100mg of 1wt% RhFemeso-SiO_2 with 10%Li under a flow of 20 mL/min of CO_2/H_2 with a molar ratio of 1/3 at 20 bar.

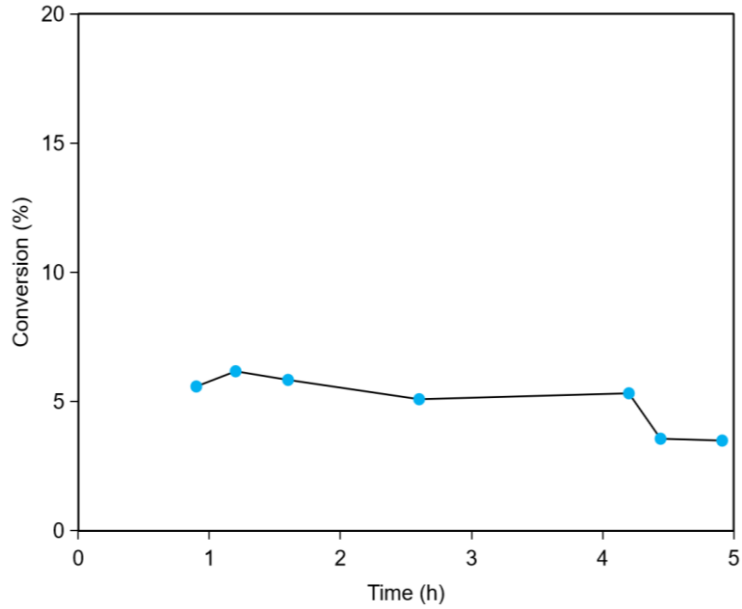

Figure 36. Results of catalytic testing of a 100mg of 1% RhFe/meso-SiO_2 with 10%Li under a flow of 20 mL/min of CO_2/H_2 with a molar ratio of 1/3 at 20 bar.

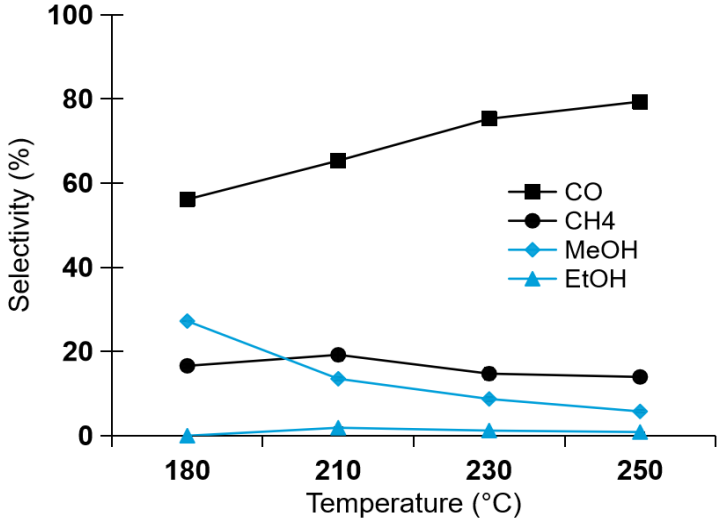

Figure 37. Results of catalytic testing of a 100mg of 1% RhFe/meso-SiO_2 with 10%Li under a flow of 20 mL/min of CO_2/H_2 with a molar ratio of 1/3 at 80 bar.

The figure below (Figure 38) summarizes all the CO_2 conversions obtained from testing the catalysts at 80 bar, increasing temperature from 180°C to 250°C. It is clear that 1 wt% Rh on mesosilica with 10 wt% Li is the best catalyst, with 14.1% of CO_2 conversion at 250°C, compared to 3% obtained with 1 wt% Rh on mesosilica with 1 wt% Li. This underlines the importance of adding the alkali promotor Li to enhance the catalytic activity, even though still great improvements are needed since the results were not satisfactory.

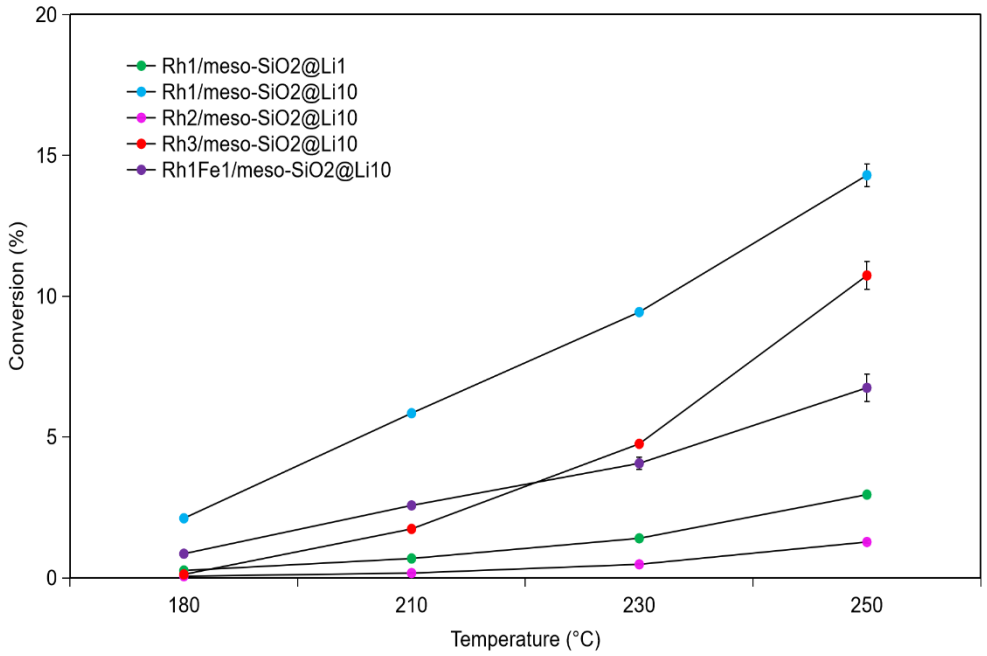

Figure 38. Results of catalytic testing of a 100mg of 1% RhFe/*meso-SiO₂* with 10%Li under a flow of 20 mL/min of CO_2/H_2 with a *molar* ratio of 1/3 at 80 bar.

	T (°C)	p (bar)	Selectivity (%)				C Balance (%)	CO_2 conversion (%)
			CO	CH_4	MeOH	EtOH		
Rh1/meso-SiO2@Li1	180	80	91.5	8.4	0.2	0.0	100.0	0.3
	210	80	89.0	10.6	0.4	0.0	100.1	0.7
	230	80	89.1	10.0	0.7	0.2	100.1	1.4
	250	80	90.2	9.0	0.6	0.2	100.1	3.0
Rh1/meso-SiO2@Li10	180	80	93.8	2.8	1.9	1.5	100.0	2.1
	210	80	95.1	3.5	1.0	0.4	100.0	5.9
	230	80	94.5	3.6	1.2	0.7	100.0	9.4
	250	80	93.7	5.0	0.8	0.5	100.0	14.3
Rh3/meso-SiO2@Li10	180	80	18.1	79.3	2.3	0.4	100.7	0.1
	210	80	36.3	62.2	1.1	0.4	101.0	1.7
	230	80	41.3	57.3	0.9	0.5	101.0	4.8
	250	80	33.3	66.0	0.4	0.3	100.4	10.7
Rh1Fe1/meso-SiO2@Li10	180	80	59.1	21.0	19.5	0.4	100.0	0.7
	210	80	65.0	19.5	13.7	1.9	100.0	2.5
	230	80	75.0	14.0	9.6	1.4	100.0	3.8
	250	80	79.4	14.0	5.8	0.9	99.9	6.8

Table 5. Summary of catalytic results obtained for Rh/meso-SiO₂ with 1% Li, 1 wt% and 3 wt% Rh/meso-SiO2 with 10% Li, and 1wt% RhFe/meso-SiO₂ with 10% Li tested from 180°C to 250°C at 80 bar under a 20ml/min of CO_2/H_2 with a molar ratio of 1/3.

The table above (Table 5) summarizes all the results obtained for the catalysts tested at 80 bar. While, 1 wt% Rh on mesosilica doped with 10 wt% Li was the best one in terms of CO_2 conversion, the bimetallic catalyst 1 wt% RhFe on mesosilica doped with 10 wt% Li was the best one in terms of methanol and ethanol selectivity. However, by increasing the temperature, while CO_2 conversion increased, methanol selectivity decreased from 19.5% at 180°C to 5.8% at 250°C. Deviations might originate from a slight particle size dependence of the specific activity, and/or a change in the effectiveness of Li promoter species following Rh particle growth.

4.1.6 Rh/SiO_2 – 20 bar

The disappointing results might be due to two things: either a problem with the reaction conditions since the reaction is favoured at higher pressures or it might imply a problem with the material itself. This is why the same reaction, at the same temperature and pressure conditions, was run using a catalyst with the same amount of active phase, but changing the support. In particular, it was used commercial silica, which is also the one that has been adopted by the previous students in the research group. However, instead of using the impregnation method that was chosen by the previous students, the same method using for synthesising the other catalysts in this study was chosen: the sol-immobilization method.

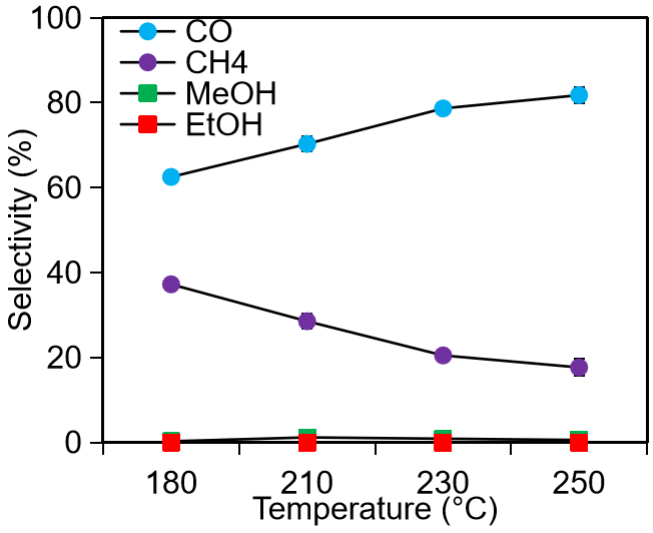

Figure 39. Results of catalytic testing of a 100mg of 0.25% Rh/SiO_2 under a flow of 20 mL/min of CO_2/H_2 with a molar ratio of 1/3 at 20 bar.

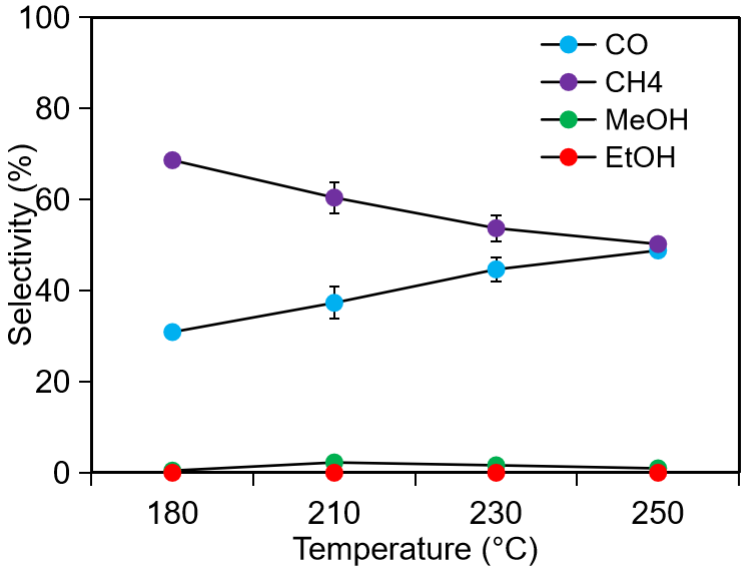

Figure 40. Results of catalytic testing of a 100mg of 0.5% Rh/SiO_2 under a flow of 20 mL/min of CO_2/H_2 with a molar ratio of 1/3 at 20 bar.

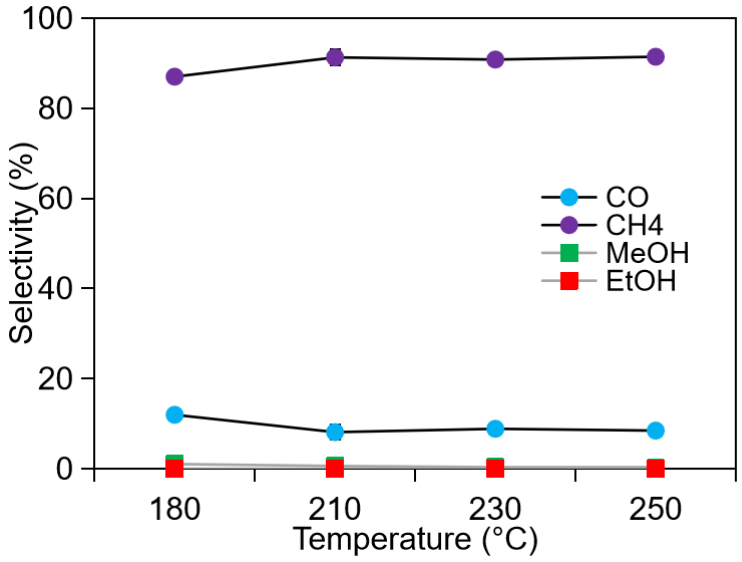

Figure 41. Results of catalytic testing of a 100mg of 1% Rh/SiO_2 under a flow of 20 mL/min of CO_2/H_2 with a molar ratio of 1/3 at 20 bar.

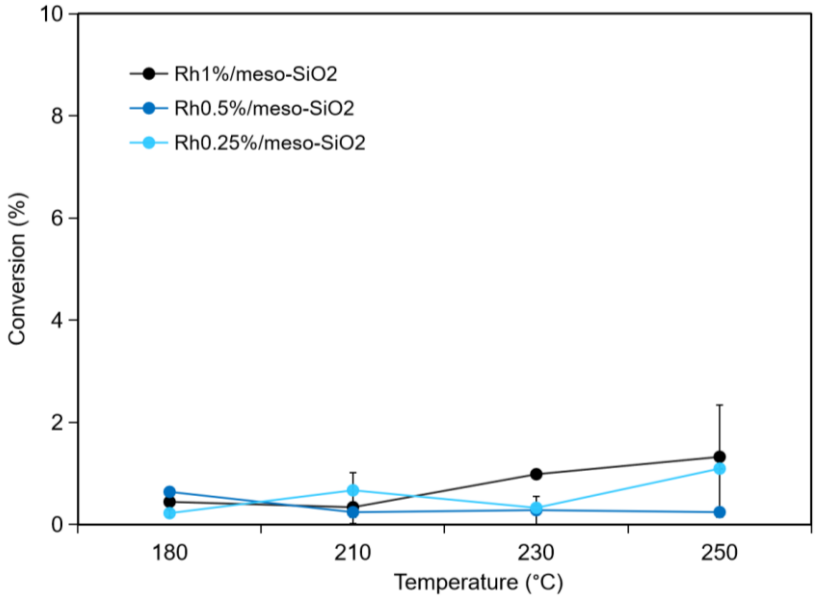

Figure 42. Results of catalytic testing of a 100mg of 0.25%, 0.5%, and 1% Rh/SiO_2 under a flow of 20 mL/min of CO_2/H_2 with a molar ratio of 1/3 at 20 bar.

Compared to Figure 20-22 showing the results obtained for Rh/mesosilica with increasing concentrations of active phase (0.25%, 0.5% and 1%), also in case of Rh/SiO_2 (Figure 39-41), as the temperature increase, methane concentration decreases while CO concentration increases. This shows that at higher temperatures, RWGS is favoured. However, increasing the active phase, while for the Rh supported on mesosilica the trend remained almost constant among the three catalysts, with Rh supported on commercial silica there is a net decrease in CO concentration and a net increase in methane concentration passing from 0.25 wt% Rh to 1 wt% Rh. This is true, except for the last plot with 1 wt% Rh/SiO_2, where both methane and CO remain almost constant throughout all the temperature, meaning that there might be an issue with the methane and CO detection.

Unfortunately, also in this case no ethanol was detected. However, CO_2 conversion (Figure 39), also in this case it increased as the temperature was increased and this time also as the active phase was increased. As for methanol selectivity, it peaked at 210°C, except again for 1 wt% Rh/SiO2, where it is higher at 180°C and then decreases as the temperature increased. This means that this experiment might give wrong information, so it is not possible to be critical on this test. It might be necessary to run the reaction again and check the results.

The following table summarizes all the results obtained for Rh/SiO_2:

Rh (%)	T (°C)	p (bar)	Selectivity (%)				C balance (%)	CO_2 conversion (%)
			CO	CH_4	MeOH	EtOH		
0.25	180	20	62.5	37.2	0.3	0.0	99.8	0.3
	210	20	70.3	28.5	1.2	0.0	99.7	0.6
	230	20	78.6	20.5	0.9	0.0	99.9	0.7
	250	20	81.8	17.7	0.6	0.0	99.8	1.3
0.5	180	20	30.9	68.6	0.5	0.0	100.0	0.2
	210	20	37.3	60.4	2.3	0.0	99.6	1.0
	230	20	44.7	53.7	1.6	0.0	99.9	1.2
	250	20	48.8	50.2	1.0	0.0	99.9	2.4
1	180	20	12.0	87.0	1.0	0.0	99.8	0.6
	210	20	8.1	91.3	0.6	0.0	99.9	1.2
	230	20	8.9	90.8	0.3	0.0	99.1	3.4
	250	20	8.5	91.4	0.1	0.0	99.8	5.7

Table 6. Summary of catalytic results obtained for Rh/SiO2 with increasing concentrations of metal loading (0.25%, 0.5%. and 1%) tested from 180°C to 250°C at 20 bar under a 20ml/min CO_2/H_2 with a molar ratio of 1/3 at 20 bar.

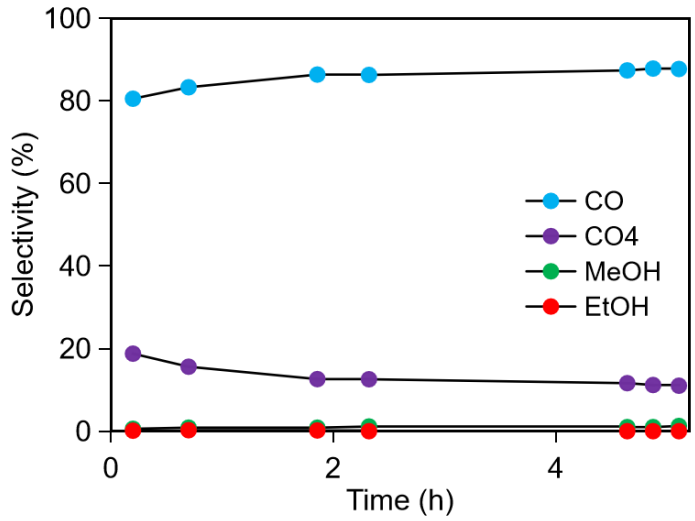

Figure 43. Results of catalytic testing of a 100mg of 0.25 wt% Rh/SiO_2 under a flow of 20 mL/min of CO_2/H_2 with a molar ratio of 1/3 at 20 bar.

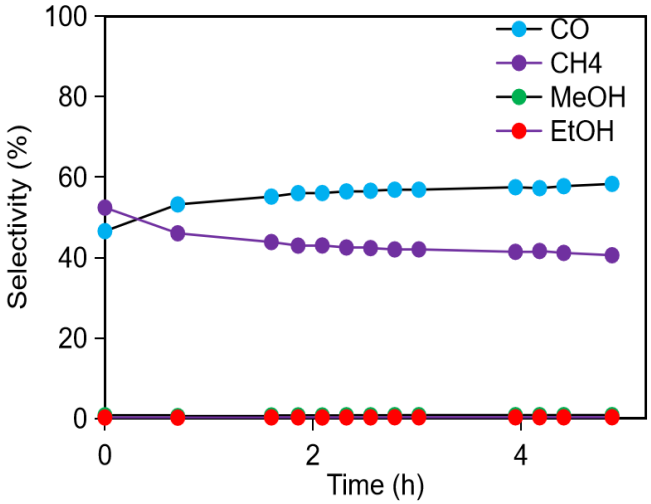

Figure 44. Results of catalytic testing of a 100mg of 0.5 wt% Rh/SiO_2 under a flow of 20 mL/min of CO_2/H_2 with a molar ratio of 1/3 at 20 bar.

The same catalysts were also tested at only one temperature (250°C) to check the stability of the catalysts and the same trend was observed: by increasing the active phase CO concentration decreased and methane concentration increased, possibly showing that only by increasing the loading of the metal it is possible to favour the RWGS reaction and slightly inhibit methanation reaction. However, again, the test with 1 wt% Rh/SiO2 gave contradictory results, indicating maybe a problem with the material synthesis itself. For this reason it is not showed in the study. Another synthesis might be necessary, which for time reasons couldn't be carried out.

4.2 Catalyst characterization

4.2.1 XPS characterization

To evaluate the oxidation state of the active phase in the nanocatalysts, XPS analyzes were performed. During the preparation of the catalysts, the sample at 1 wt% Rh on meso-SiO2 was subjected to hot water washing in order to eliminate any residual polymeric coating around the metal NPs which would have led to the degradation of the stabilizers during the catalytic reaction. To verify the effectiveness of the washing phase in reducing the atomic percentage of C, as a first analysis at the TEM, the spectra of Rh and Si have been studied in which the pre (in black) and post washed (in red) sample were compared. In addition, the spent sample was analysed, which was reported in the same graph (in blue) to be able to compare it with the fresh.

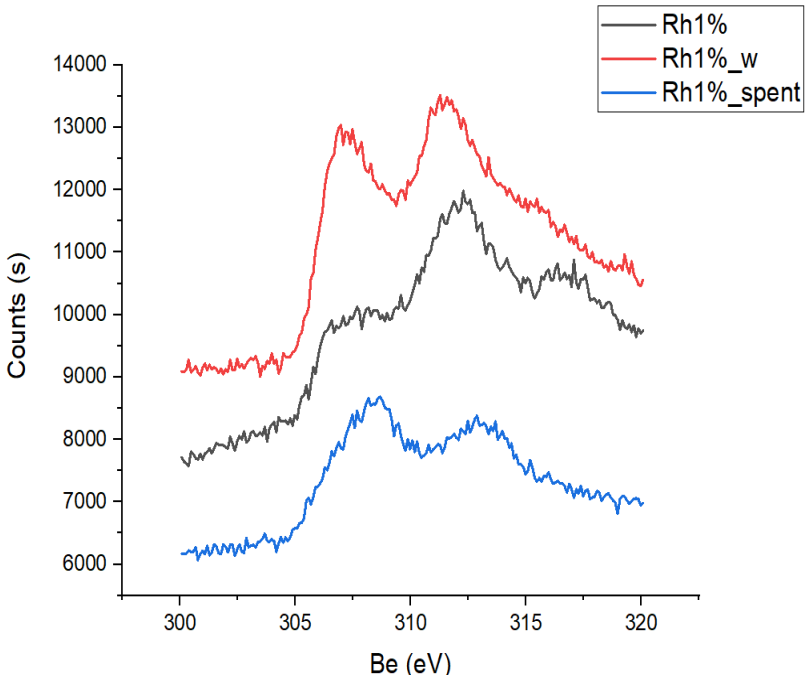

Figure 45. XPS spectra of Rh from the 1wt% Rh/mesosilica with and without being washed (respectively, red and black lines), as well as after the reaction (in blue).

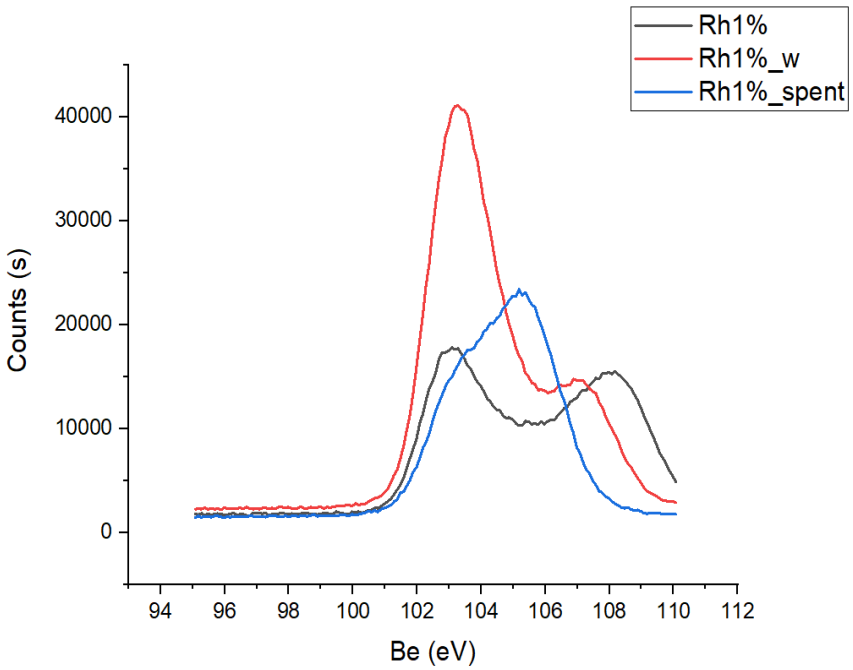

Figure 46. XPS spectra of Si from the 1wt% Rh/mesosilica with and without being washed (respectively, red and black lines), as well as after the reaction (in blue).

As expected, the XPS spectra of Rh (Figure 45) showed the presence of Rh in the metallic state (Rh^0). The peaks are composed of spin-orbit doublets (Rh 3d5/2 and Rh3d3/2). They have characteristic binding energy peaks at 306 and 311 eV for the Rh 3d5/2 and 3d3/2 electrons, respectively. Comparing the untreated fresh material with its spent counterpart (black and blue spectra), a strong presence of rhodium oxide can be observed in the untreated material due to the large peak and the peculiar peak shift towards a higher binding energy (highlighted in Table 7 below).

As regards the silica spectra (Figure 46), they present the complex multiplets relating to the mixed form of silica oxide. Although a correct interpretation was not possible, the XPS confirmed the presence of silica on the support and therefore the validity of the synthesis strategy adopted.

As for the washing step, its efficiency in removing polymeric coating around metal NPs can be confirmed by performing a qualitative comparison of the Rh spectra in Figure 45. From the table below (Table 7), the atomic % of C passed from 10.71% to 6.4% in the treated sample. Moreover, the major presence of Rh^0 valent on the sample treated with hot water is evidenced by the lower BE values.

Subsequently, the catalysts with different metal loading (1, 0.5, 0.25 %) were analysed. Also in this case, a co-presence of metal state and oxide was highlighted. A right quantification can be calculated by deconvolution analysis of the peak. The presence of Rh oxide justifies the employment of reduction with hydrogen before the catalytic reaction.

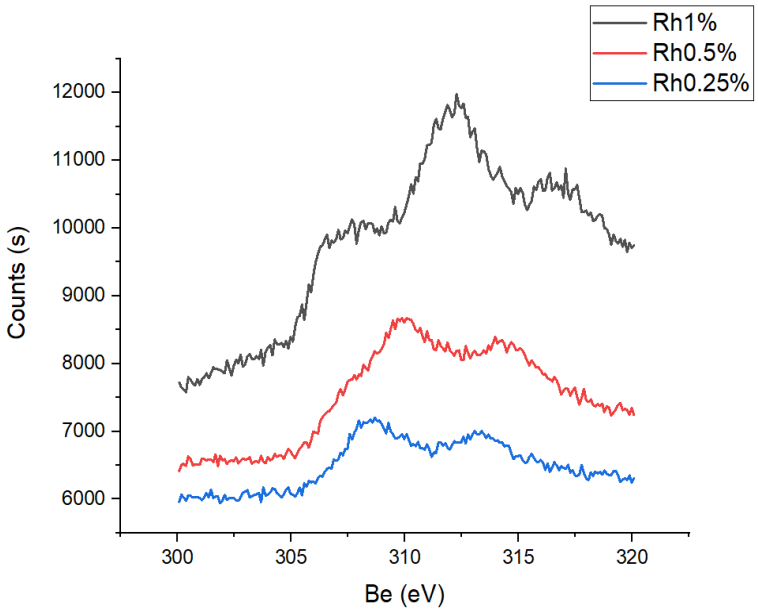

Figure 47. XPS spectra of 1wt%, Rh5 Si with and without being washed (respectively, red and black curve), as well as after the reaction (in blue).

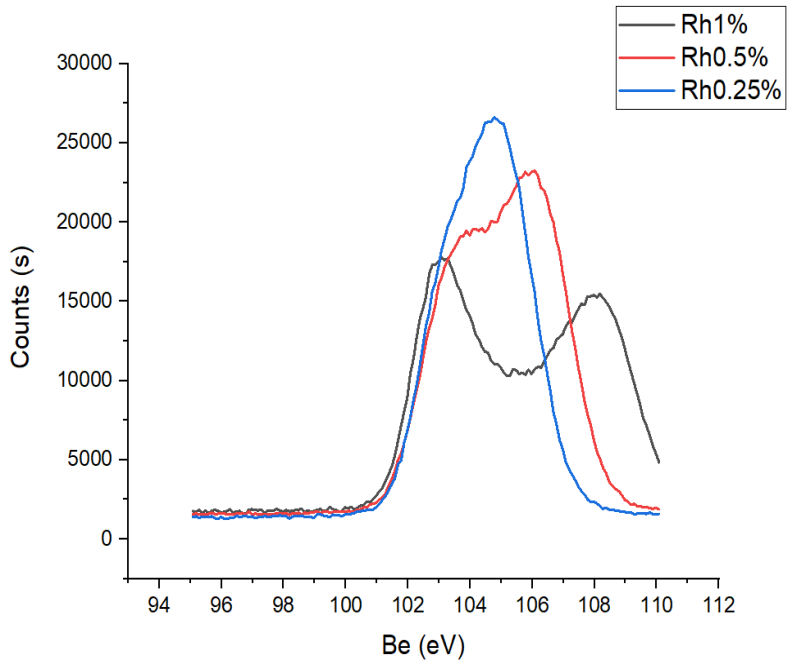

Figure 48. XPS spectra of Rh Si with different metal loading (0.25%, 0.5%, and 1%), both with and without being washed (respectively, red and black curve), as well as after the reaction (in blue).

At the end, the catalyst that showed the best results (RhFe/meso-silica@Li10%) was subjected to characterization in fresh and spent form at both 20 and 80 bar. The Rh spectra (figure 49) showed the presence of Rh oxide in the fresh sample, after the reaction for both pressures only metallic rhodium is present. Regarding the Fe spectra (Figure 50), a large peak can be observed due to the classical behaviour of the iron system to have different oxidation states. That is why a specific assessment of what kind of iron species is not possible without further analysis combined with the deconvolution approach.

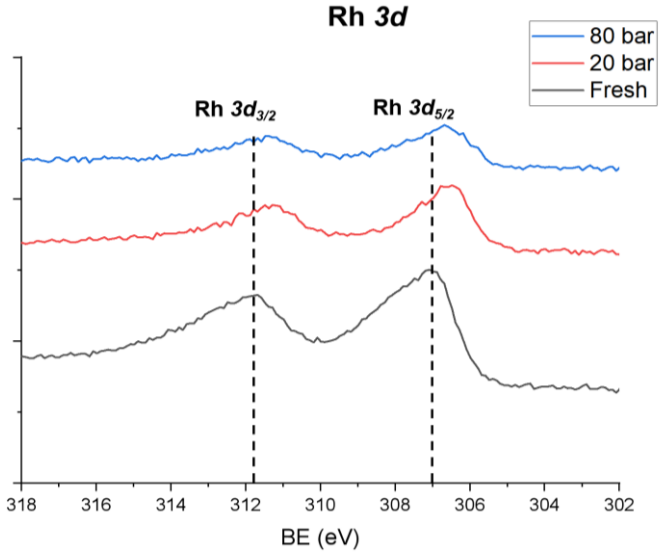

Figure 49. XPS spectra of 1 wt% Rh/mesosilca: Rh pattern.

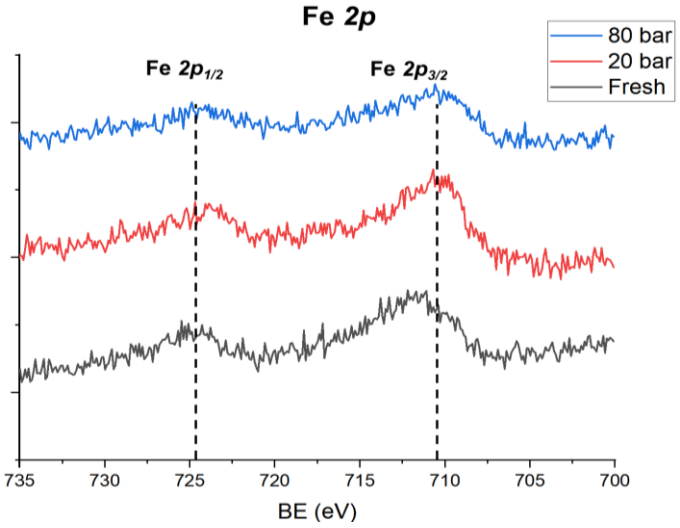

Figure 50. XPS spectra of 1 wt% Rh/mesosilca: Fe pattern.

	1 wt%Rh/mesoSiO$_2$	Peak BE	FWHM eV	Atomic %
Si2p	Not washed	104.1	4.12	28.3
	Washed	105.0	4.14	80.0
C1s	Not washed	288.0	6.08	10.7
	Washed	286.1	4.04	6.4
O1s	Not washed	533.9	4.71	60.6
	Washed	534.1	4.39	63.0
Rh3d	Not washed	312.4	11.23	0.46
	Washed	309.0	5.3	0.3

Table 7. Summary of results obtained from the XPS analysis of the washed and not wasted Rh/mesosilica sample.

4.3.2 BET characterization

Barrett, Joyner, and Halenda (BJH) analysis was employed to determine the pore area and specific pore volume using adsorption and desorption techniques. This technique characterizes pore size distribution independent of the external area due to the particle size of the sample.

4.3.2.1 Mesosilica calcined - 330°C vs 550°C

First, a comparison was done between the meso-SiO_2 calcined at 330°C and the one calcined at 550°C (Figure 51). As shown in the table below (Table 8), as the calcination temperature increased, a moderate decrease of the surface area of the material and in the micropore volume was observed. This might have been due to the increase in particle size and the degree of agglomeration following the sintering that occurs in the material.

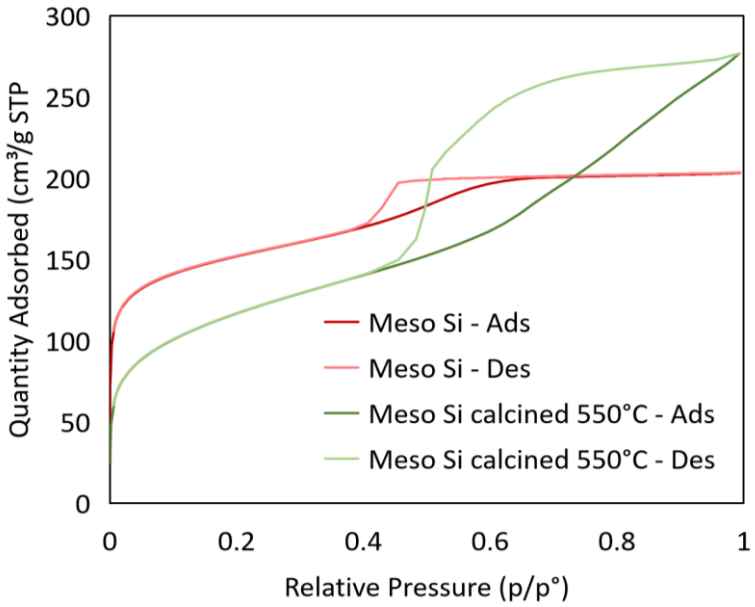

Figure 51. Nitrogen adsorption/desorption isotherms of mesosilica support calcined at different temperatures (330°C vs 550°C).

	BET Surface Area (m^2/g)	Micropore volume (cm^3/g)
meso-SiO2 calc 330°C	561.6	0.1331
meso-SiO_2 calc 550°C	413.8	0.03

Table 8. Comparison of BET Surface area (m^2/g) and micropore volume (cm^3/g) of mesosilica calcined at 330°C and 550°C.

On comparison the presently synthesized mesosilica shows significantly lower surface area than reported in the literature (about 650 m^2/g)[276]. This difference might be attributed to the synthesis procedure, precursor and surfactant used.

4.3.2.2 Meso-SiO_2 - Li0.5% vs Li1%

In the plot (Figure 52), it is possible to notice that the bare silica is mesoporous, but in the meso-SiO2 with lithium the bare silica has a completely different pore structure, even though they both have a well-defined pore structure.

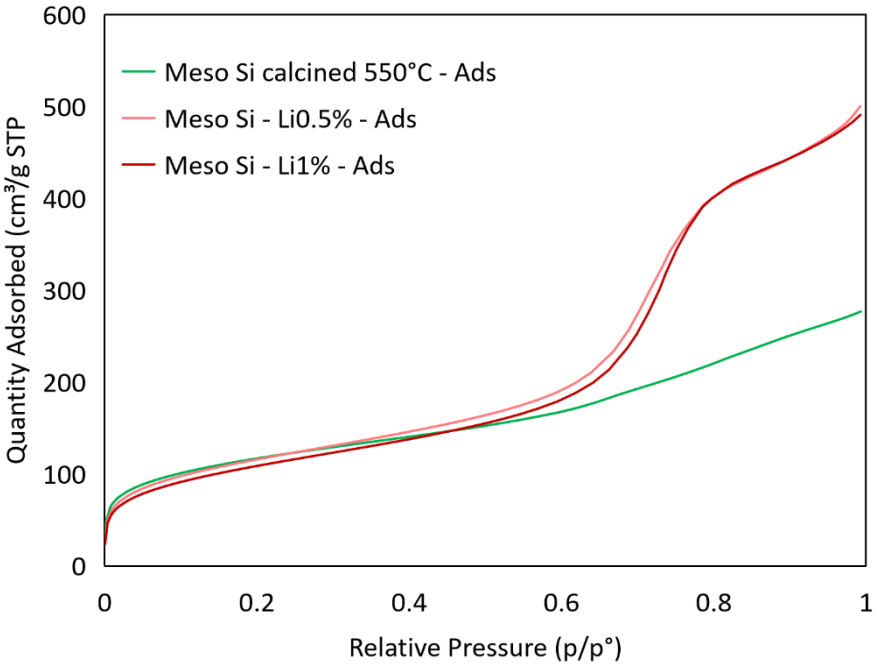

Figure 52. Comparison between nitrogen adsorption isotherms of mesosilica support calcined at 550°C, mesosilica doped with 0.5 wt% Li and 1 wt% Li.

	BET Surface Area (m^2/g)	**Micropore volume (cm^3/g)**
meso-SiO_2 calc 550°C	413.8	0.027
meso-SiO_2@Li0.5%	418.1	0.007
meso-SiO_2@Li1%	394.2	0.003

Table 9. Comparison of BET Surface area (m^2/g) and micropore volume (cm^3/g) of mesosilica calcined at 550°C, mesosilica@Li0.5% and Li1%.

BET gas adsorption experiments indicate that meso-SiO2 has actually a mesoporous structure. Table 9 indicates that the BET surface area of the bare silica is, again, lower than the one reported in literature for mesosilicas and then it decreases with the addition of 1 wt% Li due to the decrease of the pore volume, when the pore size was continuously reduced. The BJH Adsorption analysis in Figure 53 indicates that meso-SiO2 has a consistent pore size distribution that is throughout the structure of the material. Most of the pores have an average pore size diameter near 6.2 nm for the bare mesosilica, about 7.66 nm for Rh/mesosilica@Li0.5% and 7.41 nm for Rh/mesosilica@Li1%.

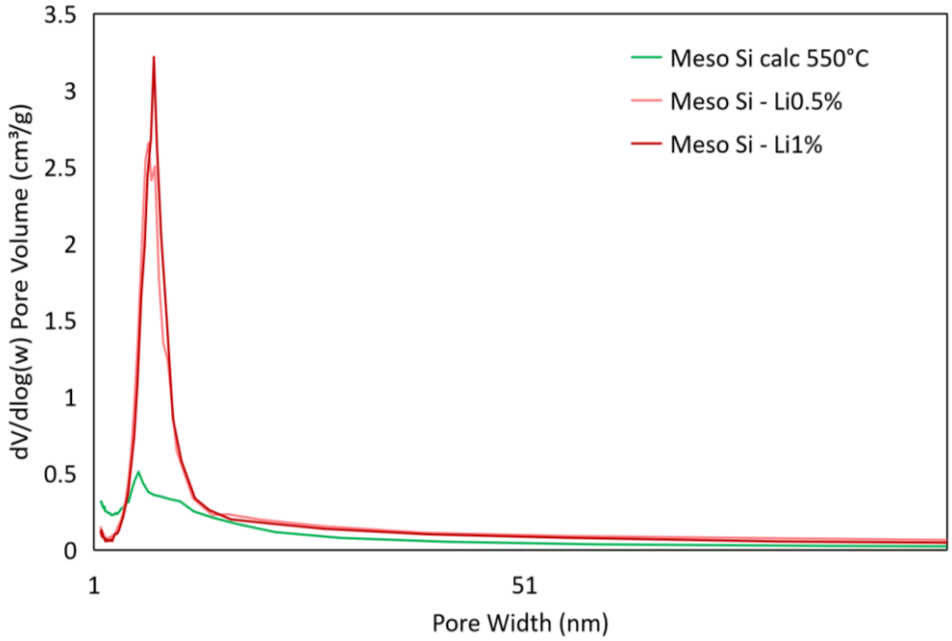

Figure 53. BET pore size distribution for of mesosilica support calcined at 550°C, mesosilica doped with 0.5 wt% Li and 1 wt% Li.

4.3.2.3 Rh/meso-SiO_2

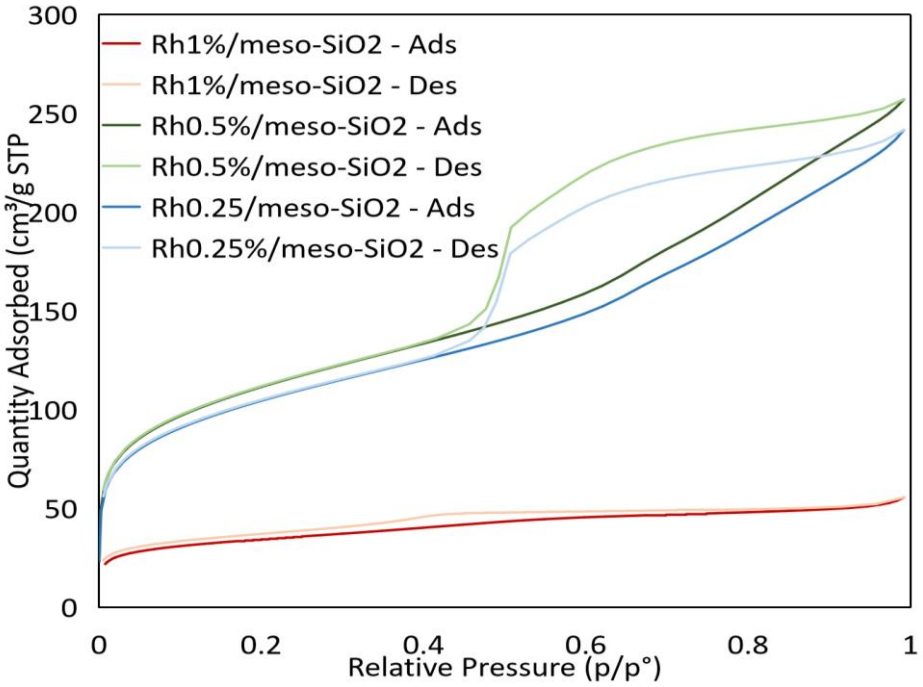

Figure 54. Comparison between nitrogen adsorption isotherms of meso-SiO2 support with different loading of Rh (0.25%, 0.5%, and 1%).

The adsorption isotherms of 0.25 wt% Rh/meso-SiO_2 and 0.5 wt% Rh/meso-SiO_2 (Figure 54) resemble the measurement of the meso-SiO_2 calcined at 550°C. The samples are definitely mesoporous, but they don't have the well-defined pore structure, as the one showed for the samples meso-SiO_2 0.5% Li and meso-SiO_2 1% Li in figure 52.

As for 1 wt% Rh/meso-SiO_2, the first data point took almost 3 hours. That is even slower than in the measurement done on the meso-SiO_2 sample calcined at 550°C.

That slow adsorption might indicate that slow diffusion in very narrow pores with a diameter of about 0.4 nm is hindering normal adsorption. Two possible explanations for the presence of such narrow pores might be:

- The pore structure collapsed,
- Something is partially blocking the pores,
- or a combination of the two alternatives.

For this measurement, it was not possible to use the t-plot to calculate the micropore volume, because the t-plot method is not valid for this isotherm. The adsorption continues to increase at all relative pressures; there is no real plateau that indicates the completion of the micropore filling. Therefore, it is not possible to distinguish between the micropores and the mesopores. The value for the micropore volume shown in the table below (Table 10) is too high because it would include also the supermicropores and the small mesopores in the micropore volume. Moreover, the table below (Table 10) showed decreasing BET surface area with increasing loading of the metal.

	BET Surface Area (m^2/g)	Micropore volume (cm^3/g)
Rh1%/mesoSiO$_2$	124.5	0.063
Rh0.5%/mesoSiO$_2$	402.5	0.075
Rh0.25%/mesoSiO$_2$	377.5	0.069

Table 10. Comparison of BET Surface area (m^2/g) and micropore volume (cm^3/g) of mesosilica with increasing Rh loading (0.25%, 0.5%, and 1%).

4.3.3 TEM characterization

Figures 55 and 56 are TEM analysed images of mesoporous silica, respectively, before and after the 5 h calcination at 550°C. Comparing the two figures, after calcination (Figure 56), it is possible to see how the organic template has clearly been removed from the support, while preserving the silica meso-structure.

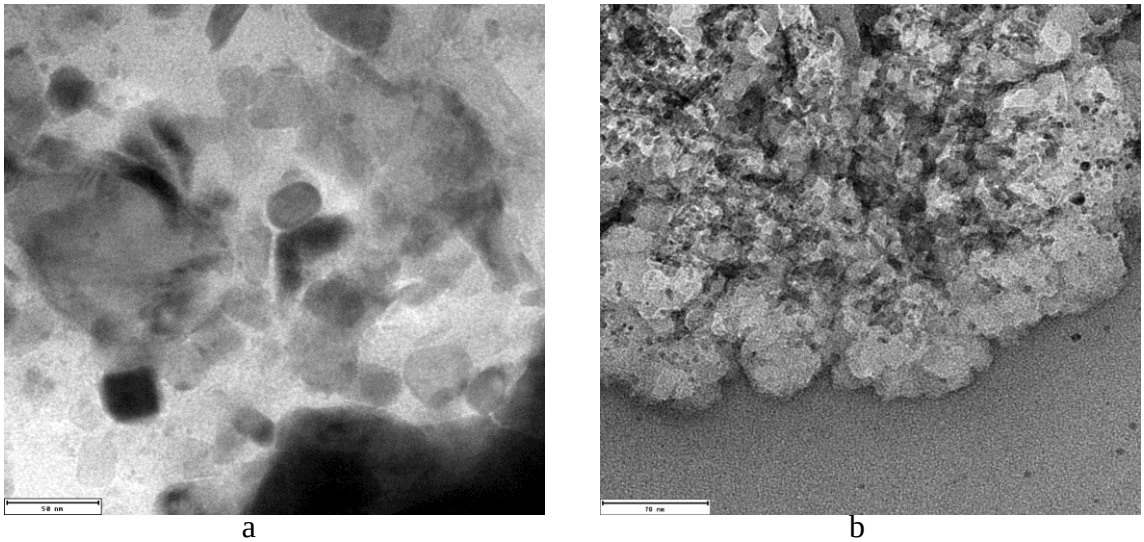

a b

Figure 55. TEM results for meso-SiO_2 before calcination (100 nm scale).

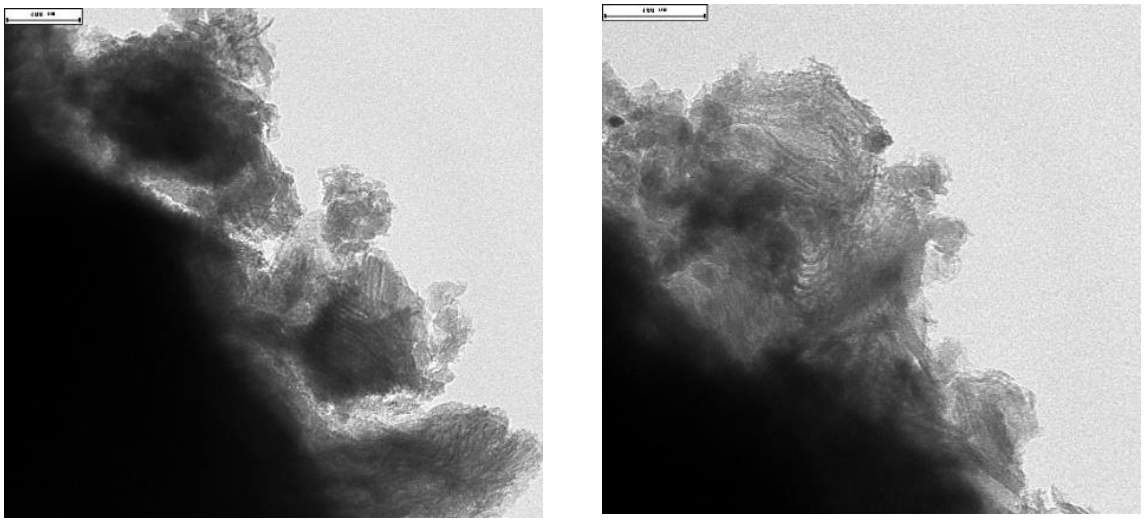

c d

Figure 56. TEM results for meso-SiO_2 after calcination at 550°C (100 nm scale).

Figures 57 (e and f) show the addition of the active phase (Rh) on the meso-structure, indicated by the darker spots on the images. Rh (3.08 nm) appears to be well-distributed thanks to the sol-immobilization method, which allows a good control over the catalyst structure. Figure d and e showed that, even after performing the reaction at 20 bar, the silica matrix was not perturbed, meaning that the reaction caused no nanoparticle aggregation and little change to the particles' appearances.

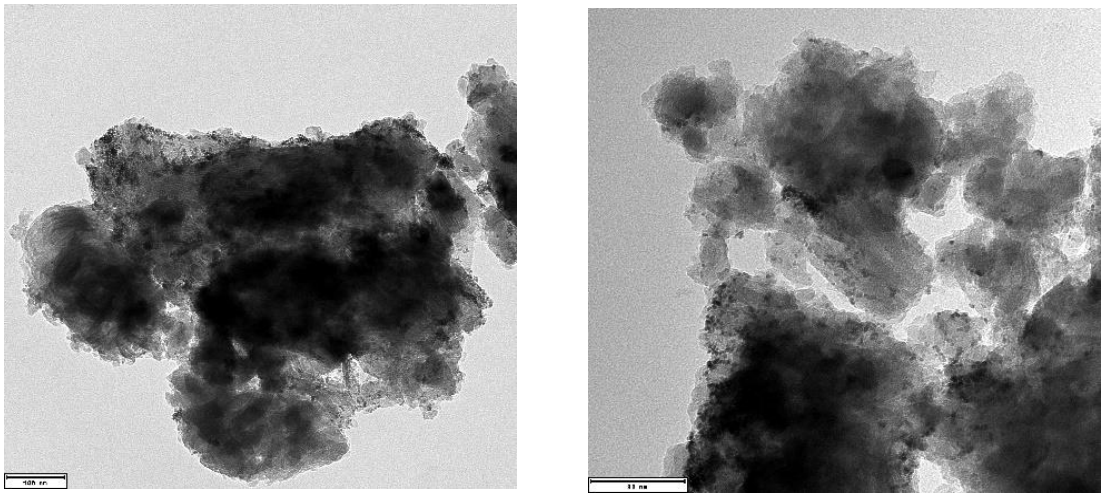

e f

Figure 57. TEM results for 0.5 wt% Rh/meso-SiO_2 before reaction (e at 100 nm scale and f at 80 nm scale).

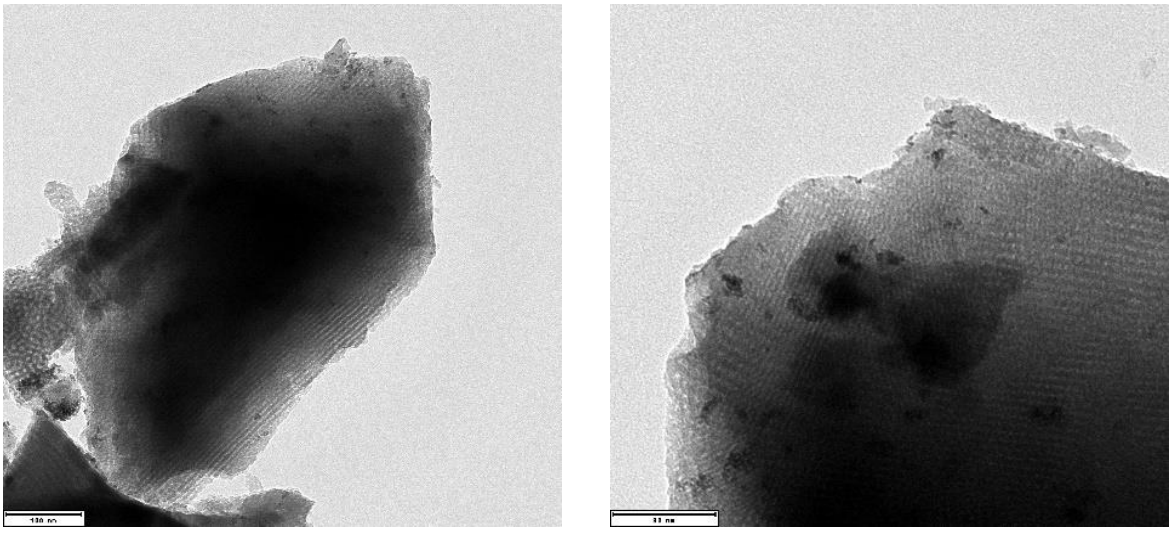

g h

Figure 58. TEM results for 1 wt% Rh/meso-SiO_2 before reaction (g at 100 nm scale and h at 80 nm scale).

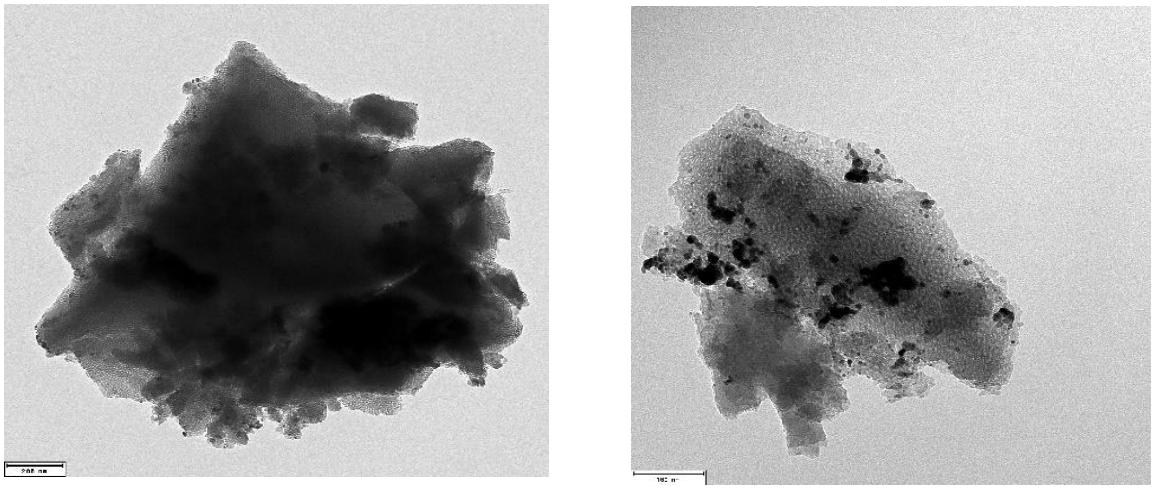

i j

Figure 59. TEM results for 1 wt% Rh/meso-SiO_2 after reaction (I at 200 nm scale and j at 100 nm scale).

Figures 60 and 61 below represents, respectively, the structure of the mesosilica doped with Li, and the structure of the doped support on which the metal was deposited. In particular, while Figure 60l shows the meso-structure of the SiO_2, in Figure 60k, instead, it is possible to identify the formation of elongated and symmetrical structures. These might be due to the formation of Lithium Chloride (LiCl) that crystallize as hydrate (LiCl $2H_2O$). LiCl is both hygroscopic and deliquescent, meaning it readily absorbs water (usually from the atmosphere), even to the point of dissolving in the sorbed water and turning into a liquid form. This probably explains why the more the structure gets exposed to the air the more is prone to melting, which is showed in Figure 61 (o and p). For this reason, protecting the solid from excessive moisture exposure is the primary requirement to maintain product quality while in storage. In most cases, the water can be removed from the material performing a heating treatment (sometimes under vacuum or under a flow of dry gas such as nitrogen).

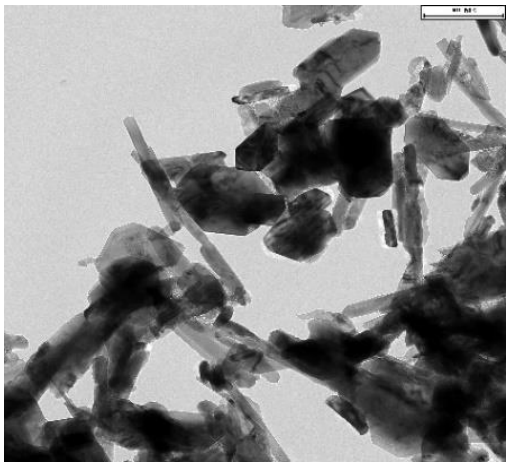

k

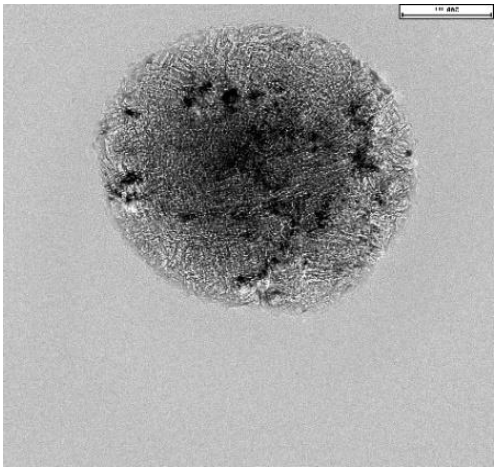

l

Figure 60. TEM results for meso-SiO2@Li10%.

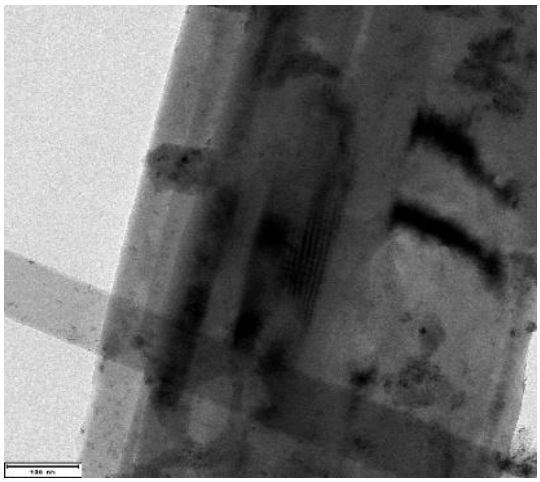

m

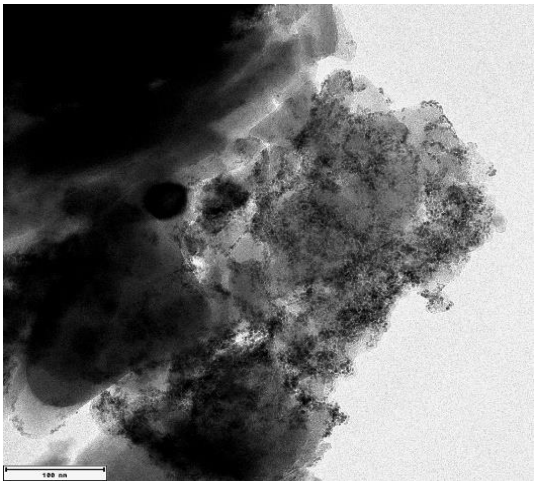

n

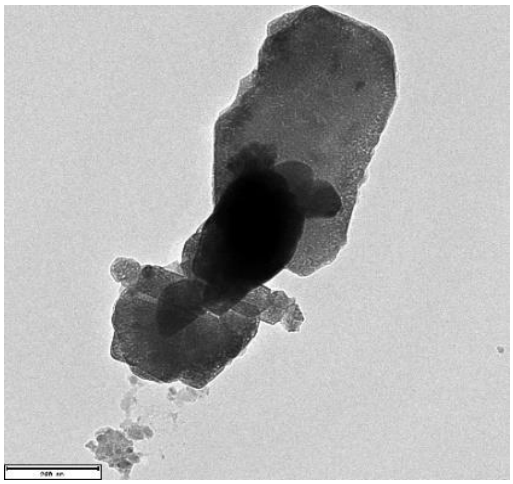

o

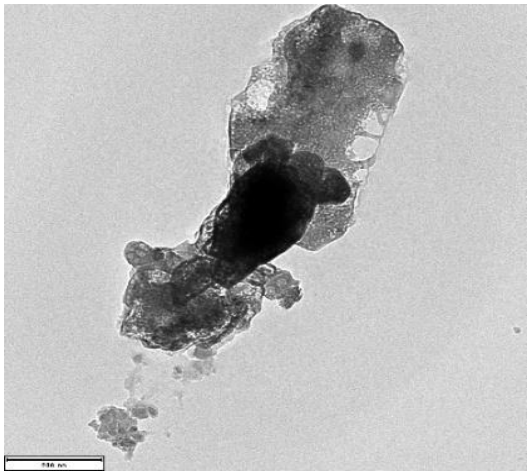

p

Figure 61. TEM results for Rh1%/meso-SiO2@Li10%.

Figure 62 shows how the meso-structure is maintained even after the reaction both at 20 bar (q) and 80 bar (r), which indicates a strong and solid structure thanks to the support. Rh appears well-distributed on the support. However, Rh particle growth for the Rh/mesosilica@Li10 catalyst were revealed during catalysis.

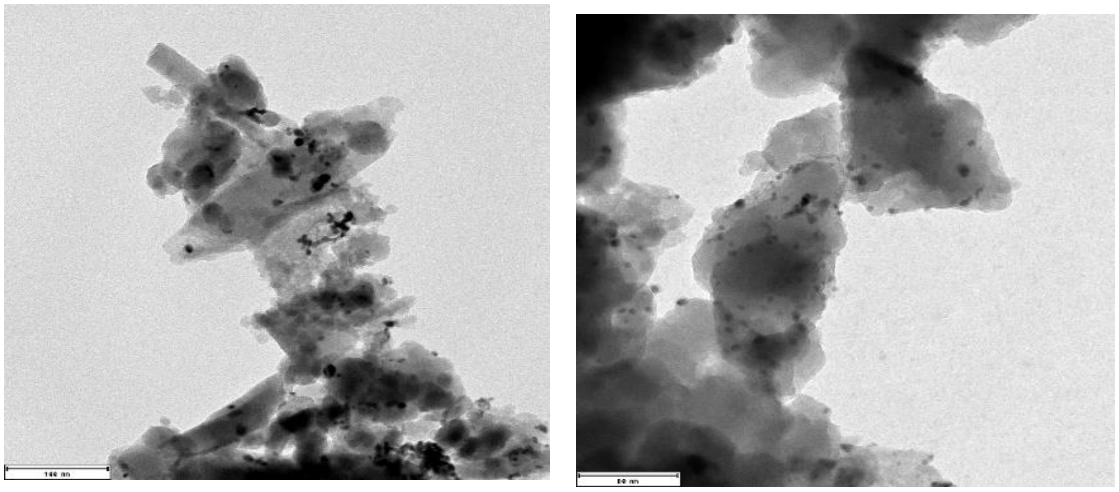

q r

Figure 62. TEM results for Rh1%/meso-SiO2@Li10% spent under 20 bar (q) and 80 bar (r).

The same can be said in case of figure 63 where the second metal is added to the catalyst structure. The alloy structure might be represented by the bigger darker chunks formed, which appear to be well-integrated in the meso-SiO_2 structure. Figure 63 shows how the catalyst structure is preserved, even after being subjected to 80 bar pressure.

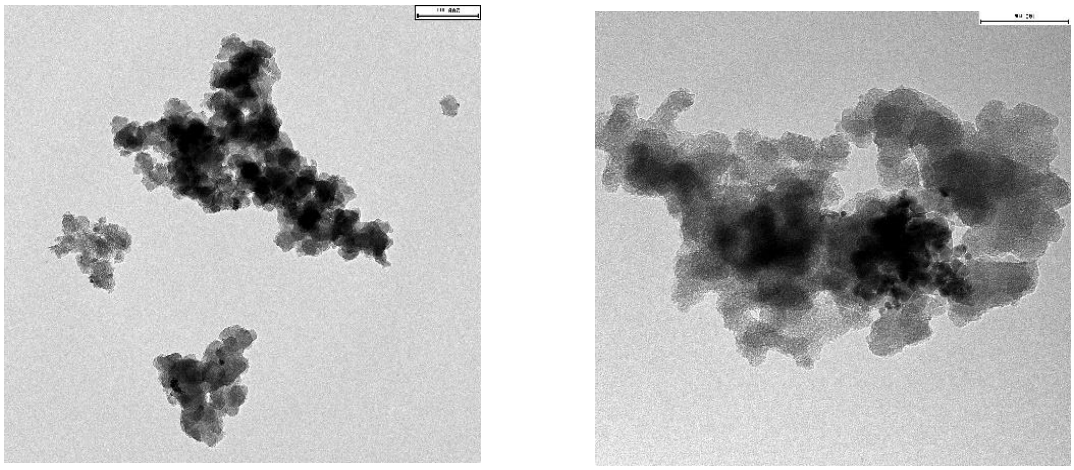

s t

Figure 63. TEM results for 1 wt% RhFe%/meso-SiO2@Li10%.

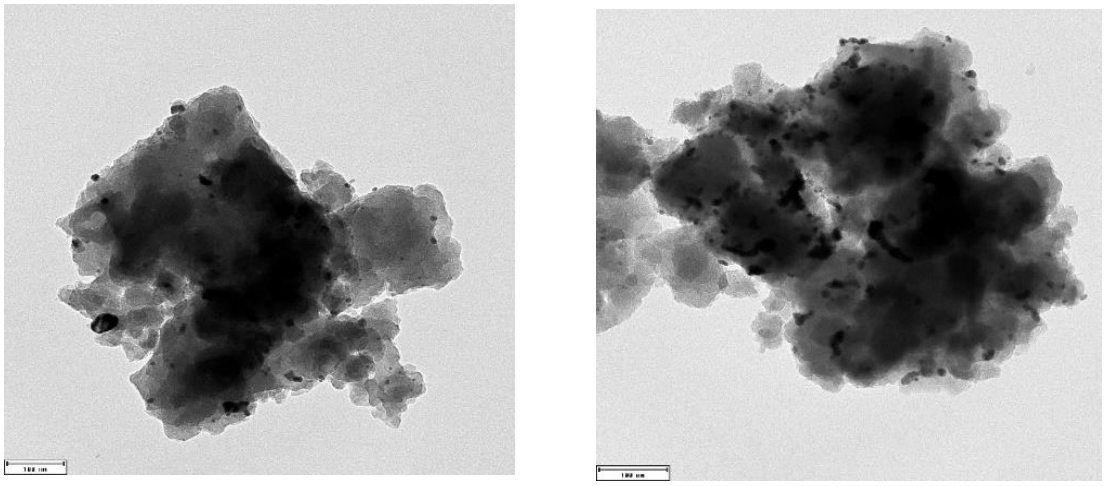

u v

Figure 64. TEM results for 1 wt% RhFe%/meso-SiO2@Li10% spent under 20 bar (u) and 80 bar (v).

For some of the images obtained from TEM and, in particular, for Rh0.5/mesosilica, Rh1/mesosilica, Rh1/mesosilica@Li10% and RhFe/mesosilica@Li10%, the particle sizes of at least 100 random particles of the samples were manually analyzed using the ImageJ Open Source Image Analysis Program (version 1.51, NIH, Bethesda, MD, USA) and the line measurement tool. The results are summarized in the table below (Table 11). Small variations in the particle size were detected between all the samples, except for 1wt%Rh/mesosilica where it's actually almost 4 times higher. This explains the abnormal behaviour in the catalytic testing as well as for the very different structure showed in the TEM images (58 and 59).

Fresh catalyst	**Rh diameter (nm)**
Rh0.5/mesoSiO$_2$	3.08
Rh1/mesoSiO$_2$	11.82
1wt%Rh/mesoSiO$_2$@Li10%	2.76
1wt%RhFe/mesoSiO2@Li10%	3.18

Table 11. Summary of Rh particles diameter over 100 random particles using ImageJ software.

Finally, commercial SiO2 microparticles were analysed with TEM. The ultra-small particles are easily detectable from the picture.

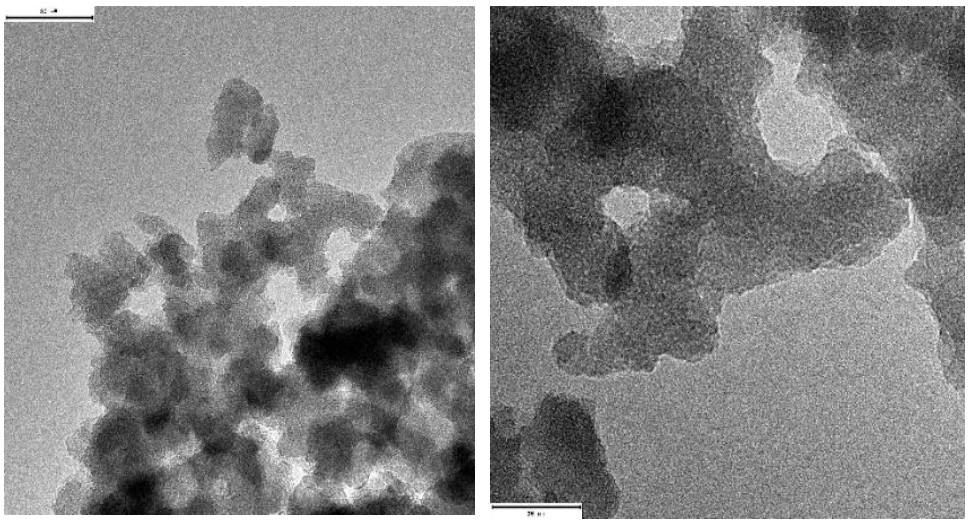

x y

Figure 65. TEM results for commercial SiO_2 nanoparticles.

Figure 66 shows the difference between the same catalyst (Rh/SiO_2) prepared with two different methods: IWI (z) and sol-immobilization (z), where the first was synthetized by another student (Singh B.) during his research project. It is clear how different is structure. In the catalyst prepared with sol-immobilization method Rh appears well-dispersed among the support, which might strongly affect the catalytic performance of the catalyst. In Figure 67 it is possible to confirm the stability of the structure, even though some bigger points are present, which might be due to an agglomeration of the metal.

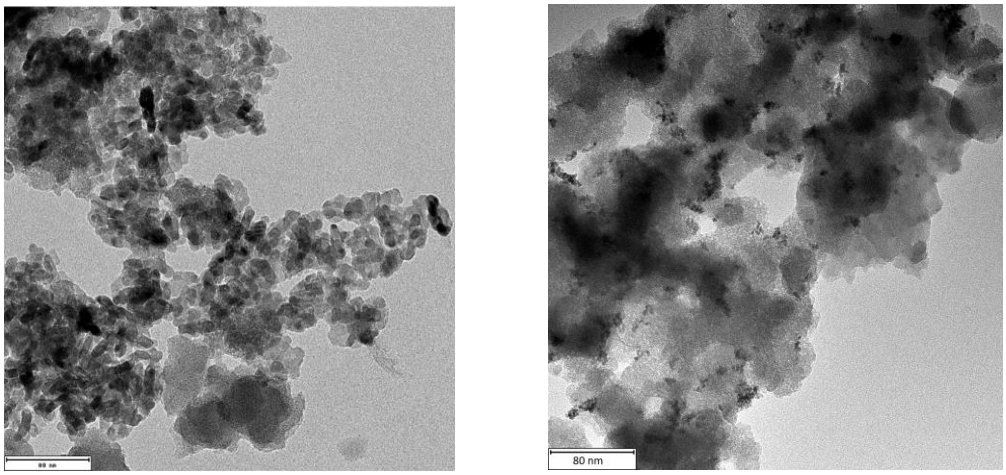

z z1

Figure 66. Comparison between the TEM results for 1 wt% Rh/SiO_2 using commercial silica. The one on the left was prepared with the IWI method by Singh B., 2021 [Singh B., 2021, Catalytic hydrogenation of CO2 to higher alcohols at elevated pressure, Master of Science, TU Delft, Delft] and the one on the right with the sol-immobilization method.

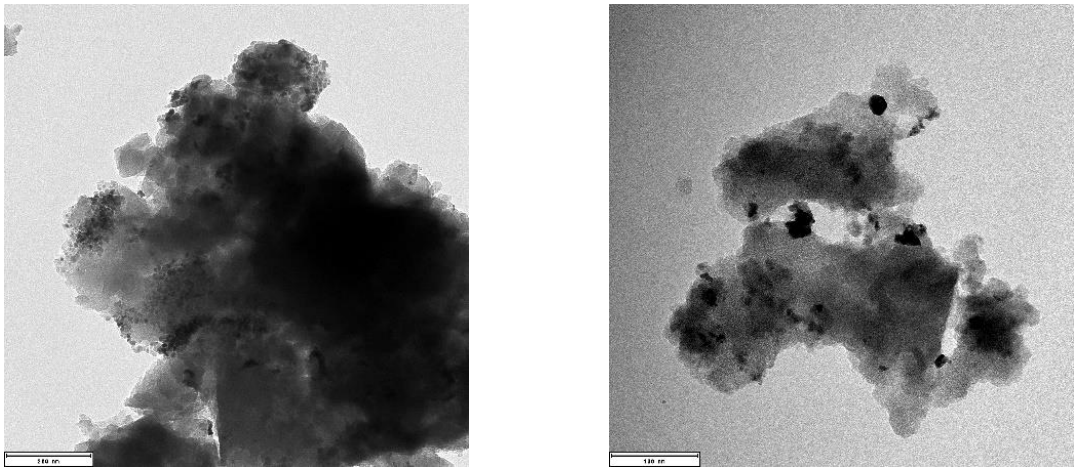

z2 z3

Figure 67. TEM results for 1 wt% Rh/SiO_2 using commercial silica spent under 20 bar.

5 Conclusions and future recommendations

- A study on the CO_2 hydrogenation reaction to higher alcohols was performed. Following literature studies and previous results obtained by other students in the research group, supported rhodium Rh NPs on mesosilica have been chosen as metal catalyst.
- For the catalyst screening, the same catalyst was first tested at different loading of Rh (0.25wt%, 0.5wt%, and 1wt%); then, at different quantities of Li (0.5wt% and 1wt%) while keeping the same Rh loading (1wt%). The same reaction was performed at 20 bar and varying the temperature from 180 °C to 250°C and under 10 ml/min of CO_2/H_2 flow with a molar ratio of 1/3. After, the reaction was performed keeping a constant loading of Li (10wt%), but varying the one of Rh (1wt% and 3 wt%), and then keeping a constant Li and Rh loadings (10wt% and 1wt%, respectively), but adding a second metal (Fe) at 1wt%. In this case, the pressure was kept at 20 bar, but at a constant temperature of 250°C for 6h, always under 10 ml/min of CO_2/H_2 flow with a molar ratio of 1/3. The 1wt%Rh/meso-SiO_2@Li10% and the 1wt%RhFe/meso-SiO_2@Li10% catalysts gave the best results in terms of CO_2 conversion: respectively, 14.2% and 5%. Thus, these two catalysts were tested also at 80 bar and at 250°C, under 10 ml/min of CO_2/H_2 flow with a molar ratio of 1/3. At higher pressure, 1wt%Rh/meso-SiO_2@Li10% gave the best results in terms of CO_2 conversion (14.3%) and 1wt%RhFe/meso-SiO_2@Li10% in terms of methanol selectivity (5.8%) of methanol selectivity. These results proved the importance of adding Li and Fe, as well as of increasing the pressure to enhance the catalytic activity of Rh/meso-SiO_2 catalyst in CO_2 hydrogenation reaction towards alcohols.
- Since no variation of the contact time were performed, it could be useful to do it and compare any possible difference in catalytic activity. Moreover, in previous projects, the use of high pressures (360 bar) has showed to significantly enhance the catalytic performance of the Rh catalysis on silica and titanium oxide supports. Therefore, it could be valuable to test the same

catalysts (Rh/meso-SiO_2@Li and RhFe/meso-SiO_2@Li) using extremely higher pressure conditions (360 bar).

- Mesosilica was chosen as support to allow stabilization of the metal NPs as well as good dispersion of Rh NPs.
- The sol-immobilization was chosen as catalyst synthesis method. Compared to conventional techniques, such as wet impregnation and deposition–precipitation, sol immobilization allows, instead, a good control of the catalyst morphology and metal particle size. To increase the interaction between the rhodium and the promoters, it would be valuable to try synthesizing promoted rhodium-based catalysts using other preparation methods, such as the co-precipitation method or the strong electrostatic adsorption method.
- Due to the high redox potential of Fe, it was not possible to use the sol immobilization for the preparation of the supported RhFeLi alloy NPs. Therefore, an innovative hybrid method was developed, combining sol immobilization with impregnation. However, another alternative methods for synthesizing RhFe/meso-SiO_2@Li can be searched, maybe changing the Fe precursor or working under better controlled anaerobic conditions.
- The BET analysis showed that there could be something blocking the pores in the mesosilica structure or that the porous structure might have collapsed (or a combination of both). This can explain the discrepancy observed in some results, as well as an overall low catalytic activity of the synthesised catalyst in the CO_2 hydrogenation reaction.
- The validity of the synthesis strategy for the catalyst adopted was confirmed by the characterization analysis. XPS spectra confirmed the desired species as well as underlined the efficiency of washing the support with hot water in order to remove polymeric coating around metal NPs (% C passed from 10.71% to 6.4% in the treated sample). The BET analysis of mesoporous silica depicted surface area of 413.81 m^2/g with a micropore volume of 0.0272 cm^3/g. TEM analysis showed a stable mesoporous structure with uniform dispersion of Rh nanoparticles throughout all the surface and Rh nanoparticles with diameters of about 3 nm.

- During XPS analysis of RhFe/meso-SiO_2@Li10%, Rh spectra showed the presence of Rh oxide in the fresh sample, after the reaction for both pressures only metallic rhodium is present. Regarding the Fe spectra, a large peak can be observed due to the classical behaviour of the Fe system to have different oxidation states. That is why further analysis combined with the deconvolution approach would be necessary for specific assessment of what kind of iron species are formed.
- Performing in situ DRIFTS can be done to gain a better understanding of the CO_2 hydrogenation reaction using the synthesised catalyst. In a previous project, a student performed in situ DRIFTS for this reaction using Rh NPs supported on commercial silica nanoparticles. One of the findings was that the introduction of promoters introduced carbonyl on oxidized Rh to the catalyst. However, no detailed knowledge was gained on the oxidation state of the catalyst during the reaction. For this, it would therefore be extremely valuable to do XAS experiments.
- The present study concludes the overall unsuccessful application of synthesized supported Rh NPs on mesoporous SiO_2 for the CO_2 hydrogenation reaction towards higher alcohols, but good results for methanol production. Following the recent studies, alternative catalysts can be proposed instead of supported Rh NPs. Recently, it has been discovered how the entrapment of the small particles in the porous structure of zeolite stabilizes the active surfaces, promoting the reaction of adsorbed CO_2 and methyl intermediates to ethanol[6]. The Cu@Na-Beta catalyst with 2–5 nm Cu particles embedded in the Na-beta zeolite seems to be a promising catalyst. At 2.1 MPa and 300°C, it resulted in 79% of ethanol selectivity and 8.65 mmol $gcat^{-1}$ h^{-1} of ethanol STY, with CO as the only by product.

Bibliography

(1) *7.4 Mechanism of reaction and catalysis | Rate and extent of reaction | Siyavula*. https://www.siyavula.com/read/za/physical-sciences/grade-12/rate-and-extent-of-reaction/07-rate-and-extent-of-reaction-04 (accessed 2023-03-09).

(2) Kakaei, K.; Esrafili, M. D.; Ehsani, A. Introduction to Catalysis. In *Interface Science and Technology*; Elsevier, 2019; Vol. 27, pp 1–21. https://doi.org/10.1016/B978-0-12-814523-4.00001-0.

(3) Zhao, X. S.; Bao, X. Y.; Guo, W.; Lee, F. Y. Immobilizing Catalysts on Porous Materials. *Mater. Today* **2006**, *9* (3), 32–39. https://doi.org/10.1016/S1369-7021(06)71388-8.

(4) Studies in Surface Science and Catalysis. In *Catalysis*; Moulijn, J. A., Leeuwen, P. W. N. M. van, Santen, R. A. van, Eds.; Studies in Surface Science and Catalysis; Elsevier, 1993; Vol. 79, pp 461–465. https://doi.org/10.1016/S0167-2991(08)63819-7.

(5) Sajid, E. M. Prepared by Engr. Muhammad Sajid B.Sc Chemcial Engineering M.Sc Chemical Engineering.

(6) Deutschmann, O.; Knözinger, H.; Kochloefl, K.; Turek, T. Heterogeneous Catalysis and Solid Catalysts; 2009. https://doi.org/10.1002/14356007.a05_313.pub2.

(7) *Homogeneous Catalysis: Understanding the Art - Piet W.N.M. van Leeuwen - Google Books*. https://books.google.com.gi/books?id=Ze0eQXJAUVwC&printsec=copyright&source=gbs_pub_info_r#v=onepage&q&f=false (accessed 2023-03-09).

(8) 18.12__Heterogeneous_Catalysis.Pdf.

(9) Ndolomingo, M. J. Review of Supported Metal Nanoparticles: Synthesis Methodologies, Advantages and Application as Catalysts. *J Mater Sci* **2020**.

(10) Bailie, J. E.; Hutchings, G. J.; O'Leary, S. Supported Catalysts. In *Encyclopedia of Materials: Science and Technology*; Buschow, K. H. J., Cahn, R. W., Flemings, M. C., Ilschner, B., Kramer, E. J., Mahajan, S., Veyssière, P., Eds.; Elsevier: Oxford, 2001; pp 8986–8990. https://doi.org/10.1016/B0-08-043152-6/01620-X.

(11) Ertl, E. G.; Kniizinger, H.; Weitkamp, J. HANDBOOK OF HETEROGENEOUS CATALYSIS.

(12) Niemantsverdriet, J. W.; Chorkendorff, I. *Concepts of Modern Catalysis and Kinetics*; John Wiley & Sons, 2006.

(13) Holm, A.; Goodman, E. D.; Stenlid, J. H.; Aitbekova, A.; Zelaya, R.; Diroll, B. T.; Johnston-Peck, A. C.; Kao, K.-C.; Frank, C. W.; Pettersson, L. G. M.; Cargnello, M. Nanoscale Spatial Distribution of Supported Nanoparticles Controls Activity and Stability in Powder Catalysts for CO Oxidation and Photocatalytic H_2 Evolution. *J. Am. Chem. Soc.* **2020**, *142* (34), 14481–14494. https://doi.org/10.1021/jacs.0c03842.

(14) Karim, N. A.; Kamarudin, S. K. Introduction to Direct Alcohol Fuel Cells (DAFCs). In *Direct Liquid Fuel Cells*; Elsevier, 2021; pp 49–70. https://doi.org/10.1016/B978-0-12-818624-4.00002-9.

(15) Che, M.; Bennett, C. O. The Influence of Particle Size on the Catalytic Properties of Supported Metals. In *Advances in Catalysis*; Elsevier, 1989; Vol. 36, pp 55–172.

(16) Alshammari. Heterogeneous Gold Catalysis: From Discovery to Applications. *Catalysts* **2019**, *9* (5), 402. https://doi.org/10.3390/catal9050402.

(17) Calderón, J. C.; Nieto-Monge, M. J.; Pérez-Rodríguez, S.; Pardo, J. I.; Moliner, R.; Lázaro, M. J. Palladium–Nickel Catalysts Supported on Different Chemically-Treated Carbon Blacks for Methanol Oxidation in Alkaline Media. *Int. J. Hydrog. Energy* **2016**, *41* (43), 19556–19569.

(18) Yan, R.; Sun, X.; Jin, B.; Li, D.; Zheng, J.; Li, Y. Preparation of Platinum/Polyaniline/Multi-Walled Carbon Nanotube Nanocomposite with Sugarcoated Haws Structure for Electrocatalytic Oxidation of Methanol. *Synth. Met.* **2019**, *250*, 146–151.

(19) Miecznikowski, K. WO3 Decorated Carbon Nanotube Supported PtSn Nanoparticles with Enhanced Activity towards Electrochemical Oxidation of Ethylene Glycol in Direct Alcohol Fuel Cells. *Arab. J. Chem.* **2020**, *13* (1), 1020–1031.

(20) Yahya, N.; Kamarudin, S. K.; Karim, N. A.; Masdar, M. S.; Loh, K. S.; Lim, K. L. Durability and Performance of Direct Glycerol Fuel Cell with Palladium-Aurum/Vapor Grown Carbon Nanofiber Support. *Energy Convers. Manag.* **2019**, *188*, 120–130.

(21) Xiao, H.; Zhang, J.; Zhao, M.; Hu, T.; Jia, J.; Wu, H. Hydrogenated Graphene as Support of Pd Nanoparticles with Improved Electrocatalytic Activity for Ethanol Oxidation Reaction in Alkaline Media. *Electrochimica Acta* **2019**, *297*, 856–863.

(22) *Encyclopedia of Materials: Science and Technology*; Buschow, K. H. J., Ed.; Elsevier: Amsterdam ; New York, 2001.

(23) Skjånes, K.; Knutsen, G.; Källqvist, T.; Lindblad, P. H2 Production from Marine and Freshwater Species of Green Algae during Sulfur Deprivation and Considerations for Bioreactor Design. *Int. J. Hydrog. Energy* **2008**, *33* (2), 511–521.

(24) Lou, Y.; Xu, J.; Zhang, Y.; Pan, C.; Dong, Y.; Zhu, Y. Metal-Support Interaction for Heterogeneous Catalysis: From Nanoparticles to Single Atoms. *Mater. Today Nano* **2020**, *12*, 100093. https://doi.org/10.1016/j.mtnano.2020.100093.

(25) Bond, G. C. The Modification of Catalytic Properties by Metal-Support Interactions. In *Studies in Surface Science and Catalysis*; Elsevier, 1982; Vol. 11, pp 1–10.

(26) Prieto, G.; Zečević, J.; Friedrich, H.; de Jong, K. P.; de Jongh, P. E. Towards Stable Catalysts by Controlling Collective Properties of Supported Metal Nanoparticles. *Nat. Mater.* **2013**, *12* (1), 34–39. https://doi.org/10.1038/nmat3471.

(27) Vandenbroucke, A. Afbraak van vluchtige organische stoffen door gecombineerd gebruik van niet-thermisch plasma en heterogene katalyse.

(28) 3-S2.0-B0123694019005416-Main.Pdf.

(29) White, R. J.; Luque, R.; Budarin, V. L.; Clark, J. H.; Macquarrie, D. J. Supported Metal Nanoparticles on Porous Materials. Methods and Applications. *Chem. Soc. Rev.* **2009**, *38* (2), 481–494.

(30) Feynman, R. Nanotechnology. *Caltechs Eng Sci* **1960**, *23*, 22–36.

(31) Nasrollahzadeh, M.; Sajadi, S. M.; Sajjadi, M.; Issaabadi, Z. An Introduction to Nanotechnology. In *Interface science and technology*; Elsevier, 2019; Vol. 28, pp 1–27.

(32) Feynman, R. P. There's Plenty of Room at the Bottom: An Invitation to Enter a New Field of Physics. *Miniaturization Reinhold* **1961**.

(33) Taniguchi, N. On the Basic Concept of Nanotechnology. *Proceeding ICPE* **1974**.

(34) Santamaria, A. Historical Overview of Nanotechnology and Nanotoxicology. *Nanotoxicity Methods Protoc.* **2012**, 1–12.

(35) Drexler, K. E. Molecular Engineering: An Approach to the Development of General Capabilities for Molecular Manipulation. *Proc. Natl. Acad. Sci.* **1981**, *78* (9), 5275–5278.

(36) Toumey, C. P. Reading Feynman into Nanotechnology: A Text for a New Science. *Techné Res. Philos. Technol.* **2008**, *12* (3), 133–168.

(37) Butt, H.-J.; Cappella, B.; Kappl, M. Force Measurements with the Atomic Force Microscope: Technique, Interpretation and Applications. *Surf. Sci. Rep.* **2005**, *59* (1–6), 1–152.

(38) Jeevanandam, J.; Barhoum, A.; Chan, Y. S.; Dufresne, A.; Danquah, M. K. Review on Nanoparticles and Nanostructured Materials: History, Sources, Toxicity and Regulations. *Beilstein J. Nanotechnol.* **2018**, *9* (1), 1050–1074.

(39) Ealia, S. A. M.; Saravanakumar, M. P. A Review on the Classification, Characterisation, Synthesis of Nanoparticles and Their Application. In *IOP conference series: materials science and engineering*; IOP Publishing, 2017; Vol. 263, p 032019.

(40) *Nanotechnology: Trends and Future Applications*; Tahir, M. B., Rafique, M., Sagir, M., Eds.; Springer Singapore: Singapore, 2021. https://doi.org/10.1007/978-981-15-9437-3.

(41) Kanoun, O.; Müller, C.; Benchirouf, A.; Sanli, A.; Bouhamed, A.; Al-Hamry, A.; Bu, L. Potential of Flexible Carbon Nanotube Films for High Performance Strain and Pressure Sensors; 2014; pp 148–183.

(42) Sannino, D. Types and Classification of Nanomaterials. *Nanotechnol. Trends Future Appl.* **2021**, 15–38.

(43) Yao, Y.; Wei, Y.; Chen, S. Size Effect of the Surface Energy Density of Nanoparticles. *Surf. Sci.* **2015**, *636*, 19–24.

(44) Gene, A. S. STRUCTURAL, OPTICAL AND MAGNETIC CHARACTERIZATION OF SPINEL ZINC CHROMITE (ZnCr2O4) NANOCRYSTALS SYNTHESIZED BY THERMAL TREATMENT METHOD. **2014**.

(45) Fuller, S. B.; Wilhelm, E. J.; Jacobson, J. M. Ink-Jet Printed Nanoparticle Microelectromechanical Systems. *J. Microelectromechanical Syst.* **2002**, *11* (1), 54–60. https://doi.org/10.1109/84.982863.

(46) Rao, C. N. R.; Müller, A.; Cheetham, A. K. *The Chemistry of Nanomaterials: Synthesis, Properties and Applications*; John Wiley & Sons, 2006.

(47) Tomar, R.; Abdala, A. A.; Chaudhary, R. G.; Singh, N. B. Photocatalytic Degradation of Dyes by Nanomaterials. *Mater. Today Proc.* **2020**, *29*, 967–973. https://doi.org/10.1016/j.matpr.2020.04.144.

(48) *Low-Energy Electron Diffraction: Experiment, Theory and Surface Structure ... - Michel A. VanHove, William Henry Weinberg, Chi-Ming Chan - Google Libri*. https://books.google.it/books?hl=it&lr=&id=bWLyCAAAQBAJ&oi=fnd&pg=PA1&dq=%5BVanHove,+M.A.,Weinberg,W.H.,+Chan,+C.M.:+Low-Energy+Electron+Diffraction:+Experiment,+Theory+and+Surface+Structure+Determination,+vol.+6.+Springer+Science+%26+Business+Media,+Berlin+(2012&ots=NsjrSb-ZmM&sig=aogPiZPGYdrUhlgmeqxeshRxuQE&redir_esc=y#v=onepage&q&f=false (accessed 2023-03-09).

(49) Alivisatos, A. P. Perspectives on the Physical Chemistry of Semiconductor Nanocrystals. *J. Phys. Chem.* **1996**, *100* (31), 13226–13239. https://doi.org/10.1021/jp9535506.

(50) Somorjai, G. A.; Li, Y. *Introduction to Surface Chemistry and Catalysis*; John Wiley & Sons, 2010.

(51) Nanda, K. K. Size-Dependent Density of Nanoparticles and Nanostructured Materials. *Phys. Lett. A* **2012**, *376* (45), 3301–3302. https://doi.org/10.1016/j.physleta.2012.10.001.

(52) Xu, L.; Liang, H.-W.; Yang, Y.; Yu, S.-H. Stability and Reactivity: Positive and Negative Aspects for Nanoparticle Processing. *Chem. Rev.* **2018**, *118* (7), 3209–3250. https://doi.org/10.1021/acs.chemrev.7b00208.

(53) Tomar, R. S.; Jyoti, A.; Kaushik, S. *Nanobiotechnology: Concepts and Applications in Health, Agriculture, and Environment*; CRC Press, 2020.

(54) Wu, Q.; Miao, W.; Zhang, Y.; Gao, H.; Hui, D. Mechanical Properties of Nanomaterials: A Review. *Nanotechnol. Rev.* **2020**, *9* (1), 259–273. https://doi.org/10.1515/ntrev-2020-0021.

(55) Roduner, E. Size Matters: Why Nanomaterials Are Different. *Chem. Soc. Rev.* **2006**, *35* (7), 583. https://doi.org/10.1039/b502142c.

(56) Makvandi, P.; Wang, C.; Zare, E. N.; Borzacchiello, A.; Niu, L.; Tay, F. R. Metal-Based Nanomaterials in Biomedical Applications: Antimicrobial Activity and Cytotoxicity Aspects. *Adv. Funct. Mater.* **2020**, *30* (22), 1910021. https://doi.org/10.1002/adfm.201910021.

(57) Rossetti, R.; Nakahara, S.; Brus, L. E. Quantum Size Effects in the Redox Potentials, Resonance Raman Spectra, and Electronic Spectra of CdS Crystallites in Aqueous Solution. *J. Chem. Phys.* **1983**, *79* (2), 1086–1088. https://doi.org/10.1063/1.445834.

(58) Jose Varghese, R.; Oluwafemi, O. S. The Photoluminescence and Biocompatibility of CuInS2-Based Ternary Quantum Dots and Their Biological Applications. *Chemosensors* **2020**, *8* (4), 101. https://doi.org/10.3390/chemosensors8040101.

(59) Roco, D. M. C. National Nanotechnology Initiative - Past, Present, Future.

(60) Sudha, P. N.; Sangeetha, K.; Vijayalakshmi, K.; Barhoum, A. Chapter 12 - Nanomaterials History, Classification, Unique Properties, Production and Market. In *Emerging Applications of Nanoparticles and Architecture Nanostructures*; Barhoum, A., Makhlouf, A. S. H., Eds.; Micro and Nano Technologies; Elsevier, 2018; pp 341–384. https://doi.org/10.1016/B978-0-323-51254-1.00012-9.

(61) Heiligtag, F. J.; Niederberger, M. The Fascinating World of Nanoparticle Research. *Mater. Today* **2013**, *16* (7–8), 262–271. https://doi.org/10.1016/j.mattod.2013.07.004.

(62) Walter, P.; Welcomme, E.; Hallégot, P.; Zaluzec, N. J.; Deeb, C.; Castaing, J.; Veyssière, P.; Bréniaux, R.; Lévêque, J.-L.; Tsoucaris, G. Early Use of PbS Nanotechnology for an Ancient Hair Dyeing Formula. *Nano Lett.* **2006**, *6* (10), 2215–2219. https://doi.org/10.1021/nl061493u.

(63) Sharifi, S.; Behzadi, S.; Laurent, S.; Laird Forrest, M.; Stroeve, P.; Mahmoudi, M. Toxicity of Nanomaterials. *Chem Soc Rev* **2012**, *41* (6), 2323–2343. https://doi.org/10.1039/C1CS15188F.

(64) Thomas, A. Much Ado about Nothing – a Decade of Porous Materials Research. *Nat. Commun.* **2020**, *11* (1), 4985. https://doi.org/10.1038/s41467-020-18746-5.

(65) Polarz, S.; Smarsly, B. Nanoporous Materials. *J. Nanosci. Nanotechnol.* **2002**, *2* (6), 581–612. https://doi.org/10.1166/jnn.2002.151.

(66) *Nanotechnology in Textiles*; Elsevier, 2019. https://doi.org/10.1016/C2017-0-02936-1.

(67) Chen, Z.; Koel, B. E.; Sundaresan, S. Plasma-Assisted Catalysis for Ammonia Synthesis in a Dielectric Barrier Discharge Reactor: Key Surface Reaction Steps and Potential Causes of Low Energy Yield. *J. Phys. Appl. Phys.* **2022**, *55* (5), 055202. https://doi.org/10.1088/1361-6463/ac2f12.

(68) Li, Y.; Cao, H.; Yu, J. Toward a New Era of Designed Synthesis of Nanoporous Zeolitic Materials. *ACS Nano* **2018**, *12* (5), 4096–4104. https://doi.org/10.1021/acsnano.8b02625.

(69) ALOthman, Z. A Review: Fundamental Aspects of Silicate Mesoporous Materials. *Materials* **2012**, *5* (12), 2874–2902. https://doi.org/10.3390/ma5122874.

(70) Yang, Z.; Xie, Z.; Liu, H.; Yan, F.; Ju, H. Streptavidin-Functionalized Three-Dimensional Ordered Nanoporous Silica Film for Highly Efficient Chemiluminescent Immunosensing. *Adv. Funct. Mater.* **2008**, *18* (24), 3991–3998. https://doi.org/10.1002/adfm.200801022.

(71) Corma, A.; Kan, Q.; Navarro, M. T.; Pérez-Pariente, J.; Rey, F. Synthesis of MCM-41 with Different Pore Diameters without Addition of Auxiliary Organics. *Chem. Mater.* **1997**, *9* (10), 2123–2126. https://doi.org/10.1021/cm970203v.

(72) Zeleňák, V.; Halamová, D.; Almáši, M.; Žid, L.; Zeleňáková, A.; Kapusta, O. Ordered Cubic Nanoporous Silica Support MCM-48 for Delivery of Poorly Soluble Drug Indomethacin. *Appl. Surf. Sci.* **2018**, *443*, 525–534. https://doi.org/10.1016/j.apsusc.2018.02.260.

(73) Giraldo, L. F.; López, B. L.; Pérez, L.; Urrego, S.; Sierra, L.; Mesa, M. Mesoporous Silica Applications. *Macromol. Symp.* **2007**, *258* (1), 129–141. https://doi.org/10.1002/masy.200751215.

(74) Cai, Q.; Luo, Z.-S.; Pang, W.-Q.; Fan, Y.-W.; Chen, X.-H.; Cui, F.-Z. Dilute Solution Routes to Various Controllable Morphologies of MCM-41 Silica with a Basic Medium. *Chem. Mater.* **2001**, *13* (2), 258–263. https://doi.org/10.1021/cm990661z.

(75) Kruk, M.; Jaroniec, M.; Antochshuk, V.; Sayari, A. Mesoporous Silicate−Surfactant Composites with Hydrophobic Surfaces and Tailored Pore Sizes. *J. Phys. Chem. B* **2002**, *106* (39), 10096–10101. https://doi.org/10.1021/jp026252z.

(76) Hattori, H. Heterogeneous Basic Catalysis. *Chem. Rev.* **1995**, *95* (3), 537–558. https://doi.org/10.1021/cr00035a005.

(77) Huang, L.; Wind, S. J.; O'Brien, S. P. Controlled Growth of Single-Walled Carbon Nanotubes from an Ordered Mesoporous Silica Template. *Nano Lett.* **2003**, *3* (3), 299–303. https://doi.org/10.1021/nl025880p.

(78) Chen, Y.; Ciuparu, D.; Lim, S.; Haller, G. L.; Pfefferle, L. D. The Effect of the Cobalt Loading on the Growth of Single Wall Carbon Nanotubes by CO Disproportionation on Co-MCM-41 Catalysts. *Carbon* **2006**, *44* (1), 67–78. https://doi.org/10.1016/j.carbon.2005.07.035.

(79) Iqbal, P.; Preece, J. A.; Mendes, P. M. Nanotechnology: The "Top-Down" and "Bottom-Up" Approaches. In *Supramolecular Chemistry*; Gale, P. A., Steed, J. W., Eds.; John Wiley & Sons, Ltd: Chichester, UK, 2012; p smc195. https://doi.org/10.1002/9780470661345.smc195.

(80) Baig, N.; Kammakakam, I.; Falath, W. Nanomaterials: A Review of Synthesis Methods, Properties, Recent Progress, and Challenges. *Mater. Adv.* **2021**, *2* (6), 1821–1871. https://doi.org/10.1039/D0MA00807A.

(81) Gazs  , A. *Production of Nanoparticles and Nanomaterials (NanoTrust Dossier No. 006en - February 2011)*; 0xc1aa5576_0x002544e3; self: Vienna, 2012; p 0xc1aa5576_0x002544e3. https://doi.org/10.1553/ITA-nt-006en.

(82) Fung, S. Y.; Hong, Y.; Keyes-Baig, C.; Chen, P. Self-Assembly of Peptides and Its Potential Applications. In *Molecular Interfacial Phenomena of Polymers and Biopolymers*; Elsevier, 2005; pp 421–474. https://doi.org/10.1533/9781845690830.3.421.

(83) Majhi, K. C.; Yadav, M. Synthesis of Inorganic Nanomaterials Using Carbohydrates. In *Green Sustainable Process for Chemical and Environmental Engineering and Science*; Elsevier, 2021; pp 109–135. https://doi.org/10.1016/B978-0-12-821887-7.00003-3.

(84) Machac, P.; Cichon, S.; Lapcak, L.; Fekete, L. Graphene Prepared by Chemical Vapour Deposition Process. *Graphene Technol.* **2020**, *5* (1–2), 9–17. https://doi.org/10.1007/s41127-019-00029-6.

(85) *Chemical Vapour Deposition: Precursors, Processes and Applications*; Jones, A. C., Hitchman, M. L., Eds.; Royal Society of Chemistry: Cambridge, 2008. https://doi.org/10.1039/9781847558794.

(86) Serp, P.; Kalck, P.; Feurer, R. Chemical Vapor Deposition Methods for the Controlled Preparation of Supported Catalytic Materials. *Chem. Rev.* **2002**, *102* (9), 3085–3128. https://doi.org/10.1021/cr9903508.

(87) Dong, Y.; Du, X.; Liang, P.; Man, X. One-Pot Solvothermal Method to Fabricate 1D-VS4 Nanowires as Anode Materials for Lithium Ion Batteries. *Inorg. Chem. Commun.* **2020**, *115*, 107883. https://doi.org/10.1016/j.inoche.2020.107883.

(88) Wu, X.; Lu, G. Q. (Max); Wang, L. Shell-in-Shell TiO2 Hollow Spheres Synthesized by One-Pot Hydrothermal Method for Dye-Sensitized Solar Cell Application. *Energy Environ. Sci.* **2011**, *4* (9), 3565. https://doi.org/10.1039/c0ee00727g.

(89) Cao, S.; Zhao, C.; Han, T.; Peng, L. Hydrothermal Synthesis, Characterization and Gas Sensing Properties of the WO3 Nanofibers. *Mater. Lett.* **2016**, *169*, 17–20. https://doi.org/10.1016/j.matlet.2016.01.053.

(90) Chen, A.; Holt-Hindle, P. Platinum-Based Nanostructured Materials: Synthesis, Properties, and Applications. *Chem. Rev.* **2010**, *110* (6), 3767–3804. https://doi.org/10.1021/cr9003902.

(91) *Handbook of Nanoparticles*; Aliofkhazraei, M., Ed.; Springer International Publishing: Cham, 2016. https://doi.org/10.1007/978-3-319-15338-4.

(92) Danks, A. E.; Hall, S. R.; Schnepp, Z. The Evolution of 'Sol–Gel' Chemistry as a Technique for Materials Synthesis. *Mater. Horiz.* **2016**, *3* (2), 91–112. https://doi.org/10.1039/C5MH00260E.

(93) Tseng, T. K.; Lin, Y. S.; Chen, Y. J.; Chu, H. A Review of Photocatalysts Prepared by Sol-Gel Method for VOCs Removal. *Int. J. Mol. Sci.* **2010**, *11* (6), 2336–2361. https://doi.org/10.3390/ijms11062336.

(94) Parashar, M.; Shukla, V. K.; Singh, R. Metal Oxides Nanoparticles via Sol–Gel Method: A Review on Synthesis, Characterization and Applications. *J. Mater. Sci. Mater. Electron.* **2020**, *31* (5), 3729–3749. https://doi.org/10.1007/s10854-020-02994-8.

(95) de Coelho Escobar, C.; dos Santos, J. H. Z. Effect of the Sol–Gel Route on the Textural Characteristics of Silica Imprinted with Rhodamine B. *J. Sep. Sci.* **2014**, *37* (7), 868–875. https://doi.org/10.1002/jssc.201301143.

(96) Munnik, P.; de Jongh, P. E.; de Jong, K. P. Recent Developments in the Synthesis of Supported Catalysts. *Chem. Rev.* **2015**, *115* (14), 6687–6718. https://doi.org/10.1021/cr500486u.

(97) Abid, N.; Khan, A. M.; Shujait, S.; Chaudhary, K.; Ikram, M.; Imran, M.; Haider, J.; Khan, M.; Khan, Q.; Maqbool, M. Synthesis of Nanomaterials Using Various Top-down and Bottom-up Approaches, Influencing Factors, Advantages, and Disadvantages: A Review. *Adv. Colloid Interface Sci.* **2022**, *300*, 102597. https://doi.org/10.1016/j.cis.2021.102597.

(98) Bitter, J. H.; van der Lee, M. K.; Slotboom, A. G. T.; van Dillen, A. J.; de Jong, K. P. [No Title Found]. *Catal. Lett.* **2003**, *89* (1/2), 139–142. https://doi.org/10.1023/A:1024744131630.

(99) Bianchi, C. L.; Canton, P.; Dimitratos, N.; Porta, F.; Prati, L. Selective Oxidation of Glycerol with Oxygen Using Mono and Bimetallic Catalysts Based on Au, Pd and Pt Metals. *Catal. Today* **2005**, *102–103*, 203–212. https://doi.org/10.1016/j.cattod.2005.02.003.

(100) Prati, L.; Villa, A. The Art of Manufacturing Gold Catalysts. *Catalysts* **2011**, *2* (1), 24–37. https://doi.org/10.3390/catal2010024.

(101) Sankar, M.; He, Q.; Morad, M.; Pritchard, J.; Freakley, S. J.; Edwards, J. K.; Taylor, S. H.; Morgan, D. J.; Carley, A. F.; Knight, D. W.; Kiely, C. J.; Hutchings, G. J. Synthesis of Stable Ligand-Free Gold–Palladium

Nanoparticles Using a Simple Excess Anion Method. *ACS Nano* **2012**, *6* (8), 6600–6613. https://doi.org/10.1021/nn302299e.

(102) Zhao, P.; Li, N.; Astruc, D. State of the Art in Gold Nanoparticle Synthesis. *Coord. Chem. Rev.* **2013**, *257* (3–4), 638–665. https://doi.org/10.1016/j.ccr.2012.09.002.

(103) Villa, A.; Wang, D.; Veith, G. M.; Vindigni, F.; Prati, L. Sol Immobilization Technique: A Delicate Balance between Activity, Selectivity and Stability of Gold Catalysts. *Catal. Sci. Technol.* **2013**, *3* (11), 3036. https://doi.org/10.1039/c3cy00260h.

(104) Prati, L.; Villa, A.; Chan-Thaw, C. E.; Arrigo, R.; Wang, D.; Su, D. S. Gold Catalyzed Liquid Phase Oxidation of Alcohol: The Issue of Selectivity. *Faraday Discuss.* **2011**, *152*, 353. https://doi.org/10.1039/c1fd00016k.

(105) Villa, A.; Wang, D.; Su, D.; Veith, G. M.; Prati, L. Using Supported Au Nanoparticles as Starting Material for Preparing Uniform Au/Pd Bimetallic Catalysts. *Phys. Chem. Chem. Phys.* **2010**, *12* (9), 2183. https://doi.org/10.1039/b919322g.

(106) Porta, F.; Prati, L.; Rossi, M.; Coluccia, S.; Martra, G. Metal Sols as a Useful Tool for Heterogeneous Gold Catalyst Preparation: Reinvestigation of a Liquid Phase Oxidation. *Catal. Today* **2000**, *61* (1–4), 165–172. https://doi.org/10.1016/S0920-5861(00)00370-9.

(107) Lopez-Sanchez, J. A.; Dimitratos, N.; Hammond, C.; Brett, G. L.; Kesavan, L.; White, S.; Miedziak, P.; Tiruvalam, R.; Jenkins, R. L.; Carley, A. F.; Knight, D.; Kiely, C. J.; Hutchings, G. J. Facile Removal of Stabilizer-Ligands from Supported Gold Nanoparticles. *Nat. Chem.* **2011**, *3* (7), 551–556. https://doi.org/10.1038/nchem.1066.

(108) Rogers, S. M.; Catlow, C. R. A.; Gianolio, D.; Wells, P. P.; Dimitratos, N. Supported Metal Nanoparticles with Tailored Catalytic Properties through Sol-Immobilisation: Applications for the Hydrogenation of Nitrophenols. *Faraday Discuss.* **2018**, *208*, 443–454. https://doi.org/10.1039/C7FD00216E.

(109) Sun, J.; Fu, Y.; He, G.; Sun, X.; Wang, X. Catalytic Hydrogenation of Nitrophenols and Nitrotoluenes over a Palladium/Graphene Nanocomposite. *Catal Sci Technol* **2014**, *4* (6), 1742–1748. https://doi.org/10.1039/C4CY00048J.

(110) Bp-Energy-Outlook-2020.Pdf.

(111) *World Energy Outlook 2020 – Analysis*. IEA. https://www.iea.org/reports/world-energy-outlook-2020 (accessed 2023-03-09).

(112) Chehrazi, M.; Moghadas, B. K. A Review on CO2 Capture with Chilled Ammonia and CO2 Utilization in Urea Plant. *J. CO2 Util.* **2022**, *61*, 102030. https://doi.org/10.1016/j.jcou.2022.102030.

(113) Etheridge, D. M.; Steele, L. P.; Langenfelds, R. L.; Francey, R. J.; Barnola, J.-M.; Morgan, V. I. Natural and Anthropogenic Changes in Atmospheric CO_2 over the Last 1000 Years from Air in Antarctic Ice and Firn. *J. Geophys. Res. Atmospheres* **1996**, *101* (D2), 4115–4128. https://doi.org/10.1029/95JD03410.

(114) Lal, R. Soil Carbon Sequestration to Mitigate Climate Change. *Geoderma* **2004**, *123* (1–2), 1–22. https://doi.org/10.1016/j.geoderma.2004.01.032.

(115) Haigh, J. D. The Sun and the Earth's Climate. *Living Rev. Sol. Phys.* **2007**, *4*. https://doi.org/10.12942/lrsp-2007-2.

(116) Fred Singer, S. Benefits of Global Warming. *Society* **1992**, *29* (3), 33–40. https://doi.org/10.1007/BF02695295.

(117) US Department of Commerce, N. *Global Monitoring Laboratory - Carbon Cycle Greenhouse Gases*. https://gml.noaa.gov/ccgg/trends/global.html (accessed 2023-03-09).

(118) Raghuvanshi, S. P.; Chandra, A.; Raghav, A. K. Carbon Dioxide Emissions from Coal Based Power Generation in India. *Energy Convers. Manag.* **2006**, *47* (4), 427–441. https://doi.org/10.1016/j.enconman.2005.05.007.

(119) IPCC_WGI-AR6-Press-Release_en.Pdf.

(120) Blasing, T. Recent Greenhouse Gas Concentrations, 2016. https://doi.org/10.3334/CDIAC/ATG.032.

(121) *Climate Change: Atmospheric Carbon Dioxide | NOAA Climate.gov*. https://www.climate.gov/news-features/understanding-climate/climate-change-atmospheric-carbon-dioxide (accessed 2023-03-09).

(122) Alexander, L. V.; Allen, S. K.; Bindoff, N. L.; Bréon, F.-M.; Church, J. A.; Cubasch, U.; Emori, S.; Forster, P.; Friedlingstein, P.; Gillett, N.; Gregory, J. M.; Hartmann, D. L.; Jansen, E.; Kirtman, B.; Knutti, R.; Kanikicharla, K. K.; Lemke, P.; Marotzke, J.; Masson-Delmotte, V.; Meehl, G. A.; Mokhov, I. I.; Piao, S.; Plattner, G.-K.; Dahe, Q.; Ramaswamy, V.; Randall, D.; Rhein, M.; Rojas, M.; Sabine, C.; Shindell, D.; Stocker, T. F.; Talley, L. D.; Vaughan, D. G.; Xie, S.-P.; Allen, M. R.; Boucher, O.; Chambers, D.; Christensen, J. H.; Ciais, P.; Clark, P. U.; Collins, M.; Comiso, J. C.; de Menezes, V. V.; Feely, R. A.; Fichefet, T.; Fiore, A. M.; Flato, G.; Fuglestvedt, J.; Hegerl, G.; Hezel, P. J.; Johnson, G. C.; Kaser, G.; Kattsov, V.; Kennedy, J. IPCC vijfde assessment cyclus, Werkgroep I.

(123) Wei, T.; Yang, S.; Moore, J. C.; Shi, P.; Cui, X.; Duan, Q.; Xu, B.; Dai, Y.; Yuan, W.; Wei, X.; Yang, Z.; Wen, T.; Teng, F.; Gao, Y.; Chou, J.; Yan, X.; Wei, Z.; Guo, Y.; Jiang, Y.; Gao, X.; Wang, K.; Zheng, X.; Ren, F.; Lv, S.; Yu, Y.; Liu, B.; Luo, Y.; Li, W.; Ji, D.; Feng, J.; Wu, Q.; Cheng, H.; He, J.; Fu, C.; Ye, D.; Xu, G.; Dong, W. Developed and Developing World Responsibilities for Historical Climate Change and CO_2 Mitigation. *Proc. Natl. Acad. Sci.* **2012**, *109* (32), 12911–12915. https://doi.org/10.1073/pnas.1203282109.

(124) Koelbl, B. S.; van den Broek, M. A.; Faaij, A. P. C.; van Vuuren, D. P. Uncertainty in Carbon Capture and Storage (CCS) Deployment Projections: A Cross-Model Comparison Exercise. *Clim. Change* **2014**, *123* (3–4), 461–476. https://doi.org/10.1007/s10584-013-1050-7.

(125) Paris Agreement.Pdf.

(126) Daggash, H. A.; Mac Dowell, N. The Implications of Delivering the UK's Paris Agreement Commitments on the Power Sector. *Int. J. Greenh. Gas Control* **2019**, *85*, 174–181. https://doi.org/10.1016/j.ijggc.2019.04.007.

(127) Lomax, G.; Workman, M.; Lenton, T.; Shah, N. Reframing the Policy Approach to Greenhouse Gas Removal Technologies. *Energy Policy* **2015**, *78*, 125–136. https://doi.org/10.1016/j.enpol.2014.10.002.

(128) McGlashan, N.; Shah, N.; Caldecott, B.; Workman, M. High-Level Techno-Economic Assessment of Negative Emissions Technologies. *Process Saf. Environ. Prot.* **2012**, *90* (6), 501–510. https://doi.org/10.1016/j.psep.2012.10.004.

(129) Jiao, N.; Wang, H.; Xu, G.; Aricò, S. Blue Carbon on the Rise: Challenges and Opportunities. *Natl. Sci. Rev.* **2018**, *5* (4), 464–468. https://doi.org/10.1093/nsr/nwy030.

(130) Renforth, P.; Kruger, T. Coupling Mineral Carbonation and Ocean Liming. *Energy Fuels* **2013**, *27* (8), 4199–4207. https://doi.org/10.1021/ef302030w.

(131) 2018-SOPHE-Program-282018.Pdf.

(132) Zhu, X.; Li, S.; Shi, Y.; Cai, N. Recent Advances in Elevated-Temperature Pressure Swing Adsorption for Carbon Capture and Hydrogen Production. *Prog. Energy Combust. Sci.* **2019**, *75*, 100784. https://doi.org/10.1016/j.pecs.2019.100784.

(133) NCASI22_Forest_Carbon_YoungVsOld_print.Pdf. https://www.ncasi.org/wp-content/uploads/2021/01/NCASI22_Forest_Carbon_YoungVsOld_print.pdf (accessed 2023-03-09).

(134) Afforestation and Reforestation under the Clean Development Mechanism - United Nations.Pdf.

(135) Zomer, R. J.; Trabucco, A.; Bossio, D. A.; Verchot, L. V. Climate Change Mitigation: A Spatial Analysis of Global Land Suitability for Clean Development Mechanism Afforestation and Reforestation. *Agric. Ecosyst. Environ.* **2008**, *126* (1–2), 67–80. https://doi.org/10.1016/j.agee.2008.01.014.

(136) Cerasoli, S.; Yin, J.; Porporato, A. Cloud Cooling Effects of Afforestation and Reforestation at Midlatitudes. *Proc. Natl. Acad. Sci.* **2021**, *118* (33), e2026241118. https://doi.org/10.1073/pnas.2026241118.

(137) Locatelli, B.; Catterall, C. P.; Imbach, P.; Kumar, C.; Lasco, R.; Marín-Spiotta, E.; Mercer, B.; Powers, J. S.; Schwartz, N.; Uriarte, M. Tropical Reforestation and Climate Change: Beyond Carbon. *Restor. Ecol.* **2015**, *23* (4), 337–343. https://doi.org/10.1111/rec.12209.

(138) McKinley, D. C.; Ryan, M. G.; Birdsey, R. A.; Giardina, C. P.; Harmon, M. E.; Heath, L. S.; Houghton, R. A.; Jackson, R. B.; Morrison, J. F.; Murray, B. C.; Pataki, D. E.; Skog, K. E. A Synthesis of Current Knowledge on Forests and Carbon Storage in the United States. *Ecol. Appl.* **2011**, *21* (6), 1902–1924. https://doi.org/10.1890/10-0697.1.

(139) Erans, M.; Sanz-Pérez, E. S.; Hanak, D. P.; Clulow, Z.; Reiner, D. M.; Mutch, G. A. Direct Air Capture: Process Technology, Techno-Economic and Socio-Political Challenges. *Energy Environ. Sci.* **2022**, *15* (4), 1360–1405. https://doi.org/10.1039/D1EE03523A.

(140) Pan, G.; Smith, P.; Pan, W. The Role of Soil Organic Matter in Maintaining the Productivity and Yield Stability of Cereals in China. *Agric. Ecosyst. Environ.* **2009**, *129* (1–3), 344–348. https://doi.org/10.1016/j.agee.2008.10.008.

(141) Stanley, P. L.; Rowntree, J. E.; Beede, D. K.; DeLonge, M. S.; Hamm, M. W. Impacts of Soil Carbon Sequestration on Life Cycle Greenhouse Gas Emissions in Midwestern USA Beef Finishing Systems. *Agric. Syst.* **2018**, *162*, 249–258. https://doi.org/10.1016/j.agsy.2018.02.003.

(142) *Coastal Blue Carbon*. https://oceanservice.noaa.gov/ecosystems/coastal-blue-carbon/ (accessed 2023-03-09).

(143) Mutch, G. A.; Morandi, S.; Walker, R.; Anderson, J. A.; Vega-Maza, D.; Operti, L.; Cerrato, G. Cation Dependent Carbonate Speciation and the Effect of Water. *J. Phys. Chem. C* **2016**, *120* (31), 17570–17578. https://doi.org/10.1021/acs.jpcc.6b05475.

(144) Renforth, P. The Negative Emission Potential of Alkaline Materials. *Nat. Commun.* **2019**, *10* (1), 1401. https://doi.org/10.1038/s41467-019-09475-5.

(145) Jamaludin, N.; Rashid, S. A.; Tan, T. Natural Biomass as Carbon Sources for the Synthesis of Photoluminescent Carbon Dots. In *Synthesis, Technology and Applications of Carbon Nanomaterials*; Elsevier, 2019; pp 109–134. https://doi.org/10.1016/B978-0-12-815757-2.00005-X.

(146) Kammann, C.; Ippolito, J.; Hagemann, N.; Borchard, N.; Cayuela, M. L.; Estavillo, J. M.; Fuertes-Mendizabal, T.; Jeffery, S.; Kern, J.; Novak, J.; Rasse, D.; Saarnio, S.; Schmidt, H.-P.; Spokas, K.; Wrage-Mönnig, N. BIOCHAR AS A TOOL TO REDUCE THE AGRICULTURAL GREENHOUSE-GAS BURDEN – KNOWNS, UNKNOWNS AND FUTURE RESEARCH NEEDS. *J. Environ. Eng. Landsc. Manag.* **2017**, *25* (2), 114–139. https://doi.org/10.3846/16486897.2017.1319375.

(147) Wang, L.; Gao, C.; Yang, K.; Sheng, Y.; Xu, J.; Zhao, Y.; Lou, J.; Sun, R.; Zhu, L. Effects of Biochar Aging in the Soil on Its Mechanical Property and Performance for Soil CO2 and N2O Emissions. *Sci. Total Environ.* **2021**, *782*, 146824. https://doi.org/10.1016/j.scitotenv.2021.146824.

(148) Obersteiner, M.; Azar, Ch.; Kauppi, P.; Möllersten, K.; Moreira, J.; Nilsson, S.; Read, P.; Riahi, K.; Schlamadinger, B.; Yamagata, Y.; Yan, J.; van Ypersele, J.-P. Managing Climate Risk. *Science* **2001**, *294* (5543), 786–787. https://doi.org/10.1126/science.294.5543.786b.

(149) Keith, D. W. [No Title Found]. *Clim. Change* **2001**, *49* (1/2), 1–10. https://doi.org/10.1023/A:1010617015484.

(150) Committee on Developing a Research Agenda for Carbon Dioxide Removal and Reliable Sequestration; Board on Atmospheric Sciences and Climate; Board on Energy and Environmental Systems; Board on Agriculture and Natural Resources; Board on Earth Sciences and Resources; Board on Chemical Sciences and Technology; Ocean Studies Board; Division on Earth and Life Studies; National Academies of Sciences, Engineering, and Medicine. *Negative Emissions Technologies and Reliable Sequestration: A Research Agenda*; National Academies Press: Washington, D.C., 2019; p 25259. https://doi.org/10.17226/25259.

(151) *Combining Bioenergy with CCS – Analysis*. IEA. https://www.iea.org/reports/combining-bioenergy-with-ccs (accessed 2023-03-09).

(152) Boot-Handford, M. E.; Abanades, J. C.; Anthony, E. J.; Blunt, M. J.; Brandani, S.; Mac Dowell, N.; Fernández, J. R.; Ferrari, M.-C.; Gross, R.; Hallett, J. P.; Haszeldine, R. S.; Heptonstall, P.; Lyngfelt, A.; Makuch, Z.; Mangano, E.; Porter, R. T. J.; Pourkashanian, M.; Rochelle, G. T.; Shah, N.; Yao, J. G.; Fennell, P. S. Carbon Capture and Storage Update. *Energy Env. Sci* **2014**, *7* (1), 130–189. https://doi.org/10.1039/C3EE42350F.

(153) Grimes, P.; Associates, G. Author(s): Klaus Lackner, ALDSSR Hans-Joachim Ziock, P-25.

(154) Azarabadi, H.; Lackner, K. S. A Sorbent-Focused Techno-Economic Analysis of Direct Air Capture. *Appl. Energy* **2019**, *250*, 959–975. https://doi.org/10.1016/j.apenergy.2019.04.012.

(155) Fu, D.; Park, Y.; Davis, M. E. Confinement Effects Facilitate Low-Concentration Carbon Dioxide Capture with Zeolites. *Proc. Natl. Acad. Sci.* **2022**, *119* (39), e2211544119. https://doi.org/10.1073/pnas.2211544119.

(156) Jiang, N.; Shen, Y.; Liu, B.; Zhang, D.; Tang, Z.; Li, G.; Fu, B. CO2 Capture from Dry Flue Gas by Means of VPSA, TSA and TVSA. *J. CO2 Util.* **2020**, *35*, 153–168. https://doi.org/10.1016/j.jcou.2019.09.012.

(157) Roh, K.; Frauzem, R.; Gani, R.; Lee, J. H. Process Systems Engineering Issues and Applications towards Reducing Carbon Dioxide Emissions through Conversion Technologies. *Chem. Eng. Res. Des.* **2016**, *116*, 27–47. https://doi.org/10.1016/j.cherd.2016.10.007.

(158) Saeidi, S.; Najari, S.; Fazlollahi, F.; Nikoo, M. K.; Sefidkon, F.; Klemeš, J. J.; Baxter, L. L. Mechanisms and Kinetics of CO 2 Hydrogenation to Value-Added Products: A Detailed Review on Current Status and Future Trends. *Renew. Sustain. Energy Rev.* **2017**, *80*, 1292–1311. https://doi.org/10.1016/j.rser.2017.05.204.

(159) Centi, G.; Perathoner, S. Opportunities and Prospects in the Chemical Recycling of Carbon Dioxide to Fuels. *Catal. Today* **2009**, *148* (3–4), 191–205. https://doi.org/10.1016/j.cattod.2009.07.075.

(160) Curtiss, L. A.; Raghavachari, K.; Redfern, P. C.; Pople, J. A. Assessment of Gaussian-2 and Density Functional Theories for the Computation of Enthalpies of Formation. *J. Chem. Phys.* **1997**, *106* (3), 1063–1079. https://doi.org/10.1063/1.473182.

(161) Jiang, Z.; Xiao, T.; Kuznetsov, V. L.; Edwards, P. P. Turning Carbon Dioxide into Fuel. *Philos. Trans. R. Soc. Math. Phys. Eng. Sci.* **2010**, *368* (1923), 3343–3364. https://doi.org/10.1098/rsta.2010.0119.

(162) Aresta, M.; Dibenedetto, A. Carbon Recycling Through CO2-Conversion for Stepping Toward a Cyclic-C Economy. A Perspective. *Front. Energy Res.* **2020**, *8*, 159. https://doi.org/10.3389/fenrg.2020.00159.

(163) Xiaoding, X.; Moulijn, J. A. Mitigation of CO 2 by Chemical Conversion: Plausible Chemical Reactions and Promising Products. *Energy Fuels* **1996**, *10* (2), 305–325. https://doi.org/10.1021/ef9501511.

(164) Ganesh, I. Conversion of Carbon Dioxide into Methanol – a Potential Liquid Fuel: Fundamental Challenges and Opportunities (a Review). *Renew. Sustain. Energy Rev.* **2014**, *31*, 221–257. https://doi.org/10.1016/j.rser.2013.11.045.

(165) Bozzano, G.; Manenti, F. Efficient Methanol Synthesis: Perspectives, Technologies and Optimization Strategies. *Prog. Energy Combust. Sci.* **2016**, *56*, 71–105. https://doi.org/10.1016/j.pecs.2016.06.001.

(166) Dalena, F.; Senatore, A.; Marino, A.; Gordano, A.; Basile, M.; Basile, A. Methanol Production and Applications: An Overview. In *Methanol*; Elsevier, 2018; pp 3–28. https://doi.org/10.1016/B978-0-444-63903-5.00001-7.

(167) Wang, M.; Luo, L.; Wang, C.; Du, J.; Li, H.; Zeng, J. Heterogeneous Catalysts toward CO 2 Hydrogenation for Sustainable Carbon Cycle. *Acc. Mater. Res.* **2022**, *3* (6), 565–571. https://doi.org/10.1021/accountsmr.2c00006.

(168) Álvarez, A.; Bansode, A.; Urakawa, A.; Bavykina, A. V.; Wezendonk, T. A.; Makkee, M.; Gascon, J.; Kapteijn, F. Challenges in the Greener Production of Formates/Formic Acid, Methanol, and DME by Heterogeneously Catalyzed CO 2 Hydrogenation Processes. *Chem. Rev.* **2017**, *117* (14), 9804–9838. https://doi.org/10.1021/acs.chemrev.6b00816.

(169) Atsonios, K.; Panopoulos, K. D.; Kakaras, E. Investigation of Technical and Economic Aspects for Methanol Production through CO 2 Hydrogenation. *Int. J. Hydrog. Energy* **2016**, *41* (4), 2202–2214. https://doi.org/10.1016/j.ijhydene.2015.12.074.

(170) Goeppert, A.; Czaun, M.; Jones, J.-P.; Surya Prakash, G. K.; Olah, G. A. Recycling of Carbon Dioxide to Methanol and Derived Products – Closing the Loop. *Chem Soc Rev* **2014**, *43* (23), 7995–8048. https://doi.org/10.1039/C4CS00122B.

(171) Onishi, N.; Laurenczy, G.; Beller, M.; Himeda, Y. Recent Progress for Reversible Homogeneous Catalytic Hydrogen Storage in Formic Acid and in Methanol. *Coord. Chem. Rev.* **2018**, *373*, 317–332. https://doi.org/10.1016/j.ccr.2017.11.021.

(172) Methanol.Pdf.

(173) Plessow, P. N.; Studt, F. Unraveling the Mechanism of the Initiation Reaction of the Methanol to Olefins Process Using Ab Initio and DFT Calculations. *ACS Catal.* **2017**, *7* (11), 7987–7994. https://doi.org/10.1021/acscatal.7b03114.

(174) Zhong, J.; Yang, X.; Wu, Z.; Liang, B.; Huang, Y.; Zhang, T. State of the Art and Perspectives in Heterogeneous Catalysis of CO 2 Hydrogenation to Methanol. *Chem. Soc. Rev.* **2020**, *49* (5), 1385–1413. https://doi.org/10.1039/C9CS00614A.

(175) Ghasemzadeh, K.; Sadati Tilebon, S. M.; Nasirinezhad, M.; Basile, A. Cost Estimation of an Integrated System for Co-Production of Electricity and Methanol. In *Methanol*; Elsevier, 2018; pp 633–659. https://doi.org/10.1016/B978-0-444-63903-5.00024-8.

(176) Saito, M.; Fujitani, T.; Takeuchi, M.; Watanabe, T. Development of Copper/Zinc Oxide-Based Multicomponent Catalysts for Methanol Synthesis from Carbon Dioxide and Hydrogen. *Appl. Catal. Gen.* **1996**, *138* (2), 311–318. https://doi.org/10.1016/0926-860X(95)00305-3.

(177) González-Castaño, M.; Dorneanu, B.; Arellano-García, H. The Reverse Water Gas Shift Reaction: A Process Systems Engineering Perspective. *React. Chem. Eng.* **2021**, *6* (6), 954–976. https://doi.org/10.1039/D0RE00478B.

(178) Dieterich, V.; Buttler, A.; Hanel, A.; Spliethoff, H.; Fendt, S. Power-to-Liquid *via* Synthesis of Methanol, DME or Fischer–Tropsch-Fuels: A Review. *Energy Environ. Sci.* **2020**, *13* (10), 3207–3252. https://doi.org/10.1039/D0EE01187H.

(179) Nguyen Hoang, T. T.; Tsai, D.-H. Low-Temperature Methanol Synthesis via (CO2 + CO) Combined Hydrogenation Using Cu-ZnO/Al2O3 Hybrid Nanoparticle Cluster. *Appl. Catal. Gen.* **2022**, *645*, 118844. https://doi.org/10.1016/j.apcata.2022.118844.

(180) Supp, E. *How to Produce Methanol from Coal*; Springer Science & Business Media, 2013.

(181) Chen, L.; Jiang, Q.; Song, Z.; Posarac, D. Optimization of Methanol Yield from a Lurgi Reactor. *Chem. Eng. Technol.* **2011**, *34* (5), 817–822. https://doi.org/10.1002/ceat.201000282.

(182) Filippi, E.; Badano, M. *Methanol Converters and Syncope Designs for Gasification Plants*; 2007.

(183) Kung, H. H. Deactivation of Methanol Synthesis Catalysts - a Review. *Catal. Today* **1992**, *11* (4), 443–453. https://doi.org/10.1016/0920-5861(92)80037-N.

(184) E.C. Heydorn; B.W. Diamond; R.D. Lilly. *COMMERCIAL-SCALE DEMONSTRATION OF THE LIQUID PHASE METHANOL (LPMEOH) PROCESS*; NONE, 823132; 2003; p NONE, 823132. https://doi.org/10.2172/823132.

(185) Twigg, M. V.; Spencer, M. S. Deactivation of Supported Copper Metal Catalysts for Hydrogenation Reactions. *Appl. Catal. Gen.* **2001**, *212* (1–2), 161–174. https://doi.org/10.1016/S0926-860X(00)00854-1.

(186) Gates, B. C.; Johanson, L. N. Langmuir-Hinshelwood Kinetics of the Dehydration of Methanol Catalyzed by Cation Exchange Resin. *AIChE J.* **1971**, *17* (4), 981–983. https://doi.org/10.1002/aic.690170435.

(187) Kiviranta-Pääkkönen, P. K.; Struckmann, L. K.; Linnekoski, J. A.; Krause, A. O. I. Dehydration of the Alcohol in the Etherification of Isoamylenes with Methanol and Ethanol. *Ind. Eng. Chem. Res.* **1998**, *37* (1), 18–24. https://doi.org/10.1021/ie970454d.

(188) Bhattacharya, S.; Kabir, K. B.; Hein, K. Dimethyl Ether Synthesis from Victorian Brown Coal through Gasification – Current Status, and Research and Development Needs. *Prog. Energy Combust. Sci.* **2013**, *39* (6), 577–605. https://doi.org/10.1016/j.pecs.2013.06.003.

(189) Rownaghi, A. A.; Rezaei, F.; Stante, M.; Hedlund, J. Selective Dehydration of Methanol to Dimethyl Ether on ZSM-5 Nanocrystals. *Appl. Catal. B Environ.* **2012**, *119–120*, 56–61. https://doi.org/10.1016/j.apcatb.2012.02.017.

(190) Farlow, M. W.; Adkins, H. The Hydrogenation of Carbon Dioxide and a Correction of the Reported Synthesis of Urethans. *J. Am. Chem. Soc.* **1935**, *57* (11), 2222–2223. https://doi.org/10.1021/ja01314a054.

(191) Gao, P.; Li, S.; Bu, X.; Dang, S.; Liu, Z.; Wang, H.; Zhong, L.; Qiu, M.; Yang, C.; Cai, J.; Wei, W.; Sun, Y. Direct Conversion of CO2 into Liquid Fuels with High Selectivity over a Bifunctional Catalyst. *Nat. Chem.* **2017**, *9* (10), 1019–1024. https://doi.org/10.1038/nchem.2794.

(192) Li, Z.; Wu, W.; Wang, M.; Wang, Y.; Ma, X.; Luo, L.; Chen, Y.; Fan, K.; Pan, Y.; Li, H.; Zeng, J. Ambient-Pressure Hydrogenation of CO2 into Long-Chain Olefins. *Nat. Commun.* **2022**, *13* (1), 2396. https://doi.org/10.1038/s41467-022-29971-5.

(193) Ni, Y.; Chen, Z.; Fu, Y.; Liu, Y.; Zhu, W.; Liu, Z. Selective Conversion of CO2 and H2 into Aromatics. *Nat. Commun.* **2018**, *9* (1), 3457. https://doi.org/10.1038/s41467-018-05880-4.

(194) Ding, L.; Shi, T.; Gu, J.; Cui, Y.; Zhang, Z.; Yang, C.; Chen, T.; Lin, M.; Wang, P.; Xue, N.; Peng, L.; Guo, X.; Zhu, Y.; Chen, Z.; Ding, W. CO2 Hydrogenation to Ethanol over Cu@Na-Beta. *Chem* **2020**, *6* (10), 2673–2689. https://doi.org/10.1016/j.chempr.2020.07.001.

(195) Wang, J.; Zhang, G.; Zhu, J.; Zhang, X.; Ding, F.; Zhang, A.; Guo, X.; Song, C. CO_2 Hydrogenation to Methanol over In_2O_3 -Based Catalysts: From Mechanism to Catalyst Development. *ACS Catal.* **2021**, *11* (3), 1406–1423. https://doi.org/10.1021/acscatal.0c03665.

(196) Luk, H. T.; Mondelli, C.; Ferré, D. C.; Stewart, J. A.; Pérez-Ramírez, J. Status and Prospects in Higher Alcohols Synthesis from Syngas. *Chem. Soc. Rev.* **2017**, *46* (5), 1358–1426. https://doi.org/10.1039/C6CS00324A.

(197) Aresta, M.; Dibenedetto, A.; Angelini, A. Catalysis for the Valorization of Exhaust Carbon: From CO_2 to Chemicals, Materials, and Fuels. Technological Use of CO_2. *Chem. Rev.* **2014**, *114* (3), 1709–1742. https://doi.org/10.1021/cr4002758.

(198) Mills, G. A. Status and Future Opportunities for Conversion of Synthesis Gas to Liquid Fuels. *Fuel* **1994**, *73* (8), 1243–1279. https://doi.org/10.1016/0016-2361(94)90301-8.

(199) Gupta, M.; Smith, M. L.; Spivey, J. J. Heterogeneous Catalytic Conversion of Dry Syngas to Ethanol and Higher Alcohols on Cu-Based Catalysts. *ACS Catal.* **2011**, *1* (6), 641–656. https://doi.org/10.1021/cs2001048.

(200) *World fuel ethanol - Analysis and Outlook*. https://www.distill.com/World-Fuel-Ethanol-A%26O-2004.html (accessed 2023-03-09).

(201) Bai, F. W.; Anderson, W. A.; Moo-Young, M. Ethanol Fermentation Technologies from Sugar and Starch Feedstocks. *Biotechnol. Adv.* **2008**, *26* (1), 89–105. https://doi.org/10.1016/j.biotechadv.2007.09.002.

(202) Nakagawa, Y.; Tajima, N.; Hirao, K. A Theoretical Study of Catalytic Hydration Reactions of Ethylene. *J. Comput. Chem.* **2000**, *21* (14), 1292–1304. https://doi.org/10.1002/1096-987X(20001115)21:14<1292::AID-JCC8>3.0.CO;2-5.

(203) Xu, D.; Wang, Y.; Ding, M.; Hong, X.; Liu, G.; Tsang, S. C. E. Advances in Higher Alcohol Synthesis from CO2 Hydrogenation. *Chem* **2021**, *7* (4), 849–881. https://doi.org/10.1016/j.chempr.2020.10.019.

(204) Van Der Laan, G. P.; Beenackers, A. A. C. M. Kinetics and Selectivity of the Fischer–Tropsch Synthesis: A Literature Review. *Catal. Rev.* **1999**, *41* (3–4), 255–318. https://doi.org/10.1081/CR-100101170.

(205) Chang et al. 1978.Pdf.

(206) He, Z.; Cui, M.; Qian, Q.; Zhang, J.; Liu, H.; Han, B. Synthesis of Liquid Fuel via Direct Hydrogenation of CO_2. *Proc. Natl. Acad. Sci.* **2019**, *116* (26), 12654–12659. https://doi.org/10.1073/pnas.1821231116.

(207) *Applied Industrial Catalysis*; Elsevier, 1983. https://doi.org/10.1016/B978-0-12-440201-0.X5001-2.

(208) Jang, H.-G.; Min, H.-K.; Lee, J. K.; Hong, S. B.; Seo, G. SAPO-34 and ZSM-5 Nanocrystals' Size Effects on Their Catalysis of Methanol-to-Olefin Reactions. *Appl. Catal. Gen.* **2012**, *437–438*, 120–130. https://doi.org/10.1016/j.apcata.2012.06.023.

(209) An, B.; Li, Z.; Song, Y.; Zhang, J.; Zeng, L.; Wang, C.; Lin, W. Cooperative Copper Centres in a Metal–Organic Framework for Selective Conversion of CO2 to Ethanol. *Nat. Catal.* **2019**, *2* (8), 709–717. https://doi.org/10.1038/s41929-019-0308-5.

(210) Kusama, H.; Okabe, K.; Sayama, K.; Arakawa, H. CO2 Hydrogenation to Ethanol over Promoted Rh/SiO2 Catalysts. *Catal. Today* **1996**, *28* (3), 261–266. https://doi.org/10.1016/0920-5861(95)00246-4.

(211) Yang, C.; Liu, S.; Wang, Y.; Song, J.; Wang, G.; Wang, S.; Zhao, Z.; Mu, R.; Gong, J. The Interplay between Structure and Product Selectivity of CO_2 Hydrogenation. *Angew. Chem. Int. Ed.* **2019**, *58* (33), 11242–11247. https://doi.org/10.1002/anie.201904649.

(212) Zhang, F.; Zhou, W.; Xiong, X.; Wang, Y.; Cheng, K.; Kang, J.; Zhang, Q.; Wang, Y. Selective Hydrogenation of CO_2 to Ethanol over Sodium-Modified Rhodium Nanoparticles Embedded in Zeolite Silicalite-1. *J. Phys. Chem. C* **2021**, *125* (44), 24429–24439. https://doi.org/10.1021/acs.jpcc.1c07862.

(213) Inoue, T.; Iizuka, T.; Tanabe, K. Hydrogenation of Carbon Dioxide and Carbon Monoxide over Supported Rhodium Catalysts under 10 Bar Pressure. *Appl. Catal.* **1989**, *46* (1), 1–9. https://doi.org/10.1016/S0166-9834(00)81390-1.

(214) Gnanamani, M. K.; Hamdeh, H. H.; Jacobs, G.; Shafer, W. D.; Hopps, S. D.; Thomas, G. A.; Davis, B. H. Hydrogenation of Carbon Dioxide over K-Promoted FeCo Bimetallic Catalysts Prepared from Mixed Metal Oxalates. *ChemCatChem* **2017**, *9* (7), 1303–1312. https://doi.org/10.1002/cctc.201601337.

(215) Li, S.-G.; Guo, H.-J.; Zhang, H.-R.; Luo, J.; Xiong, L.; Luo, C.-R.; Chen, X.-D. The Reverse Water-Gas Shift Reaction and the Synthesis of Mixed Alcohols over K/Cu-Zn Catalyst from CO2 Hydrogenation. *Adv. Mater. Res.* **2013**, *772*, 275–280. https://doi.org/10.4028/www.scientific.net/AMR.772.275.

(216) Tatsumi, T.; Muramats, A.; Tominaga, H. ALCOHOL SYNTHESIS FROM CO $_2$ /H $_2$ ON SILICA-SUPPORTED MOLYBDENUM CATALYSTS. *Chem. Lett.* **1985**, *14* (5), 593–594. https://doi.org/10.1246/cl.1985.593.

(217) Wang, L.; Wang, L.; Zhang, J.; Liu, X.; Wang, H.; Zhang, W.; Yang, Q.; Ma, J.; Dong, X.; Yoo, S. J.; Kim, J.; Meng, X.; Xiao, F. Selective Hydrogenation of CO $_2$ to Ethanol over Cobalt Catalysts. *Angew. Chem. Int. Ed.* **2018**, *57* (21), 6104–6108. https://doi.org/10.1002/anie.201800729.

(218) He, Z.; Qian, Q.; Ma, J.; Meng, Q.; Zhou, H.; Song, J.; Liu, Z.; Han, B. Water-Enhanced Synthesis of Higher Alcohols from CO $_2$ Hydrogenation over a Pt/Co $_3$ O $_4$ Catalyst under Milder Conditions. *Angew. Chem. Int. Ed.* **2016**, *55* (2), 737–741. https://doi.org/10.1002/anie.201507585.

(219) Sheerin, E.; Reddy, G. K.; Smirniotis, P. Evaluation of Rh/Ce x Ti 1−x O 2 Catalysts for Synthesis of Oxygenates from Syngas Using XPS and TPR Techniques. *Catal. Today* **2016**, *263*, 75–83. https://doi.org/10.1016/j.cattod.2015.07.050.

(220) Kim, M.-J.; Chae, H.-J.; Ha, K. S.; Jeong, K.-E.; Kim, C.-U.; Jeong, S.-Y.; Kim, T.-W. Structural Influence of Ordered Mesoporous Carbon Supports for the Hydrogenation of Carbon Monoxide to Alcohols. *J. Nanosci. Nanotechnol.* **2013**, *13* (11), 7511–7518. https://doi.org/10.1166/jnn.2013.7909.

(221) Yang, C.; Mu, R.; Wang, G.; Song, J.; Tian, H.; Zhao, Z.-J.; Gong, J. Hydroxyl-Mediated Ethanol Selectivity of CO $_2$ Hydrogenation. *Chem. Sci.* **2019**, *10* (11), 3161–3167. https://doi.org/10.1039/C8SC05608K.

(222) Kusama, H.; Okabe, K.; Sayama, K.; Arakawa, H. Ethanol Synthesis by Catalytic Hydrogenation of CO2 over Rh□FeSiO2 Catalysts. *Energy* **1997**, *22* (2–3), 343–348. https://doi.org/10.1016/S0360-5442(96)00095-3.

(223) Wang, G.; Luo, R.; Yang, C.; Song, J.; Xiong, C.; Tian, H.; Zhao, Z.-J.; Mu, R.; Gong, J. Active Sites in CO2 Hydrogenation over Confined VOx-Rh Catalysts. *Sci. China Chem.* **2019**, *62* (12), 1710–1719. https://doi.org/10.1007/s11426-019-9590-6.

(224) Kitamura Bando, K.; Soga, K.; Kunimori, K.; Arakawa, H. Effect of Li Additive on CO2 Hydrogenation Reactivity of Zeolite Supported Rh Catalysts. *Appl. Catal. Gen.* **1998**, *175* (1–2), 67–81. https://doi.org/10.1016/S0926-860X(98)00202-6.

(225) Gogate, M. R.; Davis, R. J. Comparative Study of CO and CO2 Hydrogenation over Supported Rh–Fe Catalysts. *Catal. Commun.* **2010**, *11* (10), 901–906. https://doi.org/10.1016/j.catcom.2010.03.020.

(226) Wang, D.; Bi, Q.; Yin, G.; Zhao, W.; Huang, F.; Xie, X.; Jiang, M. Direct Synthesis of Ethanol via CO $_2$ Hydrogenation Using Supported Gold Catalysts. *Chem. Commun.* **2016**, *52* (99), 14226–14229. https://doi.org/10.1039/C6CC08161D.

(227) Huang, X.; Teschner, D.; Dimitrakopoulou, M.; Fedorov, A.; Frank, B.; Kraehnert, R.; Rosowski, F.; Kaiser, H.; Schunk, S.; Kuretschka, C.; Schlögl, R.; Willinger, M.; Trunschke, A. Atomic-Scale Observation of the Metal–Promoter Interaction in Rh-Based Syngas-Upgrading Catalysts. *Angew. Chem. Int. Ed.* **2019**, *58* (26), 8709–8713. https://doi.org/10.1002/anie.201902750.

(228) Pan, X.; Fan, Z.; Chen, W.; Ding, Y.; Luo, H.; Bao, X. Enhanced Ethanol Production inside Carbon-Nanotube Reactors Containing Catalytic Particles. *Nat. Mater.* **2007**, *6* (7), 507–511. https://doi.org/10.1038/nmat1916.

(229) Yu, J.; Mao, D.; Han, L.; Guo, Q.; Lu, G. Conversion of Syngas to C2+ Oxygenates over Rh-Based/SiO2 Catalyst: The Promoting Effect of Fe. *J. Ind. Eng. Chem.* **2013**, *19* (3), 806–812. https://doi.org/10.1016/j.jiec.2012.10.021.

(230) Kim, T.-W.; Kim, M.-J.; Chae, H.-J.; Ha, K.-S.; Kim, C.-U. Ordered Mesoporous Carbon Supported Uniform Rhodium Nanoparticles as Catalysts for Higher Alcohol Synthesis from Syngas. *Fuel* **2015**, *160*, 393–403. https://doi.org/10.1016/j.fuel.2015.07.062.

(231) Qiao, B.; Wang, A.; Yang, X.; Allard, L. F.; Jiang, Z.; Cui, Y.; Liu, J.; Li, J.; Zhang, T. Single-Atom Catalysis of CO Oxidation Using Pt1/FeOx. *Nat. Chem.* **2011**, *3* (8), 634–641. https://doi.org/10.1038/nchem.1095.

(232) Caparrós, F. J.; Soler, L.; Rossell, M. D.; Angurell, I.; Piccolo, L.; Rossell, O.; Llorca, J. Remarkable Carbon Dioxide Hydrogenation to Ethanol on a Palladium/Iron Oxide Single-Atom Catalyst. *ChemCatChem* **2018**, *10* (11), 2365–2369. https://doi.org/10.1002/cctc.201800362.

(233) Peng, Y.; Wang, L.; Luo, Q.; Cao, Y.; Dai, Y.; Li, Z.; Li, H.; Zheng, X.; Yan, W.; Yang, J.; Zeng, J. Molecular-Level Insight into How Hydroxyl Groups Boost Catalytic Activity in CO2 Hydrogenation into Methanol. *Chem* **2018**, *4* (3), 613–625. https://doi.org/10.1016/j.chempr.2018.01.019.

(234) Pan, Y.; Liu, C.; Ge, Q. Effect of Surface Hydroxyls on Selective CO2 Hydrogenation over Ni4/γ-Al2O3: A Density Functional Theory Study. *J. Catal.* **2010**, *272* (2), 227–234. https://doi.org/10.1016/j.jcat.2010.04.003.

(235) Zhang, R.; Wang, B.; Liu, H.; Ling, L. Effect of Surface Hydroxyls on CO $_2$ Hydrogenation Over Cu/γ-Al $_2$ O $_3$ Catalyst: A Theoretical Study. *J. Phys. Chem. C* **2011**, *115* (40), 19811–19818. https://doi.org/10.1021/jp206065y.

(236) Bai, S.; Shao, Q.; Wang, P.; Dai, Q.; Wang, X.; Huang, X. Highly Active and Selective Hydrogenation of CO $_2$ to Ethanol by Ordered Pd–Cu Nanoparticles. *J. Am. Chem. Soc.* **2017**, *139* (20), 6827–6830. https://doi.org/10.1021/jacs.7b03101.

(237) Gnanamani, M. K.; Shafer, W. D.; Sparks, D. E.; Davis, B. H. Fischer–Tropsch Synthesis: Effect of CO2 Containing Syngas over Pt Promoted Co/γ-Al2O3 and K-Promoted Fe Catalysts. *Catal. Commun.* **2011**, *12* (11), 936–939. https://doi.org/10.1016/j.catcom.2011.03.002.

(238) Li, W.; Nie, X.; Jiang, X.; Zhang, A.; Ding, F.; Liu, M.; Liu, Z.; Guo, X.; Song, C. ZrO2 Support Imparts Superior Activity and Stability of Co Catalysts for CO2 Methanation. *Appl. Catal. B Environ.* **2018**, *220*, 397–408. https://doi.org/10.1016/j.apcatb.2017.08.048.

(239) Okabe, K.; Yamada, H.; Hanaoka, T.; Matsuzaki, T.; Arakawa, H.; Abe, Y. CO $_2$ Hydrogenation to Alcohols over Highly Dispersed Co/SiO $_2$ Catalysts Derived from Acetate. *Chem. Lett.* **2001**, *30* (9), 904–905. https://doi.org/10.1246/cl.2001.904.

(240) Ouyang, B.; Xiong, S.; Zhang, Y.; Liu, B.; Li, J. The Study of Morphology Effect of Pt/Co 3 O 4 Catalysts for Higher Alcohol Synthesis from CO 2 Hydrogenation. *Appl. Catal. Gen.* **2017**, *543*, 189–195. https://doi.org/10.1016/j.apcata.2017.06.031.

(241) Liu, B.; Ouyang, B.; Zhang, Y.; Lv, K.; Li, Q.; Ding, Y.; Li, J. Effects of Mesoporous Structure and Pt Promoter on the Activity of Co-Based Catalysts in Low-Temperature CO2 Hydrogenation for Higher Alcohol Synthesis. *J. Catal.* **2018**, *366*, 91–97. https://doi.org/10.1016/j.jcat.2018.07.019.

(242) Zhang, S.; Liu, X.; Shao, Z.; Wang, H.; Sun, Y. Direct CO2 Hydrogenation to Ethanol over Supported Co2C Catalysts: Studies on Support Effects and Mechanism. *J. Catal.* **2020**, *382*, 86–96. https://doi.org/10.1016/j.jcat.2019.11.038.

(243) Gnanamani, M. K.; Jacobs, G.; Keogh, R. A.; Shafer, W. D.; Sparks, D. E.; Hopps, S. D.; Thomas, G. A.; Davis, B. H. Fischer-Tropsch Synthesis: Effect of Pretreatment Conditions of Cobalt on Activity and Selectivity for Hydrogenation of Carbon Dioxide. *Appl. Catal. Gen.* **2015**, *499*, 39–46. https://doi.org/10.1016/j.apcata.2015.03.046.

(244) Tienthao, N.; Hassanzahediniaki, M.; Alamdari, H.; Kaliaguine, S. Effect of Alkali Additives over Nanocrystalline Co–Cu-Based Perovskites as Catalysts for Higher-Alcohol Synthesis. *J. Catal.* **2007**, *245* (2), 348–357. https://doi.org/10.1016/j.jcat.2006.10.026.

(245) Kattel, S.; Ramírez, P. J.; Chen, J. G.; Rodriguez, J. A.; Liu, P. Active Sites for CO $_2$ Hydrogenation to Methanol on Cu/ZnO Catalysts. *Science* **2017**, *355* (6331), 1296–1299. https://doi.org/10.1126/science.aal3573.

(246) Sun, J.; Cai, Q.; Wan, Y.; Wan, S.; Wang, L.; Lin, J.; Mei, D.; Wang, Y. Promotional Effects of Cesium Promoter on Higher Alcohol Synthesis from Syngas over Cesium-Promoted Cu/ZnO/Al $_2$ O $_3$ Catalysts. *ACS Catal.* **2016**, *6* (9), 5771–5785. https://doi.org/10.1021/acscatal.6b00935.

(247) Prieto, G.; Beijer, S.; Smith, M. L.; He, M.; Au, Y.; Wang, Z.; Bruce, D. A.; de Jong, K. P.; Spivey, J. J.; de Jongh, P. E. Design and Synthesis of Copper–Cobalt Catalysts for the Selective Conversion of Synthesis Gas to Ethanol and Higher Alcohols. *Angew. Chem.* **2014**, *126* (25), 6515–6519. https://doi.org/10.1002/ange.201402680.

(248) Ishida, T.; Yanagihara, T.; Liu, X.; Ohashi, H.; Hamasaki, A.; Honma, T.; Oji, H.; Yokoyama, T.; Tokunaga, M. Synthesis of Higher Alcohols by Fischer–Tropsch Synthesis over Alkali Metal-Modified Cobalt Catalysts. *Appl. Catal. Gen.* **2013**, *458*, 145–154. https://doi.org/10.1016/j.apcata.2013.03.042.

(249) Amoyal, M.; Vidruk-Nehemya, R.; Landau, M. V.; Herskowitz, M. Effect of Potassium on the Active Phases of Fe Catalysts for Carbon Dioxide Conversion to Liquid Fuels through Hydrogenation. *J. Catal.* **2017**, *348*, 29–39. https://doi.org/10.1016/j.jcat.2017.01.020.

(250) Guo, H.; Li, S.; Peng, F.; Zhang, H.; Xiong, L.; Huang, C.; Wang, C.; Chen, X. Roles Investigation of Promoters in K/Cu–Zn Catalyst and Higher Alcohols Synthesis from CO2 Hydrogenation over a Novel Two-Stage Bed Catalyst Combination System. *Catal. Lett.* **2015**, *145* (2), 620–630. https://doi.org/10.1007/s10562-014-1446-7.

(251) Ding, M.; Tu, J.; Qiu, M.; Wang, T.; Ma, L.; Li, Y. Impact of Potassium Promoter on Cu–Fe Based Mixed Alcohols Synthesis Catalyst. *Appl. Energy* **2015**, *138*, 584–589. https://doi.org/10.1016/j.apenergy.2014.01.010.

(252) *Solid State Chemistry in Catalysis*; Grasselli, R. K., Brazdil, J. F., Eds.; ACS Symposium Series; American Chemical Society: Washington, D.C., 1985; Vol. 279. https://doi.org/10.1021/bk-1985-0279.

(253) Santos, V. P.; van der Linden, B.; Chojecki, A.; Budroni, G.; Corthals, S.; Shibata, H.; Meima, G. R.; Kapteijn, F.; Makkee, M.; Gascon, J. Mechanistic Insight into the Synthesis of Higher Alcohols from Syngas: The Role of K Promotion on MoS_2 Catalysts. *ACS Catal.* **2013**, *3* (7), 1634–1637. https://doi.org/10.1021/cs4003518.

(254) Luk, H. T.; Mondelli, C.; Mitchell, S.; Siol, S.; Stewart, J. A.; Curulla Ferré, D.; Pérez-Ramírez, J. Role of Carbonaceous Supports and Potassium Promoter on Higher Alcohols Synthesis over Copper–Iron Catalysts. *ACS Catal.* **2018**, *8* (10), 9604–9618. https://doi.org/10.1021/acscatal.8b02714.

(255) Lu, Y.; Zhang, R.; Cao, B.; Ge, B.; Tao, F. F.; Shan, J.; Nguyen, L.; Bao, Z.; Wu, T.; Pote, J. W.; Wang, B.; Yu, F. Elucidating the Copper–Hägg Iron Carbide Synergistic Interactions for Selective CO Hydrogenation to Higher Alcohols. *ACS Catal.* **2017**, *7* (8), 5500–5512. https://doi.org/10.1021/acscatal.7b01469.

(256) Takagawa, M.; Okamoto, A.; Fujimura, H.; Izawa, Y.; Arakawa, H. Ethanol Synthesis from Carbon Dioxide and Hydrogen. In *Studies in Surface Science and Catalysis*; Elsevier, 1998; Vol. 114, pp 525–528. https://doi.org/10.1016/S0167-2991(98)80812-4.

(257) Rungtaweevoranit, B.; Baek, J.; Araujo, J. R.; Archanjo, B. S.; Choi, K. M.; Yaghi, O. M.; Somorjai, G. A. Copper Nanocrystals Encapsulated in Zr-Based Metal–Organic Frameworks for Highly Selective CO_2 Hydrogenation to Methanol. *Nano Lett.* **2016**, *16* (12), 7645–7649. https://doi.org/10.1021/acs.nanolett.6b03637.

(258) An, B.; Zhang, J.; Cheng, K.; Ji, P.; Wang, C.; Lin, W. Confinement of Ultrasmall Cu/ZnO_x Nanoparticles in Metal–Organic Frameworks for Selective Methanol Synthesis from Catalytic Hydrogenation of CO_2. *J. Am. Chem. Soc.* **2017**, *139* (10), 3834–3840. https://doi.org/10.1021/jacs.7b00058.

(259) Wang, N.; Fang, K.; Lin, M.; Jiang, D.; Li, D.; Sun, Y. Synthesis of Higher Alcohols from Syngas over Fe/K/β-Mo2C Catalyst. *Catal. Lett.* **2010**, *136* (1–2), 9–13. https://doi.org/10.1007/s10562-010-0288-1.

(260) Yong, J.; Luan, X.; Dai, X.; Zhang, X.; Yang, Y.; Zhao, H.; Cui, M.; Ren, Z.; Nie, F.; Huang, X. Alkaline-Etched NiMgAl Trimetallic Oxide-Supported KMoS-Based Catalysts for Boosting Higher Alcohol Selectivity in CO Hydrogenation. *ACS Appl. Mater. Interfaces* **2019**, *11* (21), 19066–19076. https://doi.org/10.1021/acsami.9b01267.

(261) Calafat, A.; Vivas, F.; Brito, J. L. Effects of Phase Composition and of Potassium Promotion on Cobalt Molybdate Catalysts for the Synthesis of Alcohols from CO2 and H2. *Appl. Catal. Gen.* **1998**, *172* (2), 217–224. https://doi.org/10.1016/S0926-860X(98)00127-6.

(262) Chen, Y.; Choi, S.; Thompson, L. T. Low Temperature CO2 Hydrogenation to Alcohols and Hydrocarbons over Mo2C Supported Metal Catalysts. *J. Catal.* **2016**, *343*, 147–156. https://doi.org/10.1016/j.jcat.2016.01.016.

(263) Liu, S.; Zhou, H.; Song, Q.; Ma, Z. Synthesis of Higher Alcohols from CO 2 Hydrogenation over Mo–Co–K Sulfide-Based Catalysts. *J. Taiwan Inst. Chem. Eng.* **2017**, *76*, 18–26. https://doi.org/10.1016/j.jtice.2017.04.007.

(264) Kusama H.; Arakawa H. Hydrogenation of CO2 over SiO2 Supported Rh-Co-alkalimetal Catalysts. *NIPPON KAGAKU KAISHI* **2002**, No. 1, 107–110. https://doi.org/10.1246/nikkashi.2002.107.

(265) Monti, E.; Ventimiglia, A.; Soto, C. A. G.; Martelli, F.; Rodríguez-Aguado, E.; Cecilia, J. A.; Maireles-Torres, P.; Ospitali, F.; Tabanelli, T.; Albonetti, S.; Cavani, F.; Dimitratos, N. Oxidative Condensation/Esterification of Furfural with Ethanol Using Preformed Au Colloidal Nanoparticles. Impact of

Stabilizer and Heat Treatment Protocols on Catalytic Activity and Stability. *Mol. Catal.* **2022**, *528*, 112438. https://doi.org/10.1016/j.mcat.2022.112438.

(266) Scurti, S.; Monti, E.; Rodríguez-Aguado, E.; Caretti, D.; Cecilia, J. A.; Dimitratos, N. Effect of Polyvinyl Alcohol Ligands on Supported Gold Nano-Catalysts: Morphological and Kinetics Studies. *Nanomaterials* **2021**, *11* (4), 879. https://doi.org/10.3390/nano11040879.

(267) Scurti, S.; Allegri, A.; Liuzzi, F.; Rodríguez-Aguado, E.; Cecilia, J. A.; Albonetti, S.; Caretti, D.; Dimitratos, N. Temperature-Dependent Activity of Gold Nanocatalysts Supported on Activated Carbon in Redox Catalytic Reactions: 5-Hydroxymethylfurfural Oxidation and 4-Nitrophenol Reduction Comparison. *Catalysts* **2022**, *12* (3), 323. https://doi.org/10.3390/catal12030323.

(268) Einstein, A. Kinetische Theorie Des Wärmegleichgewichtes Und Des Zweiten Hauptsatzes Der Thermodynamik [AdP 9, 417 (1902)]. *Ann. Phys.* **2005**, *517* (S1), 117–134. https://doi.org/10.1002/andp.2005517S108.

(269) Millikan, R. A. Einstein's Photoelectric Equation and Contact Electromotive Force. *Phys. Rev.* **1916**, *7* (1), 18–32. https://doi.org/10.1103/PhysRev.7.18.

(270) Greczynski, G.; Hultman, L. A Step-by-Step Guide to Perform x-Ray Photoelectron Spectroscopy. *J. Appl. Phys.* **2022**, *132* (1), 011101. https://doi.org/10.1063/5.0086359.

(271) Koopmans, T. Über die Zuordnung von Wellenfunktionen und Eigenwerten zu den Einzelnen Elektronen Eines Atoms. *Physica* **1934**, *1* (1–6), 104–113. https://doi.org/10.1016/S0031-8914(34)90011-2.

(272) Haasch, R. T. X-Ray Photoelectron Spectroscopy (XPS) and Auger Electron Spectroscopy (AES). In *Practical Materials Characterization*; Sardela, M., Ed.; Springer New York: New York, NY, 2014; pp 93–132. https://doi.org/10.1007/978-1-4614-9281-8_3.

(273) Stevie, F. A.; Donley, C. L. Introduction to X-Ray Photoelectron Spectroscopy. *J. Vac. Sci. Technol. A* **2020**, *38* (6), 063204. https://doi.org/10.1116/6.0000412.

(274) Shirley, D. A. High-Resolution X-Ray Photoemission Spectrum of the Valence Bands of Gold. *Phys. Rev. B* **1972**, *5* (12), 4709–4714. https://doi.org/10.1103/PhysRevB.5.4709.

(275) Hanaor, D. A. H.; Sorrell, C. C. Review of the Anatase to Rutile Phase Transformation. *J. Mater. Sci.* **2011**, *46* (4), 855–874. https://doi.org/10.1007/s10853-010-5113-0.

(276) Chao, M. C.; Lin, H. P.; Sheu, H. S.; Mou, C. Y. A Study of Morphology of Mesoporous Silica SBA-15. *Stud Surf Sci Catal* **2002**, *141*, 387–394.